

# Development of an Eddy Current Inversion Algorithm for Characterization of Surface Defects

by

Ehsan MOHSENI

MANUSCRIPT-BASED THESIS PRESENTED TO ÉCOLE DE  
TECHNOLOGIE SUPÉRIEURE IN PARTIAL FULFILLMENT FOR THE  
DEGREE OF DOCTOR OF PHILOSOPHY  
Ph.D.

MONTREAL, AUGUST 20<sup>TH</sup>, 2018

ÉCOLE DE TECHNOLOGIE SUPÉRIEURE  
UNIVERSITÉ DU QUÉBEC



Ehsan Mohseni, 2018



It is forbidden to reproduce, save or share the content of this document either in whole or in parts. The reader who wishes to print or save this document on any media must first get the permission of the author.

**BOARD OF EXAMINERS**

THIS THESIS HAS BEEN EVALUATED

BY THE FOLLOWING BOARD OF EXAMINERS

Mr. Martin Viens, Thesis Supervisor  
Departement of Mechanical Engineering at École de technologie supérieure

Ms. Wen-Fang Xie, Thesis Co-supervisor  
Departement of Mechanical Engineering at Concordia university

Mr. Guy Gauthier, Chair, Board of Examiners  
Departement of Automated Manufacturing Engineering at École de technologie supérieure

Mr. Mohammad Jahazi, Member of the jury  
Departement of Mechanical Engineering at École de technologie supérieure

Mr. Catalin Mandache, External Evaluator  
Aerospace Research Center National Research Council Canada (NRC)

THIS THESIS WAS PRESENTED AND DEFENDED

IN THE PRESENCE OF A BOARD OF EXAMINERS AND THE PUBLIC

<AUGUST 8<sup>TH</sup>, 2018 >

AT ÉCOLE DE TECHNOLOGIE SUPÉRIEURE



## ACKNOWLEDGMENTS

The past years of my Ph.D. studies at École de technologie supérieure have brought me new experiences, friends and mentors. As any other life chapter, this journey also reaches its end however, taking the journey was not possible in first place without having the constant support of friends, family and university staff.

First, I owe this opportunity to my supportive and kind supervisor Professor Martin Viens who benevolently showed me the path of progression through difficult stages of my Ph.D. studies and he never stopped assisting me in fulfilling my duties as a researcher. His professional acts, manners and attitude toward others was the most precious inspiration to me and I am sincerely grateful to him for this noble lesson.

I would like to express my gratitude for the helps and supports of Professor Wen-Fang Xie who has always provided me with invaluable advises throughout my studies. Her kindness besides her mentorship has a great influence on me and I cannot thank her enough for that.

I would like to thank Dr. Demartonne Ramos França whose leadership and friendship lessons would last forever with me. He provided me with new perspectives toward my project and I deeply appreciate his devotion to being a teacher.

In addition, I am deeply grateful to the president of jury, Professor Guy Gauthier and jury members, Professor Mohammad Jahazi and Dr. Catalin Mandache for taking the time to read this dissertation despite being very occupied. I also really appreciate their comments and suggestions concerning this thesis since it would help me to make modifications towards the improvement.

I would like to extend my thanks to Natural Sciences and Engineering Research Council of Canada (NSERC), *Consortium de recherche et d'innovation en aérospatiale au Québec* (CRFAQ), *École de technologie supérieure* (ÉTS), National Research Council of Canada (CNRC-NRC), Pratt and Whitney Canada, L-3 Mas Communications, Heroux-Devtek, Bell

Helicopter, and Safran for their financial supports and making it possible to carry out these research activities. Besides, special thanks to CMC Microsystems for providing convenient access to the license of the software used in this study. Additionally, I appreciate the efforts and directions provided by all the members of the companies and other universities, who were actively involved in the projects. I am also very thankful to Professor Lionel Birglen for his devotion in direction and organisation of the project CRIAQ MANU-418 activities.

I extend my gratitude to my best friends Dr. Behzad Ghafarizadeh, Dr. Sheida Sarafan, Mr. Vahid Talei, Ms. Roja Mirheidari, Ms. Sorour Davoodi and Mr. Baoguang Xu for their sincere companionship and helps with regard to settling in Canada, starting my studies, and getting through hardships of my daily life as an international student. In addition, I am very grateful to my very special colleague Dr. Hamid Habibzadeh for helping me from the first day of my Ph.D., accompanying me during my studies, and being a kind, amazing friend.

Finally, in every moment of my life, I had the selfless support and love of my family members who are my main inspirational characters leading me in my endeavours. I feel privileged to have very compassionate, diligent and amazing parents, Houshang and Soghra, who both taught life and science lessons as teachers not only to me but also to thousands others. I appreciate the love of my siblings, Azadeh and Iman, who always backed me up in every chapter of my life.

Ehsan Mohseni

# DÉVELOPPEMENT D'UN ALGORITHME D'INVERSION DES COURANTS DE FOUCAULT POUR LA CARACTÉRISATION DES DÉFAUTS DE SURFACE

Ehsan MOHSENI

## RÉSUMÉ

L'industrie aérospatiale est de plus en plus préoccupée par l'intégrité et la performance des structures métalliques vieillissantes dans les avions qui ont été en service durant plusieurs années. Les charges cycliques appliquées à ces structures pendant la circulation au sol, la pressurisation, le décollage, la dépressurisation et l'atterrissage favorisent l'amorçage et la propagation de nombreuses fissures de fatigue dans les zones de concentration de contrainte. Ces fissures doivent être détectées et dimensionnées avec fiabilité par des méthodes de contrôle non destructif (CND) avant qu'elles n'atteignent une taille critique qui pourrait entraîner la défaillance désastreuse de la composante. Non seulement les inspections en service bénéficient d'un système de CND fiable, mais le rôle de ces systèmes devient vital lors des phases de conception. De nos jours, il est possible d'estimer la durée de vie d'une composante critique en se basant sur des modèles élaborés à partir de la mécanique de la rupture. Ces modèles permettent d'estimer, pour une durée de vie planifiée, la taille maximale d'un défaut acceptable dans une zone donnée. Par ailleurs, la taille maximale des défauts acceptables et la limite de détection fiable d'une technique de contrôle sont les intrants de modèles d'évaluation des risques utilisés pour planifier les inspections périodiques en service. En gardant cela à l'esprit, il est évident que la détection des défauts n'est plus la seule préoccupation des études sur les CND. Par conséquent, les études récentes tentent de se concentrer sur le dimensionnement des défauts et la fiabilité d'un tel dimensionnement.

Les essais par courants de Foucault (ECF) constituent une méthode électromagnétique de CND bien établie. Depuis plusieurs années, elle est utilisée pour inspecter les composants du fuselage, du moteur et des roues d'un avion à la recherche de légers défauts de surface. Dans ce contexte, les sondes de surface différentielles en réflexion (noyau en forme de D inversé) sont parmi les meilleures candidates puisqu'elles fournissent un rapport signal sur bruit élevé. La complexité de la théorie électromagnétique régissant les ECF, additionnée à la finesse des détails géométriques de ces sondes ont ralenti le développement de modèles analytiques et semi-analytiques portant sur l'interaction entre ces sondes et des défauts de surface. Par conséquent, le développement de modèles pouvant fournir des mesures quantitatives des défauts inspectés s'est accompagné de difficultés. Cependant, au cours des dernières décennies, avec le développement de l'informatique, la modélisation de ce type de problèmes est devenue plus facile grâce à des méthodes numériques telles que la modélisation par éléments finis (MEF). De plus, les techniques de calcul souple sont devenues suffisamment sophistiquées pour imiter efficacement la reconnaissance des formes et les capacités décisionnelles du cerveau humain. Ces nouvelles possibilités, issues de l'ère technologique, peuvent être intégrées afin de développer de nouvelles méthodologies d'interprétation des signaux ECF et de dimensionnement des défauts détectés.

## VIII

La présente recherche vise à développer un algorithme d'inversion des courants de Foucault pour caractériser des défauts de surface. Ce travail de recherche consiste en deux parties. La première vise à développer un outil MEF pour simuler le balayage des encoches de surface avec une sonde ECF. Dans ce contexte, la capacité de Comsol Multiphysics à modéliser l'interaction entre une sonde de surface différentielle et différentes encoches de surface a été étudiée et le modèle a été validé par des résultats expérimentaux. Par la suite, un système d'inférence adaptatif neuro-flou, conçu pour l'estimation de la longueur d'entailles, a été entraîné en utilisant les signaux de diverses encoches générées par simulation. De plus, le système de dimensionnement a été testé et sa performance a été évaluée. Concernant la deuxième partie de cette recherche, la fiabilité d'un système ECF manuel et automatisé a été étudiée en comparant les courbes de probabilité de détection obtenues en testant des composants en acier ferromagnétique comportant des fissures de fatigue. L'étude a porté sur une sonde de surface différentielle, différents inspecteurs et une variation de paramètres d'essai influents. Le concept de dimensionnement proposé dans cette recherche peut être utilisé pour tout type de sonde ECF, de matériau et de défaut.

**Mots-clés:** Contrôle non destructifs (CND), Essai par courants de Foucault (ECF), Sonde différentielle en réflexion, Évaluation non destructive quantitative (ENDQ), Dimensionnement de fissures, Étude par modélisation, Méthodes numériques, Méthode par éléments finis (MEF), Système d'inférence adaptatif neuro-flou (SIANF), Fiabilité de l'inspection, Probabilité de détection (PD), Balayage manuel par courants de Foucault, Courants de Foucault automatisés, Simulation, Fissures.

# **DEVELOPMENT OF AN EDDY CURRENT INVERSION ALGORITHM FOR CHARACTERIZATION OF SURFACE DEFECTS**

Ehsan MOHSENI

## **ABSTRACT**

There is an increasing concern in aerospace industry regarding the integrity and performance of ageing metallic structures in aircraft that have been in service for several years. Cyclic loads applied to these structures during taxiing, pressurization, taking off, depressurization, and landing promote the nucleation and growth of many fatigue cracks from the locations of stress concentration. These cracks shall be detected and sized reliably by non-destructive evaluation (NDE) methods before they reach a critical size, which may lead to disastrous failure of components. Not only the in-service inspections benefit from a reliable NDE system, but also the role of such systems is becoming vital during design stages. Nowadays, it is possible to use life estimation models developed based on fracture mechanics to estimate the maximum allowable defect size located in critical components for an anticipated life span. Moreover, risk assessment models take the estimated maximum allowable flaw size and the flaw size that can be reliably detected as inputs to plan periodical inspections. Bearing these in mind, it is evident that defect detection is not the only concern of NDE studies anymore. Hence, the recent studies try to focus on defect sizing and the reliability of the sizing as well.

Eddy current testing (ECT) is a well-established electromagnetic method of NDE. For several years, it has been employed to inspect the fuselage, wings, engine and wheel components of aircraft for tiny surface flaws. For these purposes, ECT split-D reflection differential surface probes are one of the best nominees since they provide a high signal-to-noise ratio. The complexity of electromagnetic theory governing ECT along with the very delicate geometrical details of such probes have slowed down the advances in analytical/semi-analytical modelling of the interaction between such probes and surface defects. Therefore, development of models that could provide quantitative measures of inspected defects has been accompanied with difficulties. However, with the growth of computer science and resources in recent decades, modelling of these kinds of problems using numerical methods such as finite element modelling has become faster than before. Furthermore, the soft computing techniques have become sophisticated enough to effectively imitate the pattern recognition and decision making abilities of human brain. These offerings, brought by the new technology era, can be integrated in order to develop new methodologies for interpretation of ECT signals and sizing of detected defects.

The present research aims at developing an eddy current inversion algorithm for characterization of surface defects. The research work consists of two main parts. The first part aims to develop a FEM tool to simulate scanning of surface notches with ECT probe. In this context, the capability of Comsol Multiphysics in modelling the interaction between a split-D probe and various surface notches was investigated and the model was validated by

experimental results. Subsequently, an adaptive neuro-fuzzy inference system was designed and trained, using model-generated signals of various notches, for notch length estimation. Furthermore, the sizing system was tested and its performance was assessed. As a second part to this research, reliability of the manual and automated ECT system was investigated through comparing probability of detection curves obtained by testing defective ferromagnetic steel components. The study involved a split-D surface probe, different inspectors and variation of influential test parameters. The sizing concept proposed in this research can be used for any type of ECT probe, material and defect.

**Keywords:** Non-destructive testing (NDT), Eddy current testing (ECT), Split-D reflection differential probe, Quantitative non-destructive evaluation (QNDE), Crack sizing, Model-based study, Numerical methods, Finite element method (FEM), Adaptive neuro-fuzzy inference system (ANFIS), Inspection reliability, Probability of detection (POD), Manual eddy current scan, Automated eddy current, Simulation, Cracks.

## TABLE OF CONTENTS

	Page
INTRODUCTION .....	1
CHAPTER 1 LITERATURE REVIEW .....	11
1.1 Eddy current testing .....	11
1.1.1 Electromagnetic induction .....	12
1.1.2 Eddy current testing and influential parameters .....	15
1.1.3 Modelling in eddy current testing .....	18
1.1.4 Finite element modelling of eddy current probes .....	21
1.1.5 Model-based studies of split-D differential eddy current probe .....	25
1.2 Soft computing .....	32
1.2.1 Soft computing in eddy current testing .....	35
1.3 Probability of detection .....	37
1.3.1 Probability of detection for eddy current testing .....	41
CHAPTER 2 FINITE ELEMENT BASED MODELLING OF SURFACE CRACKS SCANNING USING A REFLECTION DIFFERENTIAL SPLIT-D EDDY CURRENT PROBE .....	47
2.1 Introduction .....	48
2.2 Impedance measurement of a commercial split-D coil .....	52
2.3 Refinement of finite element modelling parameters using an absolute coil .....	54
2.3.1 Governing electromagnetic equations .....	56
2.3.2 Extent of the simulation domain .....	58
2.3.3 Mesh assignment .....	59
2.3.4 Conductivity of the air domain .....	63
2.3.5 Computed impedance with the optimized model parameters .....	65
2.4 FEM analysis of a split-D differential coil .....	66
2.4.1 Extent of the simulation domain .....	68
2.4.2 Mesh size .....	69
2.4.3 Conductivity of the air domain .....	71
2.4.4 Simulation results and discussion .....	72
2.5 Summary and conclusions .....	78
CHAPTER 3 ADAPTIVE NEURO-FUZZY INFERENCE SYSTEM TRAINED FOR SIZING SEMI-ELLIPTICAL NOTCHES SCANNED BY EDDY CURRENTS .....	81
3.1 Introduction .....	81
3.2 Experiments and modelling .....	85
3.2.1 Lift-off and tilt studies .....	91
3.2.2 Size dependent signals for ANFIS training .....	96
3.3 Adaptive neuro-fuzzy inference system .....	97
3.4 Conclusions .....	101

CHAPTER 4     A RELIABILITY STUDY ON AUTOMATED AND MANUAL  
                  EDDY CURRENT TESTING .....103

4.1     Introduction.....104

4.2     ECT POD variables.....107

4.3     Experimental procedure .....109

4.4     Noise Treatment.....112

4.5     Numerical modeling for orientation study .....116

4.6     Effect of crack orientation on signal amplitude .....118

4.7     POD of automated and manual tests .....122

4.8     Conclusions.....126

CONCLUSION.....129

RECOMMENDATIONS .....135

APPENDIX I     A MODEL-BASED STUDY OF THE EFFECT OF SEMI-  
                  ELLIPTICAL SURFACE NOTCH GEOMETRY ON THE SIGNAL  
                  OF A SPLIT-D EDDY CURRENT PROBE .....147

APPENDIX II     SENSITIVITY OF EDDY CURRENT SIGNALS TO PROBE’S  
                  TILT AND LIFT-OFF WHILE SCANNING SEMI-ELLIPTICAL  
                  SURFACE NOTCHES - A FINITE ELEMENT MODELING  
                  APPROACH .....149

BIBLIOGRAPHY.....151

## LIST OF TABLES

	Page
Table 2.1 Dimensions and material properties of the commercial split-D probe's components. ....	52
Table 3.1 Geometry of semi-elliptical EDM notches. ....	87
Table 3.2 Dimensions of semi-elliptical EDM notches used in the simulations. ....	90
Table 3.3 Set of inputs and output that are used in the form of a vector to train a grid type ANFIS. ....	97
Table 3.4 Nominal length and the length estimated by the trained FIS for 3 calibration and 5 model-based EDM notches. ....	99
Table 4.1 List of parameters causing variations in ECT signals during automated and hand scans. ....	108
Table 4.2 List of parameters examined in this work for monitoring their effect on the distribution of ECT response. ....	109
Table 4.3 The length interval studied through modelling for each specific orientation. ....	118
Table 4.4 POD parameters for automated scans. ....	124
Table 4.5 POD parameters concerning the manual scans at different frequencies. ....	125
Table 6.1 Procedures used in preparation of samples to study hydrogen embrittlement. ....	138



## LIST OF FIGURES

	Page
Figure 1.1 (a) Self-induction for a current carrying coil (Hellier, 2013) and, (b) interaction between the coil's electromagnetic field and the conductor leading to formation of ECs (Hellier, 2013).....	13
Figure 1.2 Transformation from (a) an impedance plane to (b) a normalized impedance plane (Hellier, 2013).....	14
Figure 1.3 (a) Current density versus the penetration depth (Hellier, 2013), (b) changes in ECs' phase versus their depth of penetration (Hellier, 2013).....	16
Figure 1.4 (a) Absolute and (b) reflection differential configurations of ECT probes (García-Martín et al., 2011) .....	17
Figure 1.5 (a) 3-D model of a split-D probe reconstructed by X-ray tomography and sectioned in half, and (b) microscopic image taken from the split-D probe's tip. ....	18
Figure 1.6 (a) 3-D assembly model for TEAM problem 8. Scan directions modelled through FEM and the structure of the reflection differential surface probe used in simulations (Rosell & Persson, 2011), and (b) four different levels of the vector potential's amplitude/maximum amplitude ratio and the truncation box defined on that basis (Rosell & Persson, 2011).....	22
Figure 1.7 (a) Simplified closed fatigue crack model containing non-zero conductivity region proposed by (Rosell & Persson, 2012a), and (b) relevant input parameters that were accounted for in signal response POD by (Rosell & Persson, 2012b).....	24
Figure 1.8 Experimental peak-to-peak voltage versus the notch opening for two types of rectangular and semi-circular notches, each having two different dimensions. Extrapolated model-based curves for the larger notches were superimposed on the experimental curves. Tests were carried out at frequency of 2 MHz on samples of Ti-6246 (Norio Nakagawa et al., 2009) .....	26
Figure 1.9 Comparison between the impedance data measured by impedance spectroscopy and those obtained from VIC 3D <sup>®</sup> and COMSOL modelling for a rectangular notch with 12.6 mm in length, 5 mm in depth, and 0.28 mm in width. The results for (a) an absolute air-cored probe, (b) a split-D air-cored differential probe scanning rectangular surface notches(Brown & Eviston, 2017) .....	27

Figure 1.10 Comparison between the impedance data measured by IA, UniWest ECT unit, and those obtained from VIC 3D<sup>®</sup> and COMSOL modelling for a rectangular notch with 12.6 mm in length, 5 mm in depth, and 0.28 mm in width. The results for (a) an air-cored (R. D. Mooers & Aldrin, 2016a) and (b) a ferrite cored split-D probe (R. D. Mooers & Aldrin, 2016a).....28

Figure 1.11 (a) D-coils' assembly rotation about Z axis and tilt in two different planes (R. D. Mooers & Aldrin, 2016b), and (b) variations of the real and imaginary parts of the probe's impedance with its D-coil assembly tilted by -10° and 10° in XZ plane (R. D. Mooers & Aldrin, 2016b).....30

Figure 1.12 Membership functions of X and Y as the two inputs of a Sugeno system, and the surface output of the inference system (Jang et al., 1997).....34

Figure 1.13 (a) Regression line along with the upper and lower confidence bonds for  $\hat{a}$  vs.  $\log(a)$  data (Annis, 2009), and (b) POD curve and 95% confidence bonds (Annis, 2009).....40

Figure 1.14 Two-point normalization applied to raw data and the resulting POD curve is compared to the POD curve plotted for raw data for (a) EDM (Lemire et al., 2010), and (b) fatigue cracks (Lemire et al., 2010).....42

Figure 1.15 POD parameters for (a) different test frequencies and crack locations (P. Underhill & T. Krause, 2011a), and (b) different probes and frequencies (P. R. Underhill & T. W. Krause, 2011).....43

Figure 1.16 POD parameters are compared for mid-bore and corner cracks grown in drilled holes as well as the actual bolt holes of in-service components (P. R. Underhill & Krause, 2016) .....44

Figure 2.1 (a) 3-D model of the split-D probe showing coils, cores and magnetic shielding (b) zoom on the probe's tip taken with a confocal optical microscope. The outer driver coil and the inner receiver coils are green and red, respectively .....53

Figure 2.2 (a) Experimental setup for measuring the split-D probe's differential impedance as the probe scans three reference notches with different depths in aluminum (b) schematic of the split-D probe's orientation and scan direction with respect to an EDM notch .....54

Figure 2.3 The 3D-half model developed in Comsol to reproduce the results presented in (Burke, 1988) for an absolute coil EC probe. A circular coil, a defective plate and the encompassing air domain are shown.....55

- Figure 2.4 Contour of the  $\varphi$  component of the magnetic vector potential  $A$  given by a 2D-axisymmetric model of an absolute coil located over an extremely large (500 mm×500 mm×12 mm) un-defective sample.  $r$  and  $z$  values are in mm. According to (Burke, 1988), simulation is performed with an operating frequency of 900 Hz .....59
- Figure 2.5 Effect of the element size on the normalized computed absolute coil's (a) resistance and (b) inductive reactance as it scans an aluminum block containing a notch, (c) Schematic of the coil position with respect to the notch location. Results are normalized by the magnitude of impedance variation in the Burke's measurements (Burke, 1988) .....62
- Figure 2.6 Effect of the number of boundary layers applied in the first three eddy current penetration depths on the normalized computed absolute coil's (a) resistance and (b) inductive reactance as the coil scans an aluminum block containing a notch. Results are normalized by the magnitude of impedance variation in the Burke's measurement (Burke, 1988).....63
- Figure 2.7 Effect of air conductivity on the normalized computed absolute coil's (a) resistance and (b) inductive reactance as the absolute coil scans an aluminum block containing a notch. Results are normalized by the magnitude of impedance variation in the Burke's measurements (Burke, 1988) .....64
- Figure 2.8 Calculated values of the absolute coil's (a) resistance and, (b) inductive reactance as the coil scans over a notch. Comparison with impedance measurements extracted from Burke's work (Burke, 1988).....66
- Figure 2.9 (a) Contour map of the magnetic vector potential component perpendicular to the symmetry plane at 500 kHz for a split-D probe over an un-defective aluminum block, (b) model's mesh distribution for a split-D probe scanning an aluminum block with a 0.503 mm deep notch .....69
- Figure 2.10 Effect of the element size on the normalized computed (a) real and (b) imaginary parts of the differential impedance for a 0.188 mm deep notch in an aluminum block. Simulations are performed using four different numbers of volumetric tetrahedral elements .....70
- Figure 2.11 Effect of the element size on the normalized computed (a) real and (b) imaginary parts of the differential impedance for 1.008 mm deep notch in an aluminum block. Numerical simulations are performed using four different numbers of volumetric tetrahedral elements .....71

Figure 2.12 Effect of air conductivity on the normalized computed (a) real and (b) imaginary parts of the differential impedance for 1.008 mm deep notch in an aluminum block. Numerical simulations are performed for three different values of the air conductivity .....72

Figure 2.13 Imaginary (a) and real (b) parts of the differential impedance obtained through numerical calculation and measurement with the Nortec-500 flaw detector for a 1.008 mm deep notch in an aluminum block.....73

Figure 2.14 Imaginary (a) and real (b) parts of the differential impedance obtained through numerical calculation and measurement with the Nortec-500 flaw detector for a 0.503 mm deep notch in an aluminum block.....74

Figure 2.15 (a) Imaginary and (b) real parts of the differential impedance obtained through numerical calculation and measurement with the Nortec-500 flaw detector for a 0.188 mm deep notch in an aluminum block.....75

Figure 2.16 Single loop of the 8-shaped signals obtained by plotting the imaginary and real parts of the probe’s impedance (Figures 2.13, 2.14 and 2.15) directly on the impedance plane. (a) 1.008 mm , (b) 0.503 mm and (c) 0.188 mm deep notch.....76

Figure 2.17 Distribution of the z and x components of the induced current density, represented by a vector field, in the vicinity of the 0.188 mm deep notch as the probe is displaced by (a) 0 mm, (b) 0.6 mm and (c) 1.2 mm. Side view of the scan shows the distribution of the x and y components of the magnetic field intensity .....78

Figure 3.1 Geometrical features of a semi-elliptical notch.....87

Figure 3.2 (a) Setup for measuring the probe’s impedance as it scans the notches, (b) direction of the raster scan relative to the notch length, and (c) representation of the lift-off distance and tilt angle applied to the probe ..87

Figure 3.3 (a) Cut in half 3D reconstruction of X-Ray tomography images of the split-D probe, (b) the probe and sample assembly model prepared within Comsol showing a small meshed region in close proximity to the notch geometry.....88

Figure 3.4 Comparison between the measured and simulated signals of (a) notch A, (b) notch B, and (c) notch C at two different lift-offs of 100 and 140  $\mu\text{m}$ .....92

Figure 3.5 Effect of lift-off variations on the ECT signal of (a) notch A, (b) notch B, and (c) notch C.....93

Figure 3.6 Comparison between the measured and simulated signals of (a) notch A, (b) notch B, and (c) notch C for two probe tilts of  $2^\circ$  and  $4^\circ$  .....94

Figure 3.7 Effect of the probe's tilt angle variations on the signal of (a) notch A, (b) notch B, and (c) notch C .....	94
Figure 3.8 Variations of the probe's signal amplitude as it scans three notches A, B and C versus the probe's (a) lift-off, and (b) tilt angle.....	95
Figure 3.9 (a) Variations of the form of the probe's signal as it scans 6 different notches with different dimensions and (b) three signal shape categories used for training ANFIS.....	97
Figure 3.10 (a) Maximum signal amplitude and width shown on a simulated signal of notch A and (b) structure of a three inputs/single output ANFIS (Jang et al., 1997) .....	98
Figure 3.11 Percentage of additional error introduced into the length estimation of notch A and C because of the probe's (a) lift-off and (b) tilt angle variations.....	100
Figure 3.12 Variations of the normalized maximum amplitude of three notches A, B and C as the probe's (a) lift-off and (b) tilt angle change .....	100
Figure 4.1 Experimental setup for performing automated ECT scans.....	111
Figure 4.2 (a) relative orientation represented by the angle $\theta$ , which is defined by the crack line and scan direction, and (b) peak-to-peak amplitude of an 8-shape ECT signal .....	111
Figure 4.3 Typical noise recorded during manual scan and the windows selected for processing.....	113
Figure 4.4 Variations of the percentage of noise level normalized by the calibration signal amplitude as angle between the probe scan direction and machining tool marks orientation changes. Results are presented for 3 frequencies for both manual and automated scans.....	115
Figure 4.5 Optical laser microscope images and samples of the surface roughness profile for (a) $0^\circ$ , (b) $45^\circ$ , and (c) $90^\circ$ angles that the probe's scan direction makes with the orientation of tool marks on surface. (d) orientation of tool marks <i>versus</i> $R_a$ .....	115
Figure 4.6 Comparison between the measured signal from a crack and simulated signal for a notch for a (a) 2.92 mm and (b) 1.5 mm long crack/notch oriented at $0^\circ$ .....	117
Figure 4.7 Normalized signal amplitudes <i>versus</i> $L/D$ ratio for orientations of $0^\circ$ , $45^\circ$ and $90^\circ$ at frequencies of (a) 0.5 MHz and (b) 1 MHz.....	119

- Figure 4.8 Simulated and measured normalized signal amplitudes *versus*  $L/D$  ratio for orientations of  $0^\circ$ ,  $45^\circ$  and  $90^\circ$  at 1 MHz.....120
- Figure 4.9 Contours of current density norm distribution on the surface of a sample. The probe center is located 0.3 mm away from the notch center. Notches with lengths of (a) 2 mm, (b) 4 mm, and (c) 6 mm are investigated .....122
- Figure 4.10 Regression lines found for  $\hat{a}$  vs.  $a$  data and related POD curves plotted for automated scans with indexes of (a) 0.5 mm, (b) 1.25 mm and (c) 2.5 mm.....124
- Figure 6.1 Screen of Nortec 500S showing (a) the effect of test frequency on lift-off traces for three samples of I, E and A, (b) rotated horizontally lift-off traces at 200 kHz for three samples I, E and A, (c) overlapping of the lift-off traces of samples I and A recorded collectively from different spots on their surface.....141
- Figure 6.2 (a) 3-D model reconstructed from CT-scan image stack of the reflection absolute surface probe showing coils and cores, and (b) X-ray image of the probe along with its axis of symmetry .....143
- Figure 6.3 (a) Axisymmetric 2-D model for assembly of probe, sample and air domain prepared in Comsol and, (b) 3-D model of magnetizer's assembly and SAE 4340 sample.....144
- Figure 6.4 Magnetic field density (a) inside different domains of the assembly including the SAE 4340 sample, and (b) inside the SAE 4340 sample after applying 1.6 T high pass filter .....145

## LIST OF ABBREVIATIONS

2-D	Two Dimensional
3-D	Three Dimensional
AC	Alternating Current
AI	Artificial Intelligence
AMS	Aerospace Material Specification
ANFIS	Adaptive Neuro-Fuzzy Inference System
ASTM	American Society for Testing and Material
AWG	American Wire Gauge
BEM	Boundary Element Method
CNRC-NRC	National Research Council Canada
CRIAQ	Consortium de Recherche et d'Innovation en Aérospatiale au Québec
DC	Direct Current
DPHM	Diagnosis, Prognosis, and Health Monitoring
DT	Damage Tolerance
EC	Eddy Current
ECT	Eddy Current Testing
EDM	Electrical Discharge Machined
EMF	Electromotive Force
ETS	École de Technologie Supérieure
FAA	Federal Aviation Administration
FDM	Finite Difference Method
FEM	Finite Element Method/Model

FIS	Fuzzy Inference System
FL	Fuzzy Logic
HE	Hydrogen Embrittlement
IA	Impedance Analyzer
LSE	Least-Squares Estimator
MANU	Manufacturing
MAPOD	Model-Assisted Probability of Detection
MF	Membership Function
NASA	National Aeronautics and Space Administration
NDE	Non-Destructive Evaluation
NDT	Non-Destructive Testing
NLSE	Nonlinear Least-Squares Estimator
NN	Neural Networks
PDE	Partial Differential Equation
POD	Probability of Detection
POFI	Probability of False Indication
QNDE	Quantitative Non-Destructive Evaluation
SC	Soft Computing
TEAM	Testing Electromagnetic Analysis Methods

## LIST OF SYMBOLS AND UNITS OF MEASUREMENTS

$\delta$	Standard Penetration Depth of Eddy Currents
$\epsilon$	Electrical Permittivity
$\mu$	Permeability
$\mu_0$	Permeability of Free Space
$\mu_r$	Relative Permeability
$\rho$	Charge Density
$\sigma$	Electrical Conductivity
$\omega$	Angular Frequency
$\Delta R$	Variations of Resistance
$\Delta X$	Variations of Inductive Reactance
$\Delta Z$	Impedance Variations
$\Omega$	Ohm
$^{\circ}\text{C}$	Celsius Degree
$a$	Flaw Size
$a_{50}$	Average flaw size that is detected 50% of the times
$a_{90}$	Average flaw size that is detected 90% of the times
$a_{90/95}$	Flaw Size that is detected 90% of the times with 95% of confidence
$\hat{a}$	Signal Amplitude
$\hat{a}_{dec}$	Signal amplitude that discriminates rejected from accepted parts
$\hat{a}_{sat}$	Signal amplitude saturation level

## XXIV

$\hat{a}_{th}$	Noise amplitude level
A	Ampere
$A$	Electromagnetic Vector Potential
$B$	Magnetic Field Density
$D$	Electrical Field Density
$E$	Electrical Field Intensity
$f$	Test Frequency
H	Henry
$H$	Magnetic Field Intensity
Hz	Hertz
$J_0$	Electrical Current Density on Surface of Material
$J_e$	Externally Applied Electrical Current Density
ksi	Kilopound per Square Inch
$l$	Length of Magnetic Path
$L$	Inductance
L	Scan Line Parallel to the Notch Length
$L_0$	Inductance of the Coil Placed in Air
$N$	Number of Coil Turns
$R$	Resistance
$R_0$	Resistance of Wires
S	Siemens
T	Scan Line Perpendicular to the Notch Length

$X$  Inductive Reactance

$Z$  Impedance



## INTRODUCTION

### **Problem statement**

### **Why quantitative non-destructive evaluation is important?**

Manufacturing high quality systems and ensuring their integrity throughout their expected service life has been the concern of many industries for years. Different non-destructive testing (NDT) methods are developed/evolved to meet the industrial needs for quality control during the past century and it was not long after the World War II when their importance was rocketed. Following a catastrophic failure of an aircraft fuselage from Aloha airlines in 1987, the safety measures became tighter in aerospace industry. This incident thrust the growth of public awareness about airworthiness. Following this accident, many conferences and meetings were held regarding this matter in order to gather NDT experts and collect their recommendations. As the outcome of these meetings, many research projects were put in place to develop new techniques for inspection of ageing aircraft, and to expand the knowledge and practice of quantitative non-destructive evaluation (QNDE) (Achenbach & Thompson, 1991). Since 1978, many fatigue/fracture-critical components of aircraft structures have been mandated by Federal Aviation Administration of US (FAA) to be designed based on the damage tolerance (DT) design principles (Pitt & Jones, 1997). The lifing philosophy strongly depends on the reliable defect detection and sizing results provided by QNDE methods. DT approaches use fracture mechanic models to analyze and predict the integrity of designed components. Based on these models, it is possible to estimate the largest defect size that can be tolerated by taking into account the material properties, loading conditions and the location of stress concentration in the critical crack site. Accordingly, the defect size that can be reliably detected by the NDT system, and would not grow larger than the critical size until the next scheduled inspection, shall be repaired and kept in service. Therefore, based on life-assessment procedures, the planning for periodical non-destructive inspection can be determined by the defect size that is reliably detected. The possibility of sizing these defects using the selected NDT method stands as a guide to such plannings. This

fact highlights the importance of QNDE in the safety maintenance of aircraft structures (Achenbach & Thompson, 1991).

### **Why eddy current split-D differential surface probes?**

As the first step in inspection, it is essential to select the NDT method to best fit the intended applications, meaning that the capability of NDT system in detection of the flaw type of interest should be determined in advance. Fatigue failure of metallic aircraft components has resulted in many devastating accidents in the industry (Schijve, 1994). Fatigue cracks frequently form and grow within aircraft fuselage and engine components exposed to cyclic loads during their service life. If such cracks are open to surface, NDT methods such as visual testing, liquid penetrant inspection, and eddy current testing (ECT) are preferred for inspection. However, due to tight opening and small size of fatigue cracks, sometimes they can be detected neither by visual inspection nor by liquid penetrant method. ECT offers high sensitivity and detection reliability in dealing with such tiny cracks. Additionally, ECT method has gained a high acceptance in industries owing to factors such as the ease of application, minimum surface preparations and possibility of inspection over paint layers. Therefore, a number of ECT surface probes dedicated to detection of small narrow surface discontinuities have been developed and employed in past years. From this category, the split-D reflection differential surface pencil probes are best suited for detecting fatigue cracks for which the opening is very tight and the dimensions are small at the early stages of their growth. The probe is comprised of a circular driver and two D-shaped receiver coils. The differential configuration of oppositely wound receiver coils renders the probe insensitive to gradual variations of conductivity and permeability of test subject. Furthermore, their small sizes as well as the exceptional spatial stacking of the coils and ferrite cores inside them provide high sensitivity to abrupt changes of the surface features such as a breaking.

### **How to characterize defects using split-D probe's signal (inversion)?**

For defect characterization and sizing, it is essential to develop a forward model based on the underlying physical principles of the chosen NDT method, which is ECT in the present research. Forward models are used to predict the response of a testing method for a given material containing defects of known nature. These models are mainly developed analytically/semi-analytically based on the set of Maxwell's equations for relatively simple problem assemblies involving the geometry of the ECT probe and the defect. Additionally, these models can be used as the core of inversion algorithms for characterization of an unknown defect based on the response of ECT system. In general, many of these algorithms aim to minimize the difference between predictions of the forward model and response of ECT system by readjusting model parameters iteratively. Therefore, forward models incorporated within the inversion algorithms should be computationally efficient since numerous iterations might be required for a model to minimize the difference between its response and that of ECT. Moreover, coupling these inversion algorithms with time-consuming conventional numerical methods, as a forward model, makes it impossible to perform real-time inversion.

Fortunately, owing to rapid advances in the field of soft computing (SC), nowadays, it is a more common practice to employ new SC strategies in inversion of NDT responses. In contrast to hard computing techniques based on solid binary logic that signifies precision and categoricity, SC engines provide tolerance of approximation since they have the human mind as their role model. To form SC engines, one would be able to integrate two or more different artificial intelligence (AI) techniques such as fuzzy logic (FL), neural networks (NN) and genetic algorithms. In this context, NN and FL are more frequently used together either in series or as an integration to form hybrid systems, in which the reasoning and inference power of FL can be complemented by adaptive learning nature of NN. These systems are great alternatives to the other complex inversion algorithms because of their high adaptability to changes, learning capability, simplicity of use, and low complexity of the theory. In case of ECT inversion, neuro-fuzzy hybrid systems could be directly trained using known

geometrical characteristics of defects and features of the corresponding signals as outputs and inputs, respectively. To obtain the input/output data, one method is to prepare a large set of samples containing defects of known geometries although; such experiments could be very costly. As an alternative, one could use the outcome of the numerical discretization techniques such as finite element modelling (FEM) to produce such data to train SC engines.

FEM is a diverse numerical method capable of dealing with complex geometries and modelling of inhomogeneous media. FEM simulations of low frequency ECT are mainly carried out based on a differential equation in frequency domain derived from the quasi-static approximation of Maxwell's equations. The solver time for frequency domain formulation is markedly lower than that of time transient solutions. FEM has been previously used to model the interaction of eddy currents (EC) with different types of flaws. However, related studies devoted to differential probes are limited in number and thus, the competency of such tools to model these probe types requires further research. Additionally, EC signal predictions by FEM for arbitrarily sized defects could provide a foundation for many inexpensive model-based QNDE studies such as reliability assessment and defect characterization.

### **How to determine the reliability of inspection?**

As another crucial step in QNDE, the reliability of the NDT method shall be assessed. It is well known in the field of NDT that different inspectors report different results for inspection of the same flaw. Such discrepancies are not only a matter of human error, but also could occur due to changes in non-destructive evaluation (NDE) system parameters and environmental conditions. Statistical analysis of inspection results, which considers inspection uncertainties, provides useful information on the probability of false indication (POFI) and probability of detection (POD). In industry, POD curves are used as a measure to quantify the detection reliability affected by the inspection system parameters. As an advantage, POD and POFI enable us to compare the reliability of detection for different NDE systems used for the same application. As implied earlier, the detectable defect size plays an

important role in life assessment models used for planning inspections. In this context, the higher reliability of NDE system results in higher POD and longer inspection intervals.

### **Why automated eddy current testing?**

Recent advances in robotics have allowed industrialists to integrate new automated systems with innovative inspection techniques. In contrast to traditional approaches, employing these systems provides advantages such as shorter inspection time and lower labor cost while gaining an increased repeatability for scans. However, automated systems still need further improvements. In automated ECT, the imprecisions associated with the positioning and handling of probe during robotic scans can result in acquisition of erroneous signals. This in turn could give rise to misinterpretations of the signal and thus, taking wrong decision and actions. To address these issues, probe manipulation imprecisions, which are manifested by lift-off and tilt in ECT, are highly important and shall be investigated through modelling and experiments.

### **Summary**

Nowadays, as the main challenge in NDT society, characterization and reliable sizing of defects are the subjects of a lot of ongoing research work. This is only achievable through development of reliable inversion algorithms. These algorithms are more frequently established in two ways; a) coupling an optimization algorithm with forward models developed according to physical principles of the NDT method, and b) developing SC algorithms using the AI methodologies and training them by input/output data. The first case requires development of either analytical or semi-analytical formulations, the derivation of which can be very awkward for complex problem geometries in electromagnetics. The second approach is less complicated and more flexible. To these algorithms, the input can be the characteristics of the NDT signal acquired for the defects while the output stands for the dimensions of the corresponding defect. Normally, to collect such input/output data, one needs to have access to a large set of defects with diverse geometries in order to provide

enough training for SC algorithms. Fortunately, this data could be generated through numerical modelling approaches, such as FEM. However, like the analytical approach, numerical models should also be validated through experiments. Apart from defect sizing, the reliability of detection should also be taken into account in QNDE studies. Regardless of the chosen NDT method, inspection responses are accompanied by variabilities. These variabilities are majorly introduced by parameters such as human, environment, and inspection system. To account for all the influential factors and provide a measure for the reliability of inspection, POD analyses can become handy statistical tools.

### **Research objectives**

This research was conducted to fulfill the objectives of two projects titled as MANU-418 and DPHM-601, which were conceived by *Consortium de Recherche et d'Innovation en Aérospatiale au Québec* (CRIAQ). The first project started in 2011 and completed in 2015. Three universities (*École de technologie supérieure* (ETS), *Université Laval* and Concordia University) as well as two industrial partners (Pratt and Whitney Canada, and L-3 MAS) were involved in this project. MANU-418 was mainly focused on performing automated NDT surface inspections of components using a 6-axis MOTOMAN robotic arm in order to locate and size the potential flaws. During this project, we had the support of National Research Council Canada (CNRC-NRC). The second ongoing project is defined by CRIAQ and started in 2015. Three universities (ETS, *Université de Montréal*, and *École Polytechnique de Montréal*) were involved in this collaborative effort along with industrial partners including Safran, *Héroux-Devtek*, and Bell Helicopter. The project aims to develop a NDT method to detect and evaluate hydrogen embrittlement in high strength steels.

### **Research Contributions**

The present dissertation is a part of a larger study carried out in the framework of the aforementioned projects. The priority of the dissertation is to scrutinize and deliberate over the ECT of surface flaws through both experiments and numerical simulations in order to

satisfy the objectives of MANU-418 project. The followings stand for the original contributions of the present research in accordance to the MANU-418 project objectives. These contributions are presented in form of three journal papers embodied in chapters 2 to 4 of this dissertation and two conference presentations for which the abstracts are presented in APPENDIX I and II. The following provides a list of these publications in a chronological sequence:

- Ehsan Mohseni, Martin Viens, Demartonne Ramos França, « A Model-Based Study of The Effect of Semi-Elliptical Surface Notch Geometry on The Signal of a Split-D Eddy Current Probe » In *NDT in Canada 2016 & 6th International CANDU In-Service Inspection Workshop*, November 15-17, 2016, Burlington, Ontario, Canada.
- Ehsan Mohseni, Martin Viens, « Sensitivity of Eddy Current Signals to Probe's Tilt and Lift-Off While Scanning Semi-Elliptical Surface Notches - A Finite Element Modeling Approach ». In *NDT in Canada 2017*, June 6-8, Quebec City, Quebec, Canada.
- Ehsan Mohseni, Demartonne Ramos França, Martin Viens, Wen Fang Xie, Baoguang Xu, « Finite Element Based Modelling of Surface Cracks Scanning Using a Reflection Differential Split-D Eddy Current Probe ». Submitted to *Journal of Nondestructive Evaluation* in June 2018.
- Ehsan Mohseni, Martin Viens, Wen-fang Xie, « Adaptive Neuro-Fuzzy Inference System Trained for Sizing Semi-Elliptical Notches Scanned by Eddy Currents ». Submitted to *Journal of Nondestructive Evaluation* in June 2018.
- Ehsan Mohseni, Hamid Habibzadeh Boukani, Demartonne Ramos França, Martin Viens, « A Reliability Study on Automated and Manual Eddy Current Testing ». Submitted to *Journal of Nondestructive Evaluation* in July 2018.

Paper #1, « Finite Element Based Modelling of Surface Cracks Scanning Using a Reflection Differential Split-D Eddy Current Probe », aims at evaluating the capacity and reliability of the FEM in simulation of absolute as well as differential ECT surface probes. The study covers the design and development of a FEM representing the interaction between a simple air-cored ECT probe and electrical discharge machined (EDM) surface notches. The design

of the probe and notches as well as the material properties were set to be identical to the ones used in a benchmark ECT study (Burke, 1988). Afterwards, the predictions of the model were compared to impedance measurements of the benchmark study. Moreover, the interaction between electromagnetic field of a split-D surface probe and rectangular through-width notches were simulated. Subsequently, to check the validity of the model, ECT signals generated by FEM simulations were compared with the experimental results. The simulations were carried out using COMSOL Multiphysics®, which is a commercially available FEM software.

Paper #2, « Adaptive Neuro-Fuzzy Inference System Trained for Sizing Semi-Elliptical Notches Scanned by Eddy Currents », considers the development of the FEM representing the interaction of the electromagnetic field of the split-D probe with semi-elliptical surface EDM notches. Subsequently, the validation of the model was carried out through comparing the model output with the outcomes of experiments. The sensitivity of ECT signals to common robotic positioning errors, emerging as probe's lift-off and tilt during automated scans, were also studied and discussed. Followed by the model validation, semi-elliptical notches possessing different dimensions were modelled to constitute a size dependent table of ECT signals. Afterwards, the table of the model-generated ECT signals was utilized to train a SC algorithm for notch length estimation. Finally, the influence of variations in ECT signals, due to the robotic positioning errors, on the sizing results was studied.

Paper #3, « A Reliability Study on Automated and Manual Eddy Current Testing », holds a discussion regarding the assessment of the reliability of manual and automated inspections conducted by ECT split-D probe. In the study, the noise level connected to each scan technique is evaluated. The dependency of noise on surface roughness orientation as well as frequency is investigated. Additionally, the effect of crack orientation on variations of the signal amplitude for this probe is studied. Finally, POD curves were extracted by carrying out manual and automated inspections on several AISI 410 martensitic steel samples at three different frequencies. Consequently, the extracted noise levels and POD curves acquired for one technique were compared to that of the other.

Furthermore, as required by DPHM-601 project, the effect of hydrogen in martensitic SAE 4340 steel on the ECT probe's impedance was investigated through FEM and experiments. The results and observations are partly discussed in the recommendation section of this dissertation.

### **The structure of thesis**

The present thesis is structured in 4 chapters. The first chapter is devoted to the review of previously published papers in the field of ECT. This chapter provides a better insight into the concepts of ECT modelling, reliability studies, and SC.

Second chapter encompasses the first submitted paper entitled "Finite Element Based Modelling of Surface Cracks Scanning Using a Reflection Differential Split-D Eddy Current Probe". The chapter explores the possibility of developing FEM for ECT split-D probe and studies the interaction between its electromagnetic field and the surface notches.

The second paper submitted with the title of "Adaptive Neuro-Fuzzy Inference System Trained for Sizing Semi-Elliptical Notches Scanned by Eddy Currents" is presented in the third chapter. This chapter presents numerical studies regarding the ECT signal variations caused by the probe's tilt and lift-off. Furthermore, details of using SC for inversion of ECT signals are discussed.

The final chapter presents the third submitted paper with the title of "A Reliability Study on Automated and Manual Eddy Current Testing". In this chapter, the noise levels and PODs are extracted for both automated and manual inspections. Accordingly, the comparison between the two techniques is discussed in details.



## **CHAPTER 1**

### **LITERATURE REVIEW**

This chapter aims to review the concepts of ECT and its modelling as well as the application of AI and POD for ECT. Therefore, each of the following subsections is devoted to one of these subjects. Subsection one contains the physical principles of ECT, the main parameters affecting the signal of ECT and, different approaches that have been employed to model the ECT of surface notches with an emphasis on FEM. Subsection two provides a brief introduction to the basics of SC. In addition, a number of studies concentrated on classifying and sizing surface flaws by means of SC algorithms are reviewed there. In the last subsection, the statistical reliability study used for NDE systems is explained in summary. Furthermore, the application of such studies in ECT is described and the related published researches on this subject are presented.

#### **1.1 Eddy current testing**

Inspection of manufactured parts and systems during their service life is essential in order to ensure that they meet the design expectations and have a safe functionality during the specified period of service. These inspections shall be carried out in a proper way to not impair their properties and performance (Blitz, 2012). Non-destructive test methods used for such inspections have gained importance due to the rapid technological progress during the past 60 years in various industries such as transportation and energy, where the risks are high and strict precautions are required. In general, NDT name is assigned to a variety of methods and techniques concerned with quality, serviceability and integrity of a wide range of structures. Particularly in transportation industry, structures demand reliable, accurate and fast NDT solutions in order to avoid catastrophic accidents. ECT is one of the well-known electromagnetic NDT methods that is frequently used for these purposes. It is widely used to inspect conductive ferromagnetic and non-ferromagnetic materials since the method provides high sensitivity to surface and near surface flaws. ECT found its way to the aerospace industry in early years of its application when the aircraft structures were majorly made of

aluminum alloys. About 30 years into the service life of the first fleets, tragedies started to take place due to the fatigue failures. Ageing of airframes causes the material characteristics to degrade in components. In addition, all components are subjected to cyclic loads associated with taxing, pressurization, takeoff, landing, and depressurization. The changes in material characteristics along with the in-service cyclic loads in these structures mostly promote the formation of fatigue-induced cracks and stress corrosion cracks for which, very often, ECT is the preferred NDT method.

### 1.1.1 Electromagnetic induction

Placing a conductor loop in a time varying magnetic field brings about the electromagnetic induction process. In the process, an electromotive force (EMF) is induced in the conductor loop according to the Faraday's induction law. EMF produces a current flow in the loop where the induced voltage is proportional to the applied magnetic flux as shown in Equation 1.1.

$$\mathcal{E} = -\frac{\partial\Phi}{\partial t} \text{ (V)} \quad (1.1)$$

In this equation, the negative sign indicates the direction of EMF according to the Lenz's law. As implied by this law, the current flowing in the loop is directed in a manner to generate a secondary field opposing the one that produced the current. In a more general case, when a solenoid is connected to an alternating current (AC) generator, as demonstrated in Figure 1.1(a), it is placed in its own electromagnetic field. The field alternates with the same frequency as the injected current does and therefore, a back-EMF is applied across the solenoid according to Equation 1.1. The potential difference across an ideal coil, with no ohmic resistance, is 90° out of phase relative to current flowing in it. Therefore, the out of phase voltage resists the changes of the current in the coil. This type of resistance formed by the coil self-inductance ( $L$ ) is called inductive reactance ( $X$ ). AC resistance of the coil, or so-called impedance ( $Z$ ), is a complex value comprised of  $X$  as the imaginary part along with the

Ohmic resistance ( $R$ ) of the wires as the real part. Equation 1.2 shows the impedance  $Z$  as a function of  $X$  and  $R$ .

$$Z = \sqrt{(\omega L)^2 + R^2} \text{ } (\Omega) \quad (1.2)$$

As shown in the Equation 1.2,  $X$  itself is a function of both  $L$  and angular frequency ( $\omega$ ). According to Equation 1.3, inductance of a long solenoid is directly proportional to relative permeability of the core inside the coil ( $\mu$ ), square of the coil turns ( $N$ ) as well as the cross sectional area of the coil ( $A$ ). Besides, it is inversely proportional to the length of the magnetic path.

$$L = \mu_0 \mu_r \frac{N^2 A}{l} \text{ } (H) \quad (1.3)$$

In Equation 1.3,  $\mu_0$  is the permeability of the free space,  $\mu_r$  is the relative permeability of the core, and  $l$  stands for the magnetic path (Hellier, 2013).

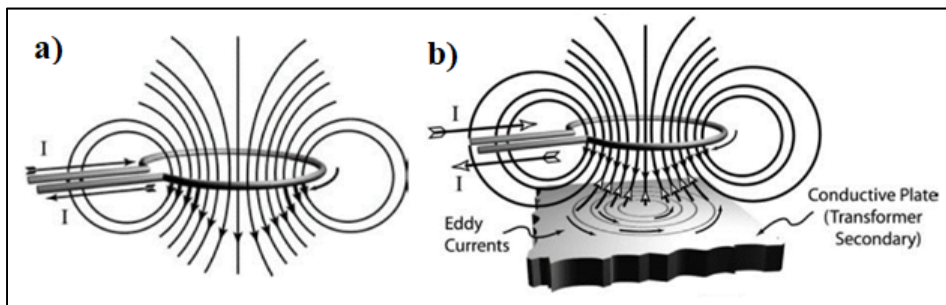


Figure 1.1 (a) Self-induction for a current carrying coil (Hellier, 2013) and, (b) interaction between the coil's electromagnetic field and the conductor leading to formation of ECs (Hellier, 2013)

As depicted in Figure 1.1(b), when a current carrying loop is brought near to a conductive component, the time varying electromagnetic field produced by the loop penetrates the component. Consequently, according to the Faraday's law of induction, the induced EMF within the sample triggers the flow of circular and continuous currents called ECs. As stated

by Lenz's law, the ECs flow in a direction to produce a secondary magnetic field that opposes the changes in primary one (García-Martín, Gómez-Gil, & Vázquez-Sánchez, 2011; Shull, 2016). The opposition of secondary field forms a reduced net flux in the loop in case of non-ferromagnetic conductors. As a result, the loop's  $X$  would decrease as compared to the  $X$  of the loop placed in air and thus, the loop's impedance reduces. It is conventional to show impedance variations on impedance plane as demonstrated in Figure 1.2.

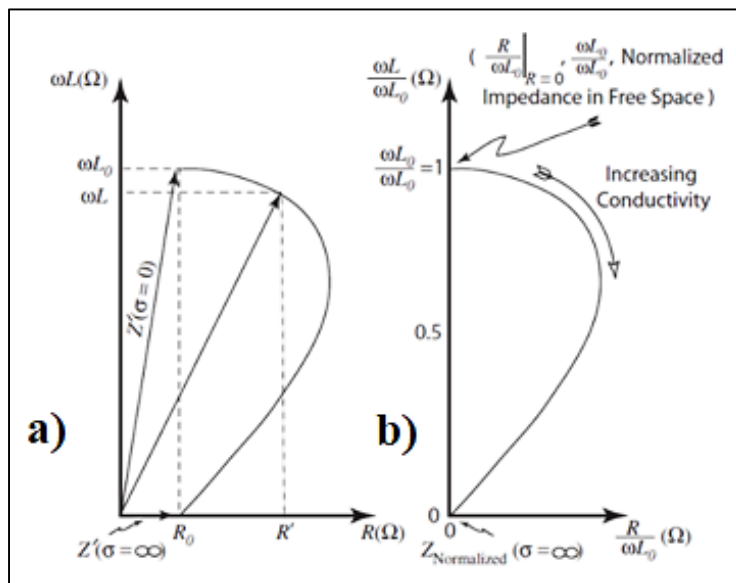


Figure 1.2 Transformation from (a) an impedance plane to (b) a normalized impedance plane (Hellier, 2013).

Referring to Equation 1.2, one can notice that the change in the test frequency changes the  $X$  value and accordingly, the impedance. Due to this fact, the scale of impedance plane requires to be scaled every time the test frequency changes. To address that, impedance plane is used in normalized form. This transformation is depicted in Figure 1.2, where the figure at left represents an impedance plane and the right one shows the normalized axes. On the new plane, the values of inductive reactance and resistance for the isolated coil are at one and zero, respectively. Normalizing the vertical and horizontal axes are carried out according to Equations 1.4 and 1.5, respectively (García-Martín et al., 2011; Hellier, 2013).

$$\text{Normalized vertical axis} = L\omega/L_0\omega \quad (1.4)$$

$$\text{Normalized horizontal axis} = \frac{R - R_0}{L_0\omega} \quad (1.5)$$

In these equations,  $L_0$  and  $R_0$  are the inductance and the resistance of the inspection when it is isolated in air, respectively. In the rest of this chapter, the impedance plane implies the normalized one.

### 1.1.2 Eddy current testing and influential parameters

EC penetration depth is limited by the test frequency as well as the permeability and the conductivity of test material. Skin depth of ECs is determined by the standard penetration depth which is a depth in the material at which the density of eddy currents reduces by 63% of the value at the surface. The standard penetration depth is commonly shown by  $\delta$ . Its relation with frequency, conductivity ( $\sigma$ ) and relative permeability is presented in Equation 1.6. The formulation is written based on, Equation 1.7, which is derived for the current density through solving Maxwell's equations for electromagnetic plane waves

$$\delta = 1/\sqrt{\pi f \sigma \mu_0 \mu_r} \quad (m) \quad (1.6)$$

$$\mathbf{J}_e = \mathbf{J}_0 e^{-\sqrt{\frac{\omega \mu_0 \mu_r \sigma}{2}} x} e^{-j \sqrt{\frac{\omega \mu_0 \mu_r \sigma}{2}} x} e^{j \omega t} \quad (1.7)$$

In Equation 1.7,  $\mathbf{J}_0$  is the current density at the material's surface. The equation shows that the EC penetration is not limited to one standard penetration depth however, as shown in Figure 1.3(a), the density of currents decreases exponentially as the currents develop deeper into the material. Furthermore, the phase of the currents flowing under the surface lags the phase of ones on surface. This phase variations are linearly related to the penetration depth according to Figure 1.3(b).

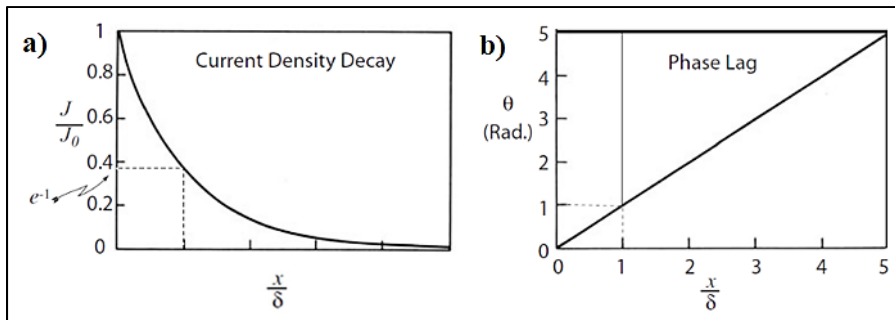


Figure 1.3 (a) Current density versus the penetration depth (Hellier, 2013), (b) changes in ECs' phase versus their depth of penetration (Hellier, 2013)

Although some parameters such as the coil configuration, size, and electromagnetic coupling between the test specimen and the coil do not affect the standard depth of penetration, but they change the absolute amplitude of eddy currents at any depth (Mix, 2005). The coupling of the coil and the test material is a function of the distance between the two. The distance is known as probe lift-off and fill factor in ECT for surface coils and encircling coils, respectively. Increasing the lift-off and decreasing the fill factor decrease the coupling and consequently, reduces the signal amplitude. Similarly, by tilting the EC coil with respect to the normal of the surface of the material the field reaching the material diminishes and as a result, the signal amplitude reduces. Aside from probe parameters, there are other parameters related to the test subject affecting the impedance of an ECT coil. In fact, any change in the characteristics of the material that affects the distribution of EC flow influences the coil's impedance. Accordingly, ECT is advantageous in detecting and characterizing anomalies that have an effect on material properties. From this category, inhomogeneities in conductivity and permeability of the material, flaws located on surface or close to surface, as well as the variations in thickness when they are smaller than the sensing depth of ECs (*i.e.*  $3\delta$ ) can be named. Each of these changes the probe's impedance in a different manner and also provides a distinct signature on impedance plane.

Depending on the application, a wide variety of eddy current instruments and probes exists. In terms of the operation mode, EC probes can be divided into two main classes based on the configuration of their pickup coils; a) the absolute, and b) differential (Shull, 2016). As

demonstrated in Figure 1.4(a) and (b), absolute probes are comprised of a single receiver coil whereas differential probes possess two receiver coils, which are wound in opposite direction and connected differentially. As shown in Figure 1.4(b), EC probes can be configured to work in reflection (driver-pickup) mode, in which a primary coil is used for excitation while the secondary absolute or differential coils are meant for sensing. This type of configuration helps to avoid the temperature drift caused by the wire resistance since the current only flows in the driver coil whereas the current in receiver coils is very small; therefore, receivers do not experience heating (Cecco, Van Drunen, & Sharp, 1983). Furthermore, it would be possible to optimize the driver and receiving coils individually to achieve an enhanced probe's flexibility and sensitivity (Burke & Ibrahim, 2004). Reflection probes have been exploited for diverse applications such as coating thickness and conductivity measurements, remote field ECT, and surface defect detection (Burke & Ibrahim, 2004).

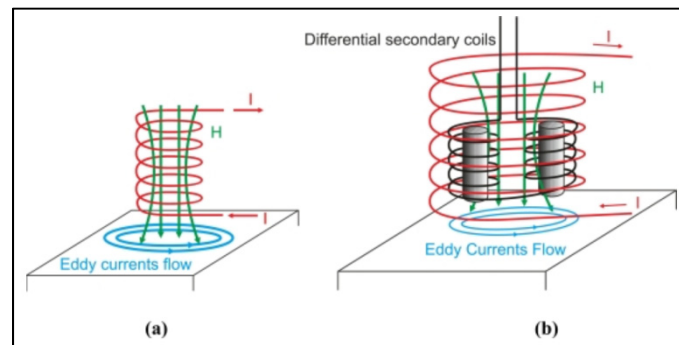


Figure 1.4 (a) Absolute and (b) reflection differential configurations of ECT probes (García-Martín et al., 2011)

Split-D reflection differential surface probe which is comprised of one driver coil and two differentially wound D-shaped receiver coils is among the most sensitive ECT probes which, in particular, are used for the purpose of surface defects detection. Each of the receiver coils in this probe is filled with a D-shaped ferrite core and a cylindrical ferrite shield contains the assembly of the coils. A 3-D half model reconstructed by the X-ray tomography of the probe is depicted in Figure 1.5(a). The probe's components are visible in a microscopic image that captures a quarter of the probe's tip in Figure 1.5(b). A more detailed presentation of the

probe's structure and geometry is provided later within chapters 2 and 3. The small footprint of the probe and its differential configuration makes it one of the most suitable choices for inspection of tiny surface breakings such as fatigue cracks.

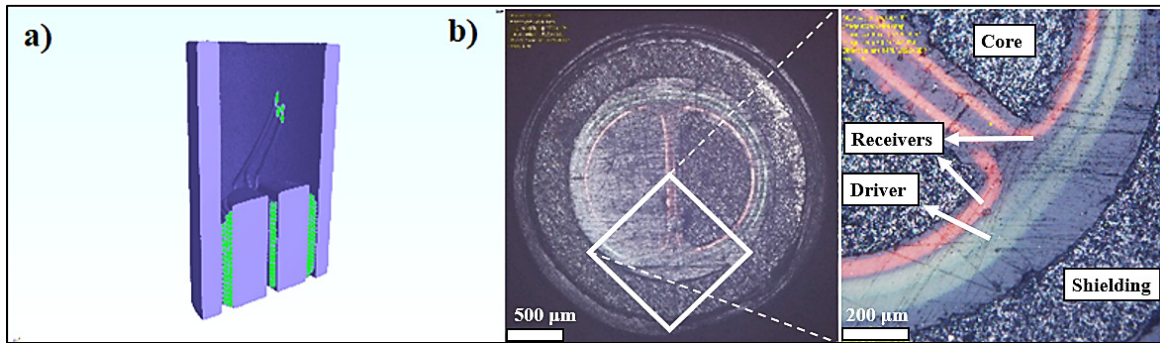


Figure 1.5 (a) 3-D model of a split-D probe reconstructed by X-ray tomography and sectioned in half, and (b) microscopic image taken from the split-D probe's tip.

### 1.1.3 Modelling in eddy current testing

In order to describe systems and to predict their response, analytical and numerical models are developed based on their governing equations. These models are called forward models, which are used to predict the measurement results by taking into account the given parameters describing the problem (Tarantola, 2005). Forward models have unique solutions for simple problem geometries and they could be expressed in entirely basic mathematical functions. This type of solution to a forward problem is called a closed-form solution. For instance, a partial differential equation (PDE) written based on the set of Maxwell's equations can be derived for an ECT problem. Depending on the complexity of the ECT problem, one might be able to find a closed-form solution to infer the ECT probe's field distribution and to evaluate the probe's impedance, accordingly. Otherwise, it is very common to estimate the solution by means of semi-analytical methods as well as purely numerical calculations. Maxwell's equations relating the material properties to electromagnetic fields in differential form are presented in Equations 1.8 to 1.11 (Shull, 2016).

$$\nabla \times \mathbf{E} = -\frac{\partial \mu \mathbf{H}}{\partial t} \text{ (Maxwell - Faraday equation)} \quad (1.8)$$

$$\nabla \times \mathbf{H} = \mathbf{J} + \frac{\partial \mathbf{D}}{\partial t} \text{ (Ampere's circuital law)} \quad (1.9)$$

$$\nabla \cdot \mathbf{D} = \rho \text{ (Gauss law for electric fields)} \quad (1.10)$$

$$\nabla \cdot \mathbf{B} = 0 \text{ (Gauss law for magnetism)} \quad (1.11)$$

where,  $\mathbf{E}$  and  $\mathbf{H}$  are electric and magnetic field intensities, respectively.  $\mathbf{D}$  and  $\mathbf{B}$  are electric and magnetic field densities, respectively. In addition,  $\rho$  is the charge density and  $\mathbf{J}$  stands for the electrical current density. In Maxwell's equations, the relation between field densities and intensities is specified by the constitutive equations presented in Equations 1.12 and 1.13, where  $\varepsilon$  symbolizes the electric permittivity of the material.

$$\mathbf{E} = \varepsilon \mathbf{D} \quad (1.12)$$

$$\mathbf{H} = \mathbf{B} / \mu \quad (1.13)$$

A closed-form solution to the PDE derived for a single cylindrical air-cored coil placed over a semi-infinite conductor clad with a conductor of a finite thickness was first suggested by *Dodd et al.* (C. Dodd & Deeds, 1968; C. V. Dodd, Luquire, Deeds, & Spoeri, 1969). Their forward model was a start to ECT modelling by providing the solution for electromagnetic vector potential ( $\mathbf{A}$ ) in the form of integrals of first-order Bessel functions. Their model made it possible to evaluate various electromagnetic quantities alongside the coil's impedance using the vector potential. The model holds for linear, isotropic and homogenous materials and axisymmetric problem geometries. Their proposed solution exceeded earlier models in many aspects; it was more comprehensive as compared to the Hochschild's model developed for an infinite coil (Hochschild, 1959), and more capable relative to the model proposed by Libby, based on transformer approach (Libby, 1971). The Dodd's model was the foundation to many consecutive inversion studies, which are performed to determine the thickness and the conductivity of metal layers (J. R. Bowler & Norton, 1992; Moulder, Uzal, & Rose, 1992; Norton, Kahn, & Mester, 1989). Several semi-analytical models have been developed since the theory of Dodd et al. for different axisymmetric problem geometries. These

configurations include the interaction between the field of air-cored/ferrite-cored ECT probes and undefective/defective conductors (Lu, Bowler, & Theodoulidis, 2012; H. Sabbagh, 1987). Noteworthy that, in the most of these studies, the problem becomes more complex as either a ferrite core is added to the coil or a defect is introduced to the material (J. R. Bowler, Theodoulidis, Xie, & Ji, 2012; Buvat et al., 2004; May, Zhou, & Morton, 2007; Theodoulidis, 2010). The solution to such problems is not unique anymore and therefore, they are mostly tackled through semi-analytical and numerical modelling, especially when the geometry is not axisymmetric. In fact, in many defect inspection applications of ECT, the geometry of the problem becomes non-axisymmetric. In such studies, ideally shaped rectangular or semi-elliptical EDM notches with finite openings are mostly used in modelling when a material contains surface and subsurface breakings (J. Bowler, Sabbagh, & Sabbagh, 1990; J. R. Bowler, 1994). In this context, many different studies have tried to use simplifying assumptions in order to suggest analytical solutions to the problem (Auld, Muennemann, & Winslow, 1981; Beissner, 1988; Burke, 1985, 1988). However, thanks to advances in computer science, the majority of ECT problems of this hand are approached by numerical methods nowadays. These methods discretize the problem's geometry into elements and they provide an approximate solution to either electromagnetic field integral equations or differential equations (Zeng, Udpa, & Udpa, 2010). As an example, Bowler *et al.* write integral equations for electromagnetic field generated by the source as an integration of Green's dyadic functions. Subsequently, these integrals are discretized over the geometry of the problem and evaluated afterwards (J. Bowler et al., 1990; J. Bowler, Yoshida, & Harfield, 1997; H. A. Sabbagh, Murphy, Sabbagh, Aldrin, & Knopp, 2013). Their approach based on integral equations is presented in form of a volume integral method (VIM) code. A review of the studies relying on this method for evaluation of split-D probes' impedance is presented in subchapter 1.1.5. Noteworthy that deriving such equations based on the Green's function could be extremely difficult for complex geometries. Therefore, anywhere within ECT studies that geometrical irregularities, as well as field and material nonlinearities are involved, numerical methods based on the solution of differential equations such as finite difference method (FDM), boundary element method (BEM), and FEM are preferred. Ferrite-cored probes, ferromagnetic materials and non-axisymmetric geometries are ECT

studies that fall in this class. FDM was the only available method during the early times of emergence of computers and its applications are limited nowadays (Auld & Moulder, 1999). BEM is frequently used in conjunction with certain analytical approximations of the problem. The other alternative is FEM, which is believed to be the most flexible in dealing with complexity and nonlinearity of the ECT problems (Chari, 1974; Ida, Palanisamy, & Lord, 1983). The following provides a brief review of the FEM-based researches studying the electromagnetic field of ECT probes.

#### **1.1.4 Finite element modelling of eddy current probes**

FEM has been successfully used for many low frequency EC applications. A long list of such publications that use the FEM to analyze and study the EC phenomenon is provided within the FEM in NDT bibliography (Mackerle, 1999, 2004). The early approaches aimed to model axisymmetric problem geometries in two dimensions (2-D). From this class, a surface coil over an aluminum slab, an encircling coil inspecting an aluminum rod with copper cladding, and a bobbin probe inspecting for crevice gap in steam generators' support plate were studied in 2-D axisymmetric (Palanisamy & Lord, 1979). Through 2-D axisymmetric modelling the geometry of a bobbin absolute coil inspecting the crevice gap was also optimized (Ida, Betzold, & Lord, 1982). The same authors also developed 2-D axisymmetric models for absolute and differential bobbin coils inspecting a tube with an outer diameter slot (Ida et al., 1983). The agreement between the models' predictions and experimentally measured signals was promising. They were also able to optimize the coil size and the spacing between the differential coils through the model.

Advances in computer science accompanied the technological growth of EC probes. Therefore, the studies are more inclined toward 3-D analysis of the probe's field interaction with defects. In this regard, two benchmark problems, defined by testing electromagnetic analysis methods (TEAM) workshop (Society) and JSAEM (Japan Society of Applied Electromagnetic and Mechanics) (Toshiyuki Takagi, Uesaka, & Miya, 1997), concerning an absolute surface coil scanning a surface rectangular notch were modelled in 3-D using the

FEM solver within COMSOL multiphysics® (Santandrea & Le Bihan, 2010). The coil model was prepared using the pre-defined multi-turn coil domain in COMSOL which considers a uniform current density across the coil cross sectional area and provides a reasonable approximation for low frequency ECT. The coil was moved along the notch length and the coil's impedance was calculated at each scanning position in order to plot impedance changes. Three layers of first order elements were defined across the first standard penetration depth to provide a better resolution for the higher density of ECs that flow close to surface. Eventually, the simulation results were compared to the findings of the benchmark studies for validation. Another paper that uses COMSOL was used by Rosell and Persson as the main FEM tool to investigate one of the problems presented by TEAM workshop (Rosell & Persson, 2011). In their 3-D model presented in Figure 1.6(a), a rectangular surface notch was scanned using a reflection differential surface probe for two different scanning directions; a) perpendicular to, and b) parallel to the notch length. The problem was truncated using a box encapsulating the assembly of the coil and sample in their study. As shown in Figure 1.6(b), the size of the box was then optimized based on the attenuation of  $A$  field. Subsequently, to calculate the probe's impedance variations as it scans the notch, several scan positions were modelled across each of the scan directions.

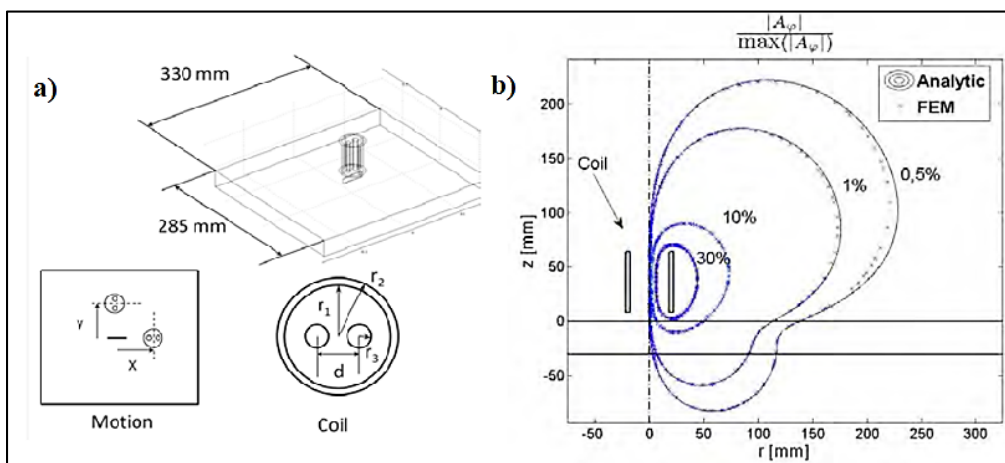


Figure 1.6 (a) 3-D assembly model for TEAM problem 8. Scan directions modelled through FEM and the structure of the reflection differential surface probe used in simulations (Rosell & Persson, 2011), and (b) four different levels of the vector potential's amplitude/maximum amplitude ratio and the truncation box defined on that basis (Rosell & Persson, 2011)

Noteworthy that to minimize the numerical errors connected to the mesh non-uniformity, the probe's impedance at each position was calculated by subtracting the probe's impedance when the notch is present from the impedance of the probe at the same position in absence of the notch. Consequently, they were able to investigate the effect of the truncation box size on the signal of their probe. They also explored the edge effect on the resulting signal using COMSOL.

The same authors prepared a model for an absolute surface coil scanning a surface rectangular notch according to TEAM problem 15 (Rosell & Persson, 2012c). They used the quasi-static approximation of Maxwell's equations to develop their FEM and validated their model by comparing it against experiments. They also tried to modify their model of EDM notch by defining different types of electrical contacts between the notch walls in order to reproduce the ECT signal of a closed surface fatigue crack having the same size as the notch. The effect of the contact types and their corresponding conductivity values was then investigated on the signal of the probe and consequently, the results are compared to measurements. The best agreement between the model and experiments was achieved as the discrete contact points was used to model conductivity bridges. The main purpose was to reproduce the signal of fatigue cracks as closely as possible using FEM to be able to use the model to conduct future model-assisted POD (MAPOD) studies.

Rosell also studied the impedance variations of a transmit-receive ECT probe as it scans over semi-elliptical closed surface cracks (Rosell, 2015). At each scan position, the probe's impedance evaluation was performed in two stages. a) an analytical evaluation when the crack is not present, and b) a numerical assessment using FEM when the crack is present. Subsequently, the impedance at each position was derived from subtraction of the impedance for two flawed and unflawed cases. The cracks were defined as surfaces with electric isolation boundary conditions in the model and so, they were assumed to be impenetrable to electric currents. The agreement between the numerical results and those of the measurements found to be acceptable.

In another study, the same strategy was used to generate ECT signal amplitude distribution for different defect sizes through FEM simulations (Rosell & Persson, 2012a). Signal response variabilities were required for a POD study. The simplified model that they used in their study for fatigue crack is shown in Figure 1.7(a), where the grey area represents the non-zero conductivity region of the crack. The contact condition, represented by  $\zeta$  was considered as one of their weighted main coefficients of amplitude variability. The other main coefficients considered in the study included crack tilt relative to the surface, probe's lift-off and crack's size.

Using the same fatigue crack concept presented in (Rosell & Persson, 2012a), ECT signals were simulated through FEM (Rosell & Persson, 2012b). In their models, the scans of an ECT probe over two types of semi-elliptical fatigue cracks with fixed length to depth ratios were simulated. In addition, the crack position relative to the scan line ( $L$ ) as well as the crack orientation relative to the scan line ( $\gamma$ ), as demonstrated in Figure 1.7(b), were considered as the parameters influencing the signal response of ECT.

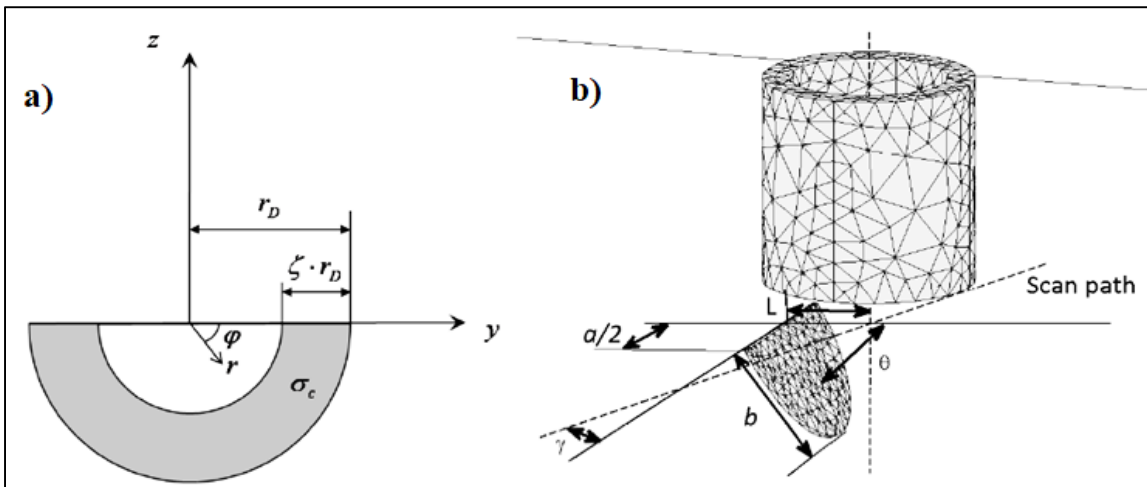


Figure 1.7 (a) Simplified closed fatigue crack model containing non-zero conductivity region proposed by (Rosell & Persson, 2012a), and (b) relevant input parameters that were accounted for in signal response POD by (Rosell & Persson, 2012b)

### 1.1.5 Model-based studies of split-D differential eddy current probe

FEM has been used in a few studies on split-D differential probes thus far. However, the popularity of the tool for ECT analysis has started to grow in industries recently (Brown & Eviston, 2017; R. D. Mooers & Aldrin, 2016a). Nakagawa *et al.* pointed out the importance of having a knowledge of the internal structure of the probe prior to modelling (N Nakagawa, Khan, & Gray, 2000). In their study, a split-D differential probe was characterized for model inputs using X-ray tomography. Afterwards, the inputs were fed into their BEM code and the model's predictions were compared to the experimental measurements for the purpose of validation. Another study by the same group investigates the effect of the notch opening and shape on the signals of split-D differential probe (Norio Nakagawa, Yang, Larson, Madison, & Raulerson, 2009). The study is interesting since EDM notches are frequently used in ECT model-based studies to represent fatigue cracks and thus, it is of high importance to gain an insight into the impact of different notch dimensional parameters on the ECT signals. This would allow one to optimize these parameters in order to achieve the best approximation for the signal of a given fatigue crack. It was demonstrated by them that the increase in notch opening results in the increase of the signal amplitude. According to their experimental data, as shown in Figure 1.8, testing a semi-circular notch with opening of 0.025 mm produces signal amplitude of 35% smaller as compared to the one obtained by testing a rectangular notch with opening of 0.127 mm. In their tests, the notch length and depth were 0.76 mm and 0.38 mm, respectively. Furthermore, it was shown that the discrepancy between the modelling and the experiment results are more significant for a notch with smaller opening. They were also able to carry out an extrapolation for their model-based study of the notch opening to deduce the signal amplitude of a notch with an opening of 0 mm. These results are presented together with their measurements in Figure 1.8.

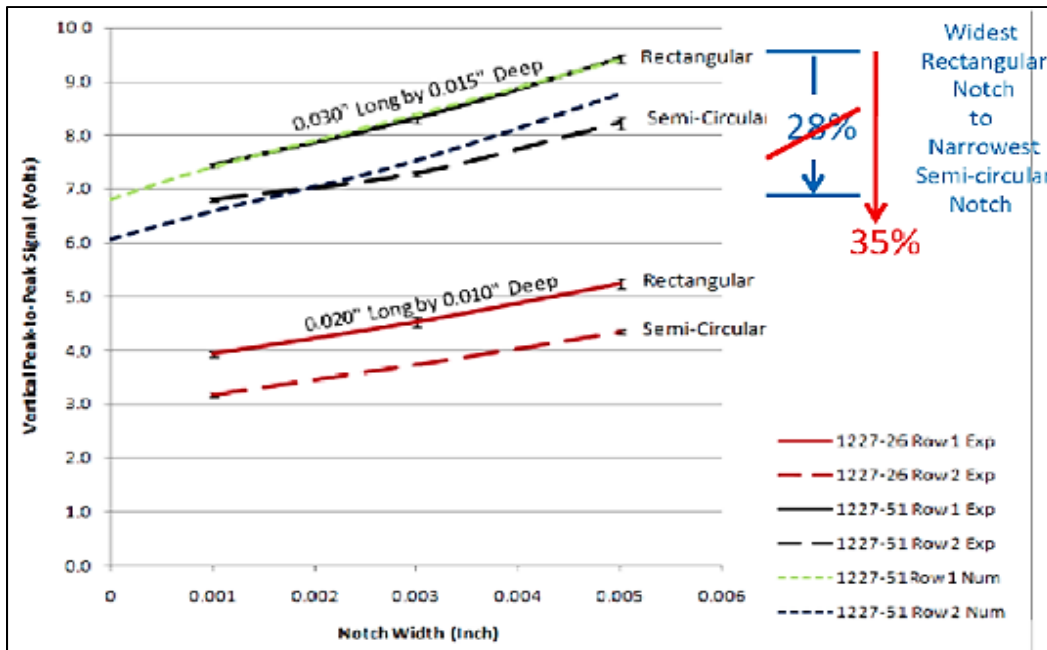


Figure 1.8 Experimental peak-to-peak voltage versus the notch opening for two types of rectangular and semi-circular notches, each having two different dimensions. Extrapolated model-based curves for the larger notches were superimposed on the experimental curves. Tests were carried out at frequency of 2 MHz on samples of Ti-6246 (Norio Nakagawa et al., 2009)

The modelling of split-D probes was majorly explored by a group of researchers that have been actively working in the field of computational electromagnetics since mid-1960s (H. A. Sabbagh et al., 2013). A series of studies devoted to split-D probes are performed using their volume integral code (VIC 3D®) to investigate the performance of such probes. The following presents a brief review of their publications.

A parametrized FEM study for two probe types of absolute and split-D differential scanning a surface notch was conducted using COMSOL (Brown & Eviston, 2017). The model geometry was prepared for the absolute probe according to the benchmark study of the Burke (TEAM problem 15) (Burke, 1988). The impedance data obtained from the simulations of the notch scan were compared to their experimental measurements, presented in their earlier publication, and the results of VIC 3D®. These results are illustrated in Figure 1.9. In the second part of this study, they looked at the impedance variations of an air-cored split-D

differential probe, with large dimensions, scanning over a rectangular notch while the scan line was aligned with the notch length. As shown in Figure 1.9, their simulation results for the probe's impedance were presented along with the measurements of impedance spectroscopy and VIC 3D®.

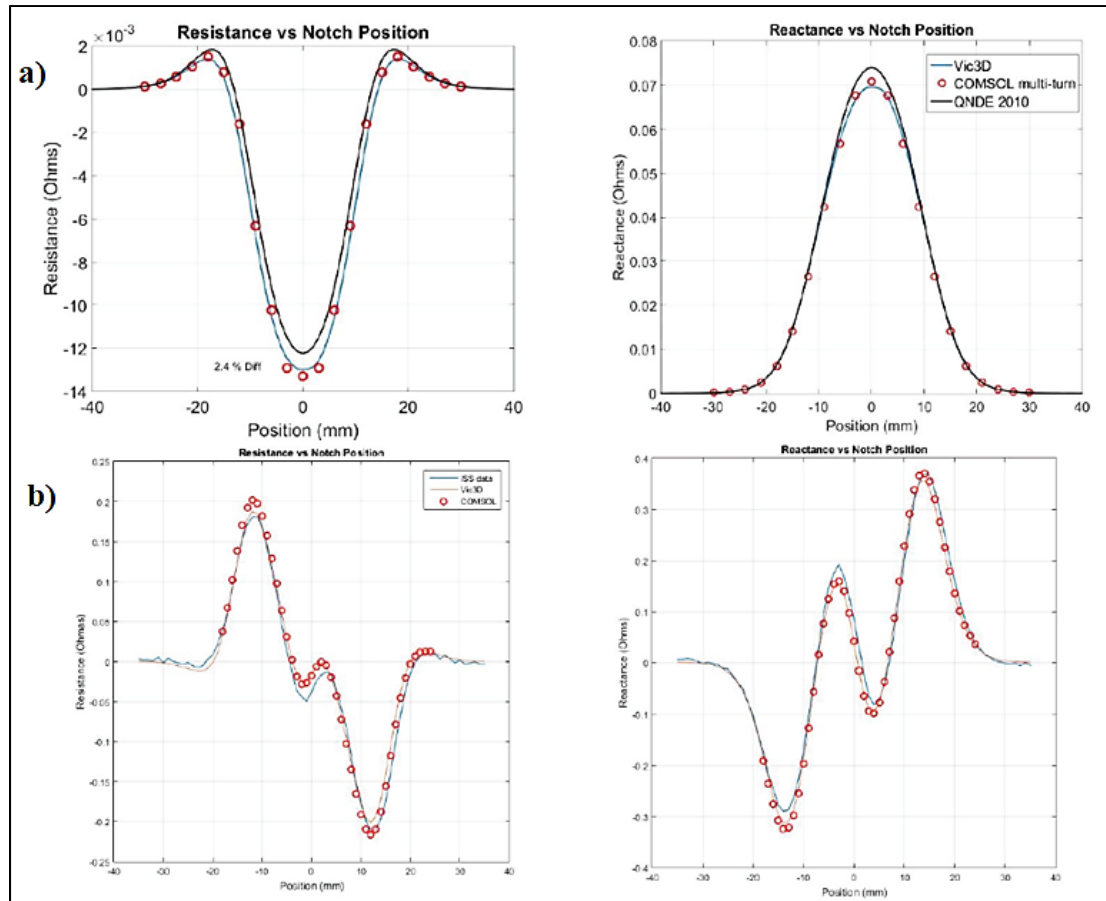


Figure 1.9 Comparison between the impedance data measured by impedance spectroscopy and those obtained from VIC 3D® and COMSOL modelling for (a) an absolute air-cored probe, (b) a split-D air-cored differential probe scanning rectangular surface notches (Brown & Eviston, 2017)

The error in estimation of the probe's impedance using COMSOL seems to be very small however; most of the commercially available split-D probes could be five times smaller than the custom probe used in this study. Furthermore, incorporating ferrite cores inside the

receiver coils and ferrite shield surrounding the coils, which is normally the case in off the shelf probes, can add to the complexity of the model and thus, the impedance evaluation.

The next study covered the fabrication and modelling of two split-D probes that were larger than the comparable commercial ones (R. D. Mooers & Aldrin, 2016a). One of the probes included ferrite cores whereas the other was air-cored. The two probes were used to scan a rectangular surface notch in a manner that the scan line fell onto the line of the notch length. Impedance variations were recorded using an impedance analyzer (IA) as well as an UniWest ECT unit. The scan was also modelled in COMSOL and VIC 3D® for the two probes. The variations in each axis of the probe's impedance are depicted in Figure 1.10(a) and 1.10(b) for air-cored and ferrite-cored probes, respectively.

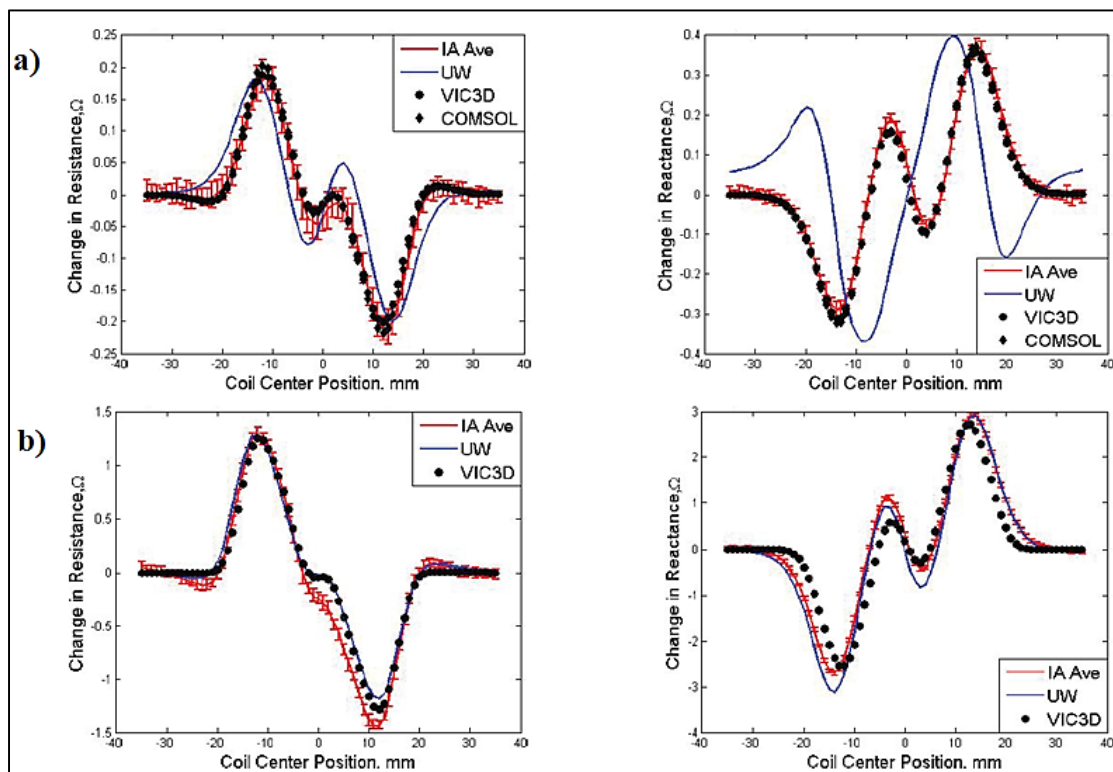


Figure 1.10 Comparison between the impedance data measured by IA, UniWest ECT unit, and those obtained from VIC 3D® and COMSOL modelling for a rectangular notch with 12.6 mm in length, 5 mm in depth, and 0.28 mm in width. The results for (a) an air-cored (R. D. Mooers & Aldrin, 2016a) and (b) a ferrite cored split-D probe (R. D. Mooers & Aldrin, 2016a)

According to their results, the simulated signal fell within the range of measurement's error at most of the scan positions in both probe cases. However, a huge discrepancy was observed between the recorded signals of UniWest and those measured by IA for the air-cored probe. As stated by authors, the source of such difference did not fully correspond to the phase rotation of the UniWest unit. They were also able to study the effect of the probe's tilt on the impedance variations, as it scanned the notch, using VIC 3D®. Accordingly, the discrepancy between the results of simulations and measurements grew, as the tilt increased.

In one of their early works, three probe types of split-D differential air-cored and ferrite-cored as well as a ferrite-cored split-D reflection differential were studied through modelling using VIC 3D® (R. Mooers, Knopp, & Blodgett, 2012). However, only the simulation results for a shielded ferrite-cored split-D differential probe scanning EDM notches in a Ti-6Al-4V plate were compared to impedance recordings. For that purpose, a Nortec 19eII ECT unit was used. The models were prepared in both VIC 3D® and ECSIM softwares. The agreement between the results obtained by simulations and measurements was not satisfactory since according to authors the measurements made by Nortec provided only relative measures of the impedance change and not the absolute values. As stated by them, results' discrepancies could be partly due to the misalignments in the scan and unbalance of the D coils. Later on, in another effort, an IA besides Nortec 2000D were used by them to verify their model which was built in VIC 3D® for a ferrite-cored split-D differential probe (R. D. Mooers, Knopp, Aldrin, & Sathish, 2014). Two notches with lengths of 2 mm and 2.5 mm, carved in a Ti-6Al-4V plate, were scanned in two directions. The first scan line was parallel to the notch length (L) and the second one was perpendicular (T). Based on their results, the shape agreement between the simulated and measured data was satisfactory for T scans, and the largest difference appeared in  $\Delta X$  values of the smaller notch sizes. In L scans, simulation data deviated from the measurements' more noticeably since the simulated results did not quite follow the experimental curve for secondary peaks that emerge between the primary ones. In most of the graphs reported there, the minimum peaks of  $\Delta R$  and  $\Delta X$  recorded by both IA and Nortec encountered an overshoot as compared to the ones obtained for

simulation. The effect was explained to be attributed to the dimensional asymmetry of the D-shaped coils.

Same group carried out a model-based study to incorporate the effect of coils' assembly tilts and shifts as well as dimensional variations of the probe's constituent element since they believed that the internal coil assembly of Split-D probes was not always perfect and thus, they commonly have tilted and shifted assemblies within the probe's housing (R. D. Mooers, Aldrin, & Knopp, 2015b). In addition, the rotation of the assembly within the housing was also studied through the model since the direction of D cores was not always as marked on the probe housing (R. D. Mooers & Aldrin, 2016b). The images of Figure 1.11(a) demonstrates the three types of parametric studies on rotation and tilt that included in their paper. The variations in impedance components, as the coil assembly was tilted by  $10^\circ$  in two opposite directions, is presented in Figure 1.11(b) for scanning a notch in L direction. They validated the study by performing experimental measurements using the probes fabricated inheriting such defects.

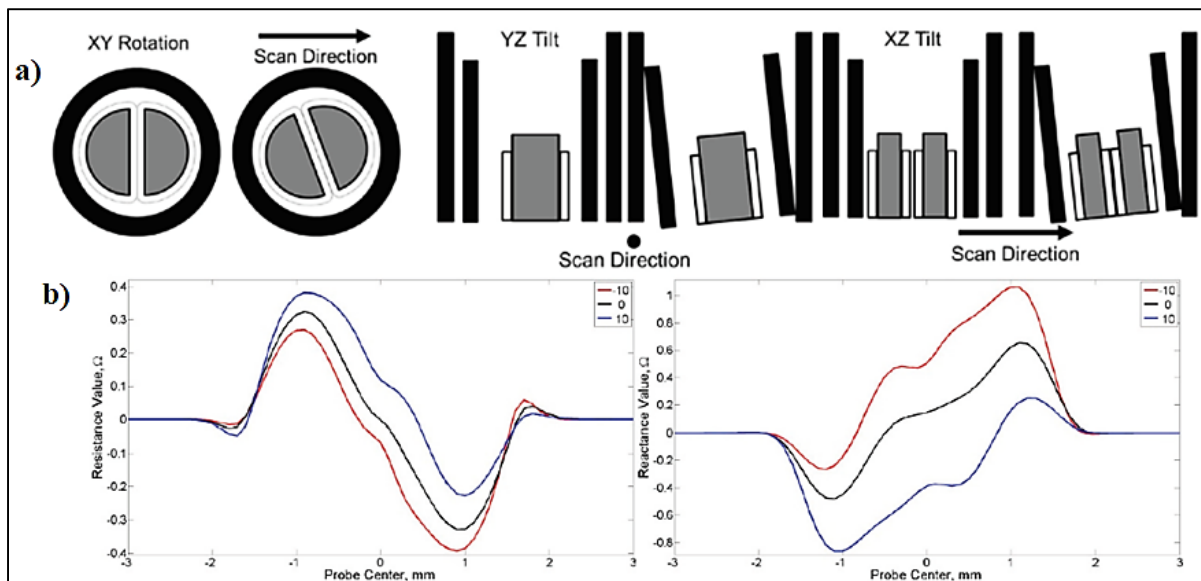


Figure 1.11 (a) D-coils' assembly rotation about Z axis and tilt in two different planes (R. D. Mooers & Aldrin, 2016b), and (b) variations of the real and imaginary parts of the probe's impedance with its D-coil assembly tilted by  $-10^\circ$  and  $10^\circ$  in XZ plane (R. D. Mooers & Aldrin, 2016b)

After some successful ECT model-based studies by this group, based on their forward solver VIC 3D®, inversion schemes were introduced for crack characterization. Although the volume integral code VIC 3D® is much faster than FEM solvers, it is not sufficiently rapid in order to incorporate it within a real-time inversion scheme for repeated calculations (J. C. Aldrin et al., 2014). Therefore, the authors presented a surrogate model based on their simulations to perform the inversion using a nonlinear least-squares estimator (NLSE). The suggested inversion approach was tested to estimate the depth, and width of through thickness, and mid-bore cracks in borehole of a 6.35 mm thick plate. The error in depth estimation was around 10% for the through thickness crack and 25% for the mid-bore. Similar to the former procedure, an interpolation table of ECT signals is prepared by carrying out simulations for notches having different sizes and simulating the scan of notches having different orientations with respect to the scan line (Shell et al., 2014). Based on the model-generated data, a surrogate forward model was defined and then, it was calibrated with reference to the collected experimental data. Accordingly, the proper transfer coefficients relating the experimental measurements to the modelling results were deduced. Furthermore, utilizing the NLSE, inversion was carried out for surface cracks. Results of the study demonstrated a good length estimation capacity whereas the depth estimation accuracy found to be lower.

In order to take into account the effect of rounding of bolt-hole edge during the inspection for potential fatigue cracks, a model-based study was conducted using COMSOL version 5.2 by (P. Underhill & Krause, 2017). Their main concern was to investigate if corner rounding has any effect on the response of a corner crack. Therefore, they generated a model for a split-D differential probe scanning corner EDMs of different openings. Their results showed that the COMSOL can be used effectively in such a study where generating a sample set representative of different rounding radiuses could have unreasonable costs. As concluded by them, rounding with a radius of 0.4 mm could reduce the signal strength of a corner notch by 20%.

In summary, except a few, the studies of the last decade on split-D probes were mainly conducted by one group who exclusively used VIC 3D® and BEM codes. The reliability of these models were well-verified through experiments. In their studies, different probe's imperfection scenarios that could be originated by displacement, tilt and rotation of the probe's internal assembly were explored. In addition, the impact of variations of notch opening on the ECT signal was discussed for specific materials. In some studies, model-based simulations were used for the scan of surface notches with different dimensions to form interpolation table of signals, based on which a surrogate model was built. Followed by that, the inversion was performed using NLSE algorithms incorporating the surrogate model. Although, the approaches used for crack characterization seemed to be promising, but their forward model was based on the simulations of a proprietary volume integral code. This dissertation also follows the objective of crack characterization however, FEM, as a more flexible and commercially available tool, is chosen to be the main analysis method for model-based studies.

## **1.2 Soft computing**

The innovative SC approaches were introduced through several works of Lotfi Zadeh *et al.* in midst of 90s. They introduced the SC as a partnership of its different principal methodologies such as FL and NN. FL was introduced as an approximating inference system that were able to emulate the human brain's perception, reasoning and decision making effectively by incorporating the imprecisions and uncertainties of the real world. For instance, the human reasoning is not binary like computers to evaluate the temperature as "yes" or "no". In contrast, these measures are expressed vaguely as "hot", "cold" and "fine". The very early successful application of these systems was in control systems, where each FL system was identified by three distinctive processing units; fuzzifier, inference system, and defuzzifier (Sugeno, 1985b). Fuzzifier is a unit at which the membership functions (MF) are used to assign a degree of a membership between 0 and 1 to a linguistic expression or value as input. According to fuzzy set theory, which is commonly used to model linguistic expressions, every input can be defined as a set to which different MFs with smooth transition boundaries

could be assigned. This is where the parameters of MFs play a very important role in mapping the inputs for further implication of the system and accordingly, in determining the system output. In next stage, operations on fuzzy sets such as intersection, union and complement can be performed depending on the design of the system. The inference system serves as reasoning core and includes the fuzzy IF-Then rules. In this unit, the rule's antecedent might be a single part or multiple, depending on the number of inputs. Therefore, the fuzzy operators might come to play in order to unify the antecedent. The defuzzification unit is the last segment of the system where the consequence of the inference system is interpreted using the MFs. The system consequents can be provided in different manners. As an instance, Takagi-Sugeno type systems calculate the crisp weighted average of consequents as the output (Tomohiro Takagi & Sugeno, 1985). A demonstration of a two-input Sugeno inference system is presented in Figure 1.12. The inputs are each having two MFs and the output is linear. The set of rules for this system are presented in Equations 1.14 to 1.17 (Jang, Sun, & Mizutani, 1997).

$$\textit{If } X \textit{ is small and } Y \textit{ is small then } z = -x + y + 1 \quad (1.14)$$

$$\textit{If } X \textit{ is small and } Y \textit{ is large then } z = -y + 3 \quad (1.15)$$

$$\textit{If } X \textit{ is large and } Y \textit{ is small then } z = -x + 3 \quad (1.16)$$

$$\textit{If } X \textit{ is large and } Y \textit{ is large then } z = x + y + 2 \quad (1.17)$$

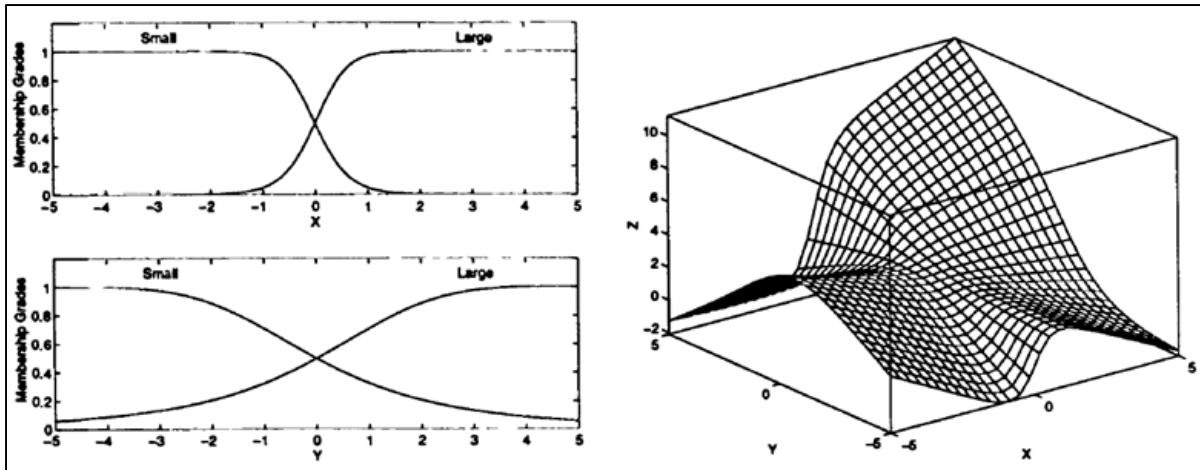


Figure 1.12 Membership functions of X and Y as the two inputs of a Sugeno system, and the surface output of the inference system (Jang et al., 1997)

In addition to FL, adaptive NN that was inspired by human brain's neurons and it has been present for a while in the field of SC as an information processing tool with perception and pattern recognition abilities. These networks are comprised of several nodes, which are interconnected by neurons or links. Depending on the direction of the links and the information flow, these networks can be feedforward or recurrent. Each node may have a set of constituent parameters which dictates the output of that node and accordingly, affects the entire behavior of the network. These modifiable parameters in the network, such as the aforementioned MF parameters, are varied repeatedly by means of optimization methods in order to converge the behavior of the network to a prescribed mapping. This is the task of optimization algorithms to set those parameters and as a result, change MFs to map a given data set of inputs to a known output. In the so called learning process for NN, a LSE in forward pass and a backpropagation algorithm in backward pass modifies the parameters in order to reproduce the desired system outputs (Jang et al., 1997). The capacity of such networks in modelling of nonlinear systems, besides the fact that FL and NN are being complementary results in forming of adaptive neuro-fuzzy systems. Adaptive neuro-fuzzy inference system (ANFIS) is one of these system types that has a very similar architecture to FL, which is complemented by adaptive learning algorithms of NN. ANFIS, owing to its high capacity to match any non-linear system, is employed in recent QNDE studies as a

universal approximator. Although the usage of these algorithms in ECT is in its infancy, but the attention paid to such approaches has been growing rapidly. The following provides an overview of previous studies concerning the application of SC in ECT.

### **1.2.1 Soft computing in eddy current testing**

Smid *et al.* used ANFIS as one of their classifier systems to predict the size and angle of surface notches based on the obtained ECT signal (Smid, Docekal, & Kreidl, 2005). Other SC techniques were also exploited for the purpose of inversion. As an instance, in a study by Kojima *et al.*, the notch profile shape was approximated using the integration of genetic algorithm and fuzzy inference system (FIS) (Kojima, Kubota, & Hashimoto, 2001). Moreover, in order to characterize the defects occurring on steam generator tubes, the result from a hybrid network consisting of a feedforward NN and a FL system was compared with the approximations made by each of NN and FL, individually. According to the reported results, error corresponding to the hybrid system was the lowest (Morabito, 1998). In the work presented by Sikora *et al.*, a fuzzy inference system was trained by measured signals of rectangular surface EDM notches in Inconel 600 plates (Sikora & Baniukiewicz, 2005). They used the data, which was collected at six different frequencies with an ECT system, to reconstruct the notch profile. Sixty percent of the signals were used for training and the rest were devoted to the system assessment. The designed system used a processing moving window, which encompassed five scanning positions at each frequency. Accordingly, a system with thirty inputs and one output was formed. Numerous system inputs made it impossible computationally to use ANFIS in their study. Therefore, they optimized the number of MFs and their related parameters through experiments and simulations in order to decrease the training load as well as the resulting number of rules. Their results for the profile reconstruction for EDM notches and some natural flaws seemed to be promising, even though the estimation error was slightly high for the flaws with irregular profile shapes. Song *et al.* were also used a hybrid intelligent system comprised of two different architectures of NN, probabilistic and back propagation (Song & Shin, 2000). These two were employed to analyze the signals of a differential bobbin probe inspecting axisymmetric I, and V shaped

grooves located on an Inconel 600 tube. One of the networks was devoted to classification while the other to sizing. The scan of two hundred grooves by means of ECT probe was simulated using FEM at two different frequencies in order to generate model-based signals for training. In next step, the model was validated by carrying out measurements. Ten signal features were used as inputs for classification and another ten was extracted for sizing by only including the features that had the most sensitivity to dimensional changes of the groove. Rosado *et al.* proposed a new method to extract the features of ECT signals (Rosado, Janeiro, Ramos, & Piedade, 2013). As reported by them, a trained NN with model-generated signals was used to deduce the length and depth of surface notches. They introduced a function, comprised of the summation of two-paired odd Gaussian functions, to reproduce the ECT signal of inspected notches. The related parameters of Gaussian functions were chosen to serve as six inputs to their network. In a study by Rao *et al.*, a NN was trained to estimate the depth in real time for both transversal and longitudinal notches located in a welded austenitic steel based on the two-frequency ECT signals (Rao, Raj, Jayakumar, & Kalyanasundaram, 2002). They extracted twelve effective parameters from the impedance trajectories. They also trained the network to neglect the edge effect and lift-off variations. Half of the number of notches in the study was used for on-line training while the other half was kept to test the system. Using their network, they could produce the depth profile excluding the noise in the signal created by the inhomogeneities of the welded area.

In the present study, a single output Sugeno type fuzzy inference system is used to estimate the notch lengths (Sugeno, 1985a). As a part of MANU-418 project, our group formerly utilized ANFIS to characterize surface fatigue cracks of AISI 410 steel samples (Xu, 2014; Xu et al., 2013). In that effort, the system was trained by means of a training data set that was obtained by robotic ECT scan of the cracked samples. To train a system using experimental dataset, depending on the maturity needed for the system training, a large set of defective samples with cracks of different characteristics might be required. This can render the process very costly in terms of money and time. Therefore, as an effective alternative to that approach, it is decided to use a training data set, which is formed based on numerical simulations for the ECT of surface notches possessing different lengths. The concept of the

model-based training is implemented here to estimate the length of semi-elliptical surface notches in 7075-T6 aluminum alloy samples. Three different features of the simulated signals of the notches are taken as training inputs to ANFIS while the notch length stands as the single system's output. A hybrid learning algorithm comprised of backpropagation error and least-squares estimator (LSE) is implemented to set the network parameters in a manner to model the system as close as possible to the desired one (Jang et al., 1997). Considering the fact that the approach is in its early stages of development, the results of the system are found to be quite acceptable. A more detailed discussion on the procedure and the length estimation results of the system is subsumed in chapter 3.

### **1.3 Probability of detection**

QNDE techniques have grown in maturity owing to advances in the technology and the development of new life estimation programs based on the DT concept. Nowadays, the concept is being used in both stages of design and maintenance by different industries in order to ensure the integrity of components and systems during their service life. As an input to these models, defect size plays a very important role. In these concepts, it is mainly assumed that there are potentially many severe flaws within the structure that can grow beyond the critical allowable flaw size before the next inspection. Therefore, such defects, which can seriously endanger the performance of the structure, shall be detected and repaired at the beginning of each usage interval. The detection and sizing of these potential defects majorly dependent on the capability of the NDE system in use and therefore, this can directly dictate the frequency of scheduled inspections planned through the risk assessment models (Berens, 2000; Lemire, Underhill, Krause, Bunn, & Butcher, 2010). In other words, being able to use a NDE system that can reliably detect smaller defects decreases the frequency of periodical inspections indicated through risk assessment analysis. Thus, to choose NDE system wisely, it is essential to have a strategy to evaluate the performance and quantify the capability of different NDE systems in detecting and sizing of such defects. The concept was originally employed by National Astronautics and Space Administration (NASA) in early 70's suggesting that the reliability of a NDE system should be evaluated relying on the

largest defect that could be missed by a NDE system instead of the smallest defect which is detected (Neuschaefer & Beal, 1972). According to studies, the gap between these two sizes could be quite large for different NDE systems (Rummel & Matzkanin, 1997). Given this fact, NASA started a new program to quantify the reliability of inspections and consider them in their designs of the new shuttle based on linear elastic fracture mechanics. Not long after that, the approach was accepted as a standard in other industries. This concept, which is used routinely for assurance of the NDE system performance, can be explained more clearly providing instances. As an example, inspectors who inspect a defect with known dimensions, without having a prior knowledge of the presence of the defect, may face different detection qualities. Apart from the expertise of inspectors, the inspection outcome can vary if one inspector carries out the tests at different times of the day. Besides, the inspection reliability can also be affected by many other parameters such as material properties and geometry as well as environmental factors, test apparatus, and test procedures of the NDE system. In order to assess the reliability of an inspection considering its conditions and procedures, POD was developed as a quantification tool based on statistical models. The responses of a few NDE systems are presented in the form of detection/no-detection data whereas most of the systems provide signal amplitude as a function of flaw size. Depending on the type of inspection data in hand, the data is conventionally analyzed through two different types of POD curves namely, Hit-Miss and  $\hat{a}$  vs.  $a$ . Where  $\hat{a}$  stands for the signal amplitude corresponding to a defect of size  $a$ . POD curves of  $\hat{a}$  vs.  $a$  data are plotted based on the variabilities in the response of an NDE method inspecting fix-sized defects. The response distribution is mainly originated from the variation of different parameters that are involved in the NDE system. These parameters do not equally affect the response, and they may not all be controllable during the inspection. Except the uncontrollable ones, whose effect would be already included in a POD study, it is wise to indicate the controllable parameters that have a stronger influence on signal. This makes it possible to design a limited number of experiments so the POD best reflects the capability of NDE while the effect of influential parameters is included. This strategy helps to reduce the costs associated with the fabrication of flawed/unflawed test coupons and the number of inspector involved. POD curves found several practical applications in industries such as measuring the improvements of NDE

systems, comparing the performance of different NDE systems in detection and sizing, and evaluating the qualification of inspectors.

For starting a NDE reliability assessment, a calibration procedure shall be determined in advance to define a reference for different inspectors. Following the calibration, every factor regarding the defect, material, testing device and environment that has an impact on signal should be included during the POD demonstration in order to obtain a POD which represents the actual test conditions. Noteworthy that the number of defective specimens should be adequate in order to perform statistical analysis on data. Moreover, the size distribution of the flaws used in the demonstration is very dependent on the selected NDT method and procedure. Hence, a prior knowledge of the method capability might be helpful in determining the size interval that contains the highest concentration of flawed samples. After plotting  $\hat{a}$  vs.  $a$  data, it is possible to left and right censor the data. To this end, the responses smaller than the level of the background noise ( $\hat{a}_{th}$ ) can be left censored, Also the responses larger than an amplitude threshold level ( $\hat{a}_{sat}$ ), indicating the saturation level, should be right censored. These values are shown in Figure 1.13(a) by dashed grey lines at the bottom of figure for background noise level, and at the top for  $\hat{a}_{sat}$ . The other important parameters that comes to play in creation of POD curves is known as  $\hat{a}_{dec}$ , which is determined according to the noise distribution and hence, the desired POFI value. It should be noted that selecting low  $\hat{a}_{dec}$  levels, with a value very close to the noise level, leads to higher POFI and lower POD. As the data is censored, it is possible to derive a linear relationship between the  $\hat{a}$  and  $a$ , where the regression parameters are estimated through maximum likelihood by considering a constant signal response variance at all crack sizes. To use this method,  $\hat{a}$  data is assumed to be distributed normally about the regression trend, as depicted in Figure 1.13(a). Sometimes, this linear relation can be best established for the data if  $\hat{a}$  or  $a$ , or both are presented in logarithmical scales. Since the regression parameters are estimated values, there is a variance connected to the regression. The can be calculated for the confidence level of 95%, which in turn yields the bounds for regression variance at each size. Figure 1.13(a) shows the regression line by a solid line, and the 95% confidence boundaries with dashed ones.

Confidence boundaries are further away from the regression line at its extremities since the confidence at the center of regression is the highest and it drops as it reaches the extremities. This is mainly observed due to the uncertainties of the regression line slope. According to experience,  $\hat{a}$  vs.  $a$  POD has a form of cumulative normal or cumulative log normal (Annis, 2009). In Figure 1.13(b), POD curve and its 95% limits are plotted according to data presented in Figure 1.13(a).

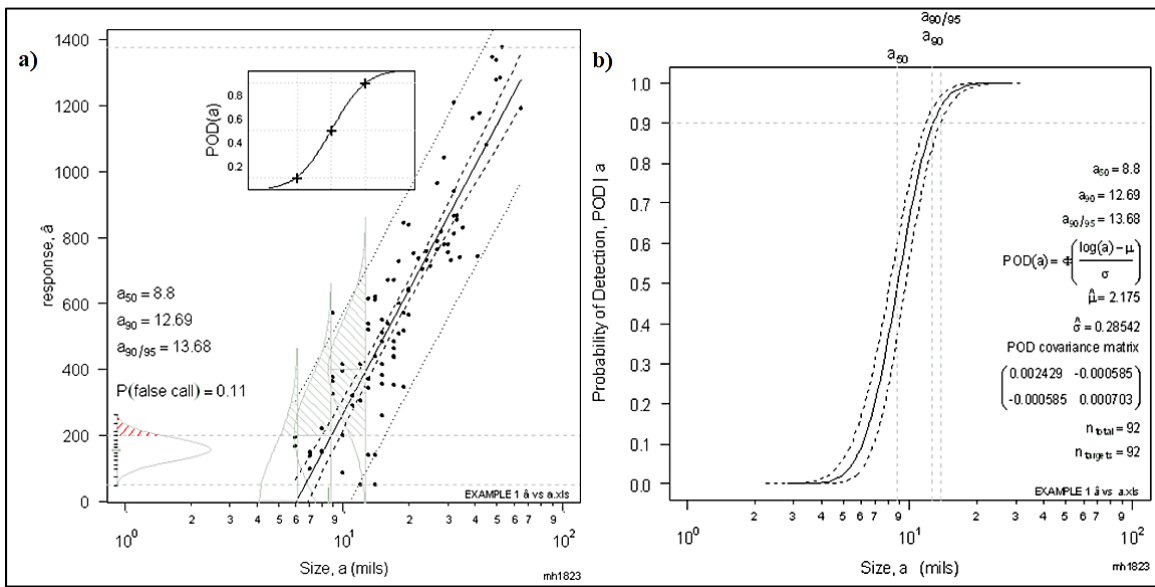


Figure 1.13 (a) Regression line along with the upper and lower confidence bonds for  $\hat{a}$  vs.  $\log(a)$  data (Annis, 2009), and (b) POD curve and 95% confidence bonds (Annis, 2009)

The defect size standing for  $a_{90/95}$  is conventionally taken as the size that can be reliably detected in POD studies. However, this can be different considering the application sensitivity and the desired reliability criteria.  $a_{90/95}$  states that there is 95% of confidence to detect a defect with size  $a$  or larger, 90% of the inspection times (Berens, 2000). The following section is devoted to a review of previous reliability studies conducted in the field of ECT.

### 1.3.1 Probability of detection for eddy current testing

A comprehensive reliability study regarding the EC inspection of bolt hole cracks was presented in several publications by (Lemire, Underhill, & Krause, 2009; Lemire et al., 2010; P. Underhill & T. Krause, 2011a, 2011b; P. R. Underhill & T. W. Krause, 2011; P. R. Underhill & Krause, 2016). These studies are particularly interesting since reflection differential bolt hole scanner ECT probes were used for inspections. In the initial study, numerous flawed/unflawed two-layered aluminum coupons were produced representing the bolt hole of layered aluminum structures of aircraft wing regions (Lemire et al., 2009; Lemire et al., 2010). Mid-bore flaws were introduced to the holes and several inspectors conducted the inspections using a calibration procedure. The bolt hole flaws were partially fatigue induced cracks developed from initial notches while the rest of them were EDM notches. They observed that the signal response plotted versus the depth for EDM notches has a different trend from the results of fatigue cracks. The difference between the aspect ratios of cracks and notches as well as the limited sensitivity of ECT to the notch depth at the selected frequency of 400 KHz were the main reasons mentioned in the study. Accordingly, they found that plotting the signal response data versus the length of EDM/cracks provides a better matching of the trend. Moreover, after plotting the response data versus the defect length for each inspector, the results revealed that the initial notch size used in calibrations was too small and hence, it caused too much variability in the recorded signal amplitudes. Therefore, they suggested to normalized data with the response of a larger notch and the mean of two larger notches to address the issue. The improvements gained by this method in the POD curves of EDMs and cracks are demonstrated in Figure 1.14(a) and Figure 1.14 (b). Noteworthy that the curve of the crack is wider since there was a larger spread in the data of fatigue cracks. Their second approach to reliability of ECT for inspecting boreholes involved the creation of fatigue cracks in hole without having starter notches (P. Underhill & T. Krause, 2011a). They applied cyclic loads to samples in order to grow cracks from the machined surfaces of the holes. Several inspections were carried out using ECT split-D hole scanner during the loading. Afterwards, the crack size related to each ECT scan was indicated by investigating the striation patterns of fatigue through fractography. Some of the

induced cracks were corner cracks while the rest were mid-bores. The authors presented a comparison study, using C-scan data, for the detectability of corner and mid-bore cracks at two different frequencies based on the hit-miss data.

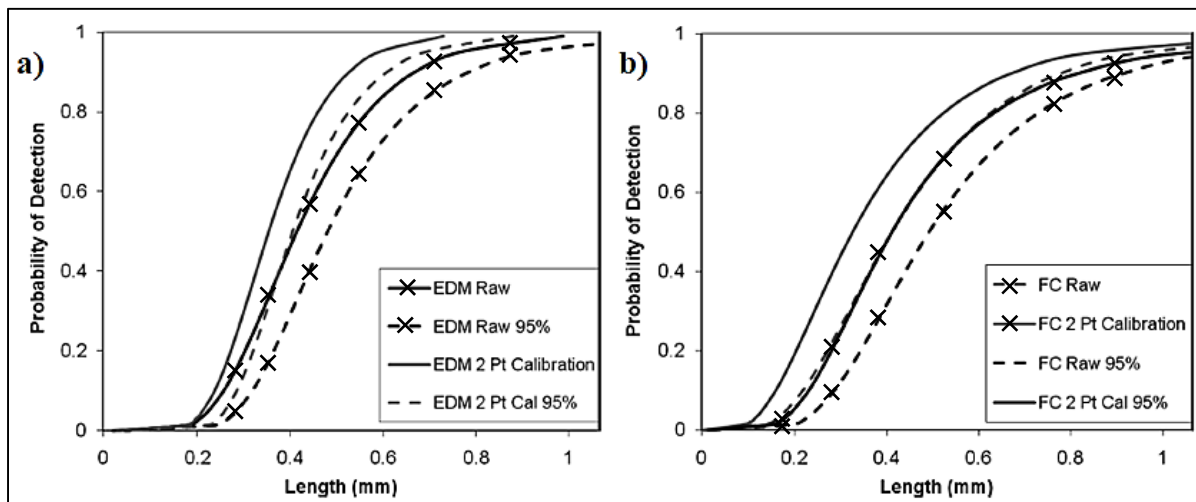


Figure 1.14 Two-point normalization applied to raw data and the resulting POD curve is compared to the POD curve plotted for raw data for (a) EDM (Lemire et al., 2010), and (b) fatigue cracks (Lemire et al., 2010)

As implied by Figure 1.15, higher test frequency increases the signal height, which is the main feature contributing to the detectability of C-scan images, and hence, enhances the POD. Furthermore, as the probe gets closer to the edge of the hole, adjacent to the sample's surface, the current is compressed due to edge effect. Consequently, the higher current concentration at the edge gives rise to higher signal amplitudes and a better POD for corner cracks as compared to mid-bore ones.

a)	Parameter	Corner 800 kHz	Mid-bore 800 kHz	Corner 1600 kHz	Mid-bore 1600 kHz
	# of samples	30	44	30	44
	Depth $a_{90/95}$ (mm)	0.45	0.50	0.22	0.34
	Length $a_{90/95}$ (mm)	0.45	1.26	0.22	0.62
	Depth $a_{50}$ (mm)	0.26	0.22	0.15	0.15
	Length $a_{50}$ (mm)	0.26	0.47	0.15	0.35
	Area at $a_{50}$ (mm <sup>2</sup> )	0.053	0.162	0.018	0.041

b)	Parameter	Freq. kHz	Intimate contact probe	Non-contact probe
	$a_{50}$ (mm)	1600	0.15	0.18
	$a_{90/95}$ (mm)	1600	0.22	0.29
	$a_{50}$ (mm)	800	0.26	0.31
	$a_{90/95}$ (mm)	800	0.45	–

Figure 1.15 POD parameters for (a) different test frequencies and crack locations (P. Underhill & T. Krause, 2011a), and (b) different probes and frequencies (P. R. Underhill & T. W. Krause, 2011)

The effect of different test frequencies on POD was investigated in another study (P. R. Underhill & T. W. Krause, 2011). Also, the performance of a contact split-D probe was compared to a non-contact one, which had a steel sheath. As reported by authors, the phase angle, that the signal and lift-off trace make, increased at higher frequencies leading to an enhanced detection through C-scan images. In contrast, the signal amplitude almost remained unchanged. Their results for the comparing the PODs of the two different probes used at different frequencies are presented in Figure 1.15(b). Only the data gathered at the two highest frequencies were statistically adequate to form POD curves. The best POD was obtained for the intimate contact probe working at highest frequency of 1600 kHz.

The hit-miss data, gathered from the visual inspection of C-scans of mid-bore cracks, was used for POD analysis in a similar study by (P. Underhill & T. Krause, 2011b). Cracks were grown under cyclic loading from the surface of machined bolt holes without the aid of starter notches. Additionally, the C-scan images were recorded for the automated ECT which was performed at different loading cycles. Then, the crack sizes corresponding to the cycles, at which the images were taken, were determined using quantitative fractography. In this manner, the hit-miss data versus crack length and depth were plotted and also the POD curve was extracted for each of them. Their results demonstrated that  $a_{50}$  for length was twice the

value of  $a_{50}$  found for depth. The observation reflected the actual length/depth aspect ratio of the fatigue cracks. The reasons provided for supporting the observation were that the crack depth was smaller than  $3\delta$  and also the crack length did not exceed the effective diameter of the probe.

The same group used the real fastener holes of a stabilizer component, instead of using machined holes, to grow fatigue cracks in a recent publication (P. R. Underhill & T. W. Krause, 2016). Similar to their former studies, quantitative fractography was used to associate the crack sizes to the repeated automated ECT inspections. As illustrated in Figure 1.16, hit-miss POD parameters showed that for mid-bore cracks, grown from the actual in-service bolt holes, had a  $a_{90/95}$  smaller than  $a_{90/95}$  for corner cracks. These results were against the results reported for the POD of cracks grown from the machined bolt holes. Presence of burrs at the corners as well as the possible rounding of the corners was found to be the main reasons explaining this contrast in results. It sounds convincing since due to the first reason the signal/noise ratio was reduced and the signal was weakened by introducing lift-off as second reason.

Parameter	Cracks in drilled holes		Cracks in bolt holes extracted from service	
	Corner	Mid-Bore	Corner	Mid-Bore
Number of samples	30	44	58	62
Length $a_{90/95}$ (mm)	0.29	0.63	0.82	0.60
Length $a_{50}$ (mm)	0.15	0.33	0.32	0.30

Figure 1.16 POD parameters are compared for mid-bore and corner cracks grown in drilled holes as well as the actual bolt holes of in-service components (P. R. Underhill & T. W. Krause, 2016)

Rosell *et al.* used their validated model of an absolute probe and a parametric fatigue crack in order to develop a MAPOD (Rosell & Persson, 2012c, 2013). The influential parameters contributing to the signal response variability in their experiments included the crack

characteristics, the probe's lift-off, the probe's position relative to the crack line, and the crack orientation relative to the scan line. They prepared a meta-model based on FEM simulations of cracks to produce signal response distribution for each crack size. Rossell also carried out another model assisted POD using the simulations of FEM for a transmit-receive ECT probe scanning surface cracks (Rosell, 2015). In the model, he considered a broad set of variable parameters affecting the signal response such as probe's position and scan orientation relative to the crack, lift-off, crack's tilt, and the conductivity of material. The signal response was assumed to be a linear function of these parameters varying around a mean  $\hat{a}$  value for each crack size. Accordingly, a meta-model, which required a reduced number of simulations, was established. Once the model was built, parameters were changed and the signal responses were plotted versus crack length and consequently, the MAPOD was plotted.

The study presented in chapter 4 investigates the combined effect of surface roughness and test frequency on the noise level for ECT of surface fatigue cracks in martensitic stainless steel samples of AISI 410, since both of these parameters are of high importance in choosing the appropriate NDE procedure for ferromagnetic materials. The chapter also incorporates a simplified reliability study by means of POD curves comparing the capability of manual and automated surface scans performed by a slit-D surface probe. Only the influential parameters, which are selected based on the prior experience of using such probes, are included to contribute to the signal response variability in order to generate PODs that reflect the actual test conditions in the best manner. The effect of crack orientation relative to the scan line, as an influential parameter on ECT amplitude, is further investigated through FEM simulations.



## CHAPTER 2

### FINITE ELEMENT BASED MODELLING OF SURFACE CRACKS SCANNING USING A REFLECTION DIFFERENTIAL SPLIT-D EDDY CURRENT PROBE

Ehsan Mohseni<sup>a</sup>, Demartonne Ramos França<sup>b</sup>, Martin Viens<sup>a</sup>, Wen Fang Xie<sup>c</sup>, and Baoguang Xu<sup>c</sup>

<sup>a</sup> Department of Mechanical Engineering, École de technologie supérieure (ÉTS), Montréal (Québec), H3C 1K3, Canada

<sup>b</sup> John Abbott College, Montréal (Québec), H9X 3L9 Canada

<sup>c</sup> Department of Mechanical & Industrial Engineering, Concordia University, Montréal (Québec), H3G 1M8 Canada

Paper submitted to the Journal of Nondestructive Evaluation, June 2018

#### Abstract

Differential eddy current probes are commonly used to detect tiny cracks on the surface of conductive materials. Since the development of analytical or semi-analytical models of such a sensor may be prone to intractable complications, there is, nowadays, a growing number of research works on the numerical modelling of these sensors. In this paper, by the use of finite elements modelling (FEM), the interaction of a reflection differential split-D probe with surface electrical discharge machined (EDM) notches has been simulated in 3 dimensional (3-D) half space. In order to attain a better insight into the correct setup of the FEM parameters, a simple multi-turn cylindrical absolute coil has also been modelled. The outcome generated through the simulated scan of this absolute coil over a surface notch in aluminum is validated with existing experimental impedance data taken from the literature. Parameters contributing to reliable FEM simulation results, such as maximum mesh size, mesh distribution, extent of the surrounding air domain and conductivity of the air are all investigated for the 3-D modelling of both absolute and differential probes. The investigation shows that the simulation results on a commercial reflection differential split-D surface pencil probe closely estimate the experimental measurements of the probe's impedance variations as it scans three EDM notches having different depths in aluminum. The reliability

of the simulation results generated by Comsol Multiphysics version 5 FEM package (COMSOL, 2018) are discussed for the cases of absolute and differential probes.

## 2.1 Introduction

The presence of microscopic imperfections within the structure of materials is inevitable in production parts. Under specific loading and environmental conditions, these imperfections may grow and form critical discontinuities. For instance, the fatigue crack is a very common defect type that could be frequently found in components under cyclic loads. These defects may deleteriously affect the performance of components and industrial systems by reducing their expected lifetime. The presence of such cracks and other kinds of discontinuity justifies the necessity of in service non-destructive testing (NDT) of components and systems, especially when the associated systems are directly related to human safety. Among all other industries who employ NDT to assess the integrity of structures (Bhaumik, Sujata, & Venkataswamy, 2008; Jones, Molent, & Pitt, 1999; Pitt & Jones, 1997), the aerospace industry is tightly connected to human safety. A wide variety of fatigue induced flaw types may exist in the components of an aircraft (Findlay & Harrison, 2002; Grover, 1966). Therefore, depending on the nature and location of these flaws, proper NDT techniques should be assigned for in-service inspections. Eddy current testing (ECT) has been routinely employed in various industries as a well-established NDT technique applied to conductive materials. Recent progresses in ECT is readily found in thickness measurement of coatings or thin conductive sheet metals, evaluation of conductivity and permeability variations, detection of surface and near surface inhomogeneities such as cracks (Davis, 1989; Hellier, 2013; Shull, 2016). This wide diversity of applications has demanded the development of different configurations of eddy current (EC) sensors tailored to specific inspection purposes (García-Martín et al., 2011). In the aerospace industry, ECT is well-known for its superior inspection performance of bolt holes, lap joints, wheels and engine components (Hagemaier & Kark, 1997; Krause, Hohmann, Gruneklee, & Maus, 2000; Wincheski & Namkung, 1998).

Absolute surface probes, with their simplest configuration (a single multi-turn circular coil), are conceived to operate typically at a frequency range of 100 Hz to 4 MHz. Depending on the type of application, they may have different shapes and sizes. Since lower operating frequencies imply higher penetration depths inside the material, low frequency absolute surface probes (no more than 500 kHz) with relatively large footprint diameters are best suited for either performing thickness, permeability and conductivity evaluations or detecting near surface defects and inhomogeneities (Shull, 2016). Reflection differential and bridge differential probes have more elaborated designs and are essentially assigned for detecting and sizing tiny surface breakings. Besides being virtually insensitive to gradual variations in the material's thickness, conductivity and permeability, the reflection differential probes compensate for the unwanted effects caused by the probe's tilt or lift-off, owing to the differential configuration of their receiver coils. Surface differential probes are commonly used in the form of an optimized reflection differential split-D configuration, which has a relatively small footprint considering the shape of its receiver coils.

For more than 50 years, numerous researchers have been trying to expand the borders of EC theory aiming at finding the solutions to the set of Maxwell's equations for the interaction between different probe types and defective/un-defective materials. Only a few succeeded to deploy analytical/semi-analytical approaches for some specific cases, which were accompanied by simplifying assumptions limiting their applications for actual cases (Burrows, 1964; C. Dodd & Deeds, 1968). Others mainly utilized more flexible numerical methods to diminish the modelling complexity for the EC coupling with defects, making it possible to estimate probe impedance variations over defective samples (J. Bowler & Harfield, 1998; J. Bowler, Jenkins, Sabbagh, & Sabbagh, 1991; J. R. Bowler, 1994). These modelling approaches included a broad diversity of numerical techniques emerging as efficient tools for EC analysis. All classical discretization approaches, such as finite element method (FEM), finite volume method (FVM) and finite difference method (FDM) have been considered as powerful numerical techniques for approximating the solution of differential equations with relative advantages and disadvantages depending on the application and the governing partial differential equations (Peiró & Sherwin, 2005). Given the same computing

power, FEM may not be the best in terms of solving speed, but several well-established commercial FEM software packages are conceived for a wide variety of problem classes with appropriate governing equations and solvers. This feature makes FEM packages the most flexible and accessible tools for performing numerical analysis. In the present paper, Comsol is extensively used for FEM of the interaction between eddy currents and geometrical discontinuities in conductors.

Considering all aforementioned advantages associated with the surface differential probes, a growing number of researchers focused on the modelling of this type of configuration. Most of the current works are devoted to numerical modelling and parametric studies of split-D differential probes, since the experimental tests may be time consuming and costly (Khan & Nakagawa, 1999; R. Mooers et al., 2012; R. D. Mooers, Knopp, Aldrin, & Sathish, 2013; R. D. Mooers et al., 2014; N Nakagawa et al., 2000; Norio Nakagawa et al., 2009; Rosell & Persson, 2011; H. A. Sabbagh, Sabbagh, & Murphy, 2002). For instance, in the work developed by R. D. Mooers et al (R. Mooers et al., 2012; R. D. Mooers et al., 2014), the results obtained from two numerical software packages, namely VIC-3D and ECSIM, are compared with experimental measurements performed by a split-D probe. In another related study (R. D. Mooers et al., 2013) a parametric sweep on the dimensions of each constituting component of a split-D probe is carried out with the two aforementioned software packages, and the influence of each parameter on the recorded signals is determined as the probe scans a notch. A model developed by N. Nakagawa et al (Norio Nakagawa et al., 2009) for a split-D probe describes the effect of electrical discharge machined (EDM) notch width on the probe's output signal, and simulation results are then validated with experimental data. The primary objective of each EC model is to reproduce the results of experiments to the highest possible accuracy. Then, the premium EC modeling results could form the essentials of defect characterization (inversion), and reliability studies (J. Aldrin, Knopp, Lindgren, & Jata, 2009; J. C. Aldrin et al., 2012; Knopp, Aldrin, Lindgren, & Annis, 2006; Shell et al., 2014). Therefore, to assess the rigorousness of each EC model, a proper validation study must be carried out (Khan & Nakagawa, 1999; Knopp, Aldrin, & Misra, 2006; N Nakagawa et al., 2000). Rosell and Persson (Rosell & Persson, 2011) reproduced the results of a

numerical benchmark study called TEAM problem 8, which was established by TEAM workshop (Verite, 1990). In this study, a differential probe, comprised of a drive and two circular receiver coils, is modelled using Comsol Multiphysics. Within the benchmark study provided by TEAM, the probe's dimensions are significantly larger than those of commercially available split-D probes, and the frequency investigated is much lower than the typical operating frequency for these types of probe. Certainly, all those ideal considerations are key for providing a basis for validating a wide range of modelling efforts. However, they are not sufficiently robust for validating the models for small cracks characterization.

The present study aims at surface crack characterization using a split-D probe. Therefore, simulated signals obtained with realistic split-D probe configurations will be used for both probability of detection studies [Mohseni E., Habibzadeh Boukani H., Ramos França D., Viens M. (2018) Reliability study of manual and automated eddy current testing of AISI 410 martensitic stainless steel. Submitted to Journal of Nondestructive Evaluation] and training data set for a fuzzy logic based inversion algorithm (Xu et al., 2013). For these very purposes, the reliability of Comsol on predicting the split-D probe's output signals as it scans surface EDM notches are here investigated systematically.

The current paper is organized as follows. In Section 2.2, the experimental setup used to validate numerical model is described. It comprises a commercially available split-D differential probe scanning three notches with different depths in an aluminum calibration block. In Section 2.3, an absolute probe is first modelled in Comsol version 5 in order to gain a better understanding on the simulation parameter setup. Results are compared with reference values found in the literature (Burke, 1988). In Section 2.4, the commercial split-D probe is modelled in Comsol. Numerical simulations are carried out for all three reference notches in the aluminum calibration block and compared against measurement data. Finally, the summary and conclusions are given in Section 2.5.

## 2.2 Impedance measurement of a commercial split-D coil

In order to verify the reliability of Comsol Multiphysics in simulating the output response of a commercial split-D probe, a Nortec-500 flaw detector from Olympus NDT corporation along with a reflection differential split-D surface pencil probe are selected for the measurement of its impedance as it scans three distinct EDM reference notches engraved in an aluminum calibration block. The probe's bandwidth extends from 500 kHz to 3 MHz. Figure 2.1(a) and Figure 2.1(b) give the details on the probe's tip, showing the driver coil, receiver coils inside the driver, surrounding ferrite shielding and D-shaped ferrite cores. Because the probe's configuration and geometry are proprietary, only a little design information is readily available from the manufacturer's website. For this reason, the probe's dimensions were either measured from microscopic images or extracted after destroying a probe to reveal its inner structure. Table 2.1 summarizes all relevant information on dimensions and material properties of the probe's constituents.

Table 2.1 Dimensions and material properties of the commercial split-D probe's components.

<b>Receiver D-coils:</b>	20 loops of 0.063 mm dia. wire	<b>Shielding inner diameter:</b>	1.934 mm
<b>Driver coil:</b>	37 loops of 0.055 mm dia. wire in 2 layers	<b>Shielding outer diameter:</b>	2.528 mm
<b>Coils height:</b>	1.260 mm	<b>Shielding height:</b>	3.000 mm
<b>Core:</b>	1.254 mm dia. × 2.000 mm height	<b>Conductivity of cores and shielding:</b>	0.2 S/m
<b>Gap between cores:</b>	0.224 mm	<b>Permeability of cores and shielding:</b>	2500 $\mu_r$

The Nortec-500 flaw detector has a built-in screen to display the probe's differential impedance. Here, however, the measurements are performed by a LabVIEW application that controls a data acquisition card connected to the output voltages of the Nortec system. The

voltage signals, respectively given by the horizontal and the vertical position of the probe impedance on the detector screen, are used to verify the accuracy of shape, phase and amplitude of the simulated signals in Comsol.

A 95 mm long  $\times$  35 mm wide  $\times$  5 mm high calibration 7075-T6 aluminum block containing three 0.18 mm-wide EDM notches with different depths (namely, 0.188 mm, 0.503 mm and 1.008 mm) is used throughout the scan measurements. The conductivity of this aluminum block is measured as 19.7 MS/m using the Nortec 500 flaw detector itself, a dedicated conductivity probe and conductivity reference blocks. Since the notches extend throughout the width of the aluminum block, their lengths correspond to 35 mm and are much longer than the probe's footprint.

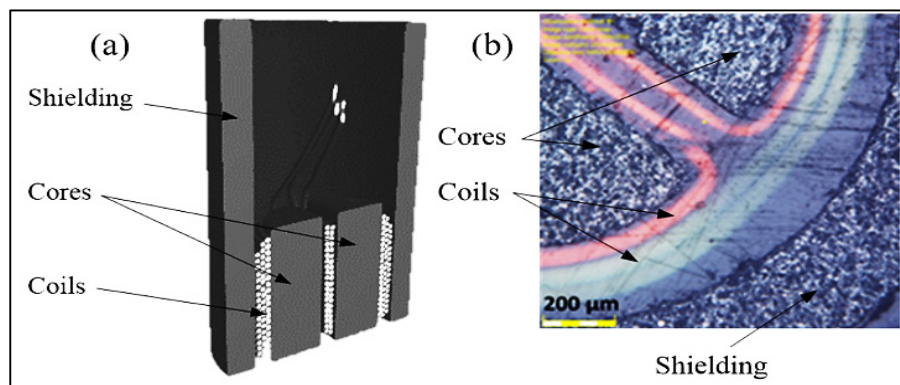


Figure 2.1 (a) 3-D model of the split-D probe showing coils, cores and magnetic shielding (b) zoom on the probe's tip taken with a confocal optical microscope. The outer driver coil and the inner receiver coils are green and red, respectively

With respect to the experimental procedure, the split-D probe is clamped inside an alignment device. The aluminum block sits on a motorized X-Y table allowing micrometric translations along each axis. Initially, the horizontal and vertical gains of the Nortec-500 flaw detector are equally adjusted, and a 6 V-driving voltage is selected. With this instrument, it is important to keep the same impedance plane rotation angle during all scans in order to be able to draw comparisons between simulation results and experimental measurements. In this case, the

angle of zero degree is selected. The probe's tip is placed on the aluminum block in a manner to have a small lift-off of 0.03 mm. Each notch is scanned five times and each time, the lift-off is recalibrated to include the error associated with the lift-off calibration in measurements. This procedure is essential since the lift-off calibration is very dependent on the accuracy of the Z-stage and thus it can vary slightly from one scan to another. Besides that, the rotation of the probe is finely adjusted in order to guarantee that the separation surface of the D-cores is parallel to the notch axis. The perpendicularity of the probe with respect to the aluminum block's surface has been verified by scanning a surface notch. Indeed, the alignment of the system was confirmed by a fairly symmetric 8-shaped signal with positive and negative peaks of almost equal magnitudes. The scanning of notches is performed by moving the center of the probe's tip from -2 to +2 mm with respect to the notch centerline. The data is recorded in steps of 50  $\mu\text{m}$  along the scanning path. Figure 2.2(a) and Figure 2.2(b) illustrate the experimental setup as well as the probe's orientation and scan direction with respect to a single notch.

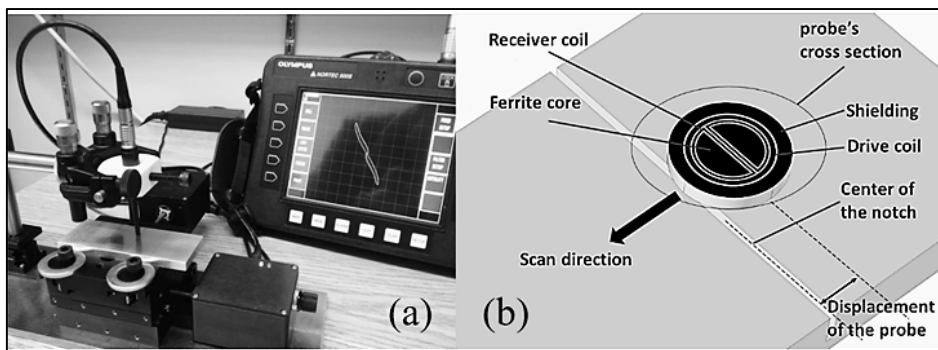


Figure 2.2 (a) Experimental setup for measuring the split-D probe's differential impedance as the probe scans three reference notches with different depths in aluminum (b) schematic of the split-D probe's orientation and scan direction with respect to an EDM notch

### 2.3 Refinement of finite element modelling parameters using an absolute coil

In the present investigation, the authors optimize EC system modelling parameters in Comsol so as to reproduce experimental data provided in Burke's experiment (Burke, 1988). In his

work, Burke presented the impedance variation measurements of an air-cored absolute coil scanning over a rectangular notch in an aluminum plate. The detailed description of the setup, geometries and dimensions can be found in the original work (Burke, 1988).

The axisymmetric nature of an eddy current absolute coil's geometry allows one to build a two dimensional (2D)-axisymmetric model when the coil is either in air or located over an un-defective conductor. However, by introducing a notch onto the conductor's surface, the geometry is no longer axisymmetric. Consequently, Burke's experimental arrangement needs to be modelled in 3-D. Nonetheless, because the coil is always centered on the notch axis, the problem is symmetric with respect to a plane perpendicular to the conductor's surface and passing through the notch's centerline. The full scale geometry of the Burke's setup model could thus be cut in half using this plane of symmetry. The overall half scale model created in Comsol is illustrated in Figure 2.3.

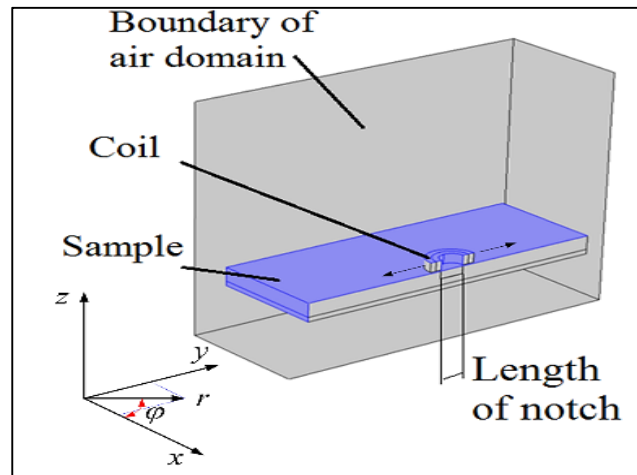


Figure 2.3 The 3D-half model developed in Comsol to reproduce the results presented in (Burke, 1988) for an absolute coil EC probe. A circular coil, a defective plate and the encompassing air domain are shown

It comprises an aluminum block with a rectangular surface notch located in the middle of the block's surface, a hollow cylindrical conductor representing a coil and a rectangular prism

domain encompassing all the components. All the dimensions used in this model are taken from (Burke, 1988), except for the sizes of the aluminum block and the air domain, which are set to minimize the runtime of the finite element (FE) solver. The material properties of aluminum, as taken from (Burke, 1988), is assigned to the defective block. The properties of air have been assigned to the air domain surrounding the coil and the conductor block.

Instead of a multi-turn coil's winding, the hollow cylindrical conductor is defined with the multi-turn coil domain feature of Comsol. This enables direct specification of coil's properties such as the number of turns, as well as the conductivity and the gauge of the wire. The multi-turn coil domain feature of Comsol is useful when modelling the inductors with a highly compact number of coil turns at low operating frequencies. In this case, it is possible to assume that the current density is distributed uniformly over the coil's cross section. The coil is excited by an alternating current  $I$  with magnitude of 1A, and the current density of a circular multi-turn coil domain is calculated through

$$\mathbf{J}_e = NI / S \quad (2.1)$$

where  $N$  is the number of windings, and  $S$  is the cross sectional area of the cylindrical object to which the coil domain has been assigned to.

It is worthwhile to mention that, according to Burke's study, the scan direction is parallel to the notch's length. So, to simulate this scan, the absolute coil is moved over a 20 mm range along the notch's centerline. The corresponding coil impedance is computed for each displacement step of 2.5 mm starting at the center of the notch.

### 2.3.1 Governing electromagnetic equations

The "Magnetic Field Physics" package in Comsol version 5 is selected for FE simulations. The governing equation for the magnetic field interface is based on the Maxwell-Ampere's law.

$$\nabla \times \mathbf{H} = \mathbf{J} + \partial \mathbf{D} / \partial t \quad (2.2)$$

where  $\mathbf{H}$  is the magnetic field intensity,  $\mathbf{J}$  is the current density, and  $\mathbf{D}$  is the electric flux density. The current density ( $\mathbf{J}$ ) can be expressed as the sum of the externally applied current density ( $\mathbf{J}_e$ ) and the induced current density ( $\mathbf{J}_{in} = \sigma \mathbf{E}$ ), where  $\sigma$  stands for conductivity and  $\mathbf{E}$  for electrical field intensity. The constitutive equations are (Stratton, 2007):

$$\mathbf{H} = \mathbf{B} / \mu \quad (2.3)$$

$$\mathbf{B} = \nabla \times \mathbf{A} \quad (2.4)$$

$$\mathbf{D} = \epsilon \mathbf{E} \quad (2.5)$$

$$\mathbf{E} = -\nabla V - \partial \mathbf{A} / \partial t \quad (2.6)$$

where  $\mu$  is the magnetic permeability,  $\mathbf{B}$  is the magnetic flux density,  $\mathbf{A}$  is the magnetic vector potential,  $\epsilon$  is the electrical permittivity and  $V$  is the electrical potential applied to the system. It shall be noted that, in the current problem,  $\nabla V = 0$ . Substituting equations (2.3 to 2.6) into the equation (2.2) and considering time-harmonic functions leads to:

$$(\nabla \times (\nabla \times \mathbf{A})) / \mu + (j\sigma\omega - \omega^2\epsilon)\mathbf{A} = \mathbf{J}_e \text{ where } j = \sqrt{-1} \quad (2.7)$$

where  $\omega$  is the angular frequency. Comsol solves equation (2.7) in the frequency domain.

Generally speaking, in the low frequency regime, where the electromagnetic wavelength is much greater than the size of the system, it is possible to assume that the quasi-static form of the Maxwell's equations can be used ( $\sigma \gg \omega\epsilon$ ). Although, in such a case, the displacement current term ( $\partial \mathbf{D} / \partial t$ ) is generally excluded from the calculations, the equation embedded in the magnetic field package of Comsol takes it into account without any solution cost.

### 2.3.2 Extent of the simulation domain

Generating an unbounded or infinitely extended air domain in FE simulations has been a long-standing issue for many physical problems. In terms of execution time, it is beneficial to truncate this domain to an extent in which the simulation results remain reliable. Fortunately, in eddy current problems, the region of practical interest can be limited to a bounded domain large enough to capture a reasonable amount of the coil's electromagnetic field. Truncating the block domain requires special attention to avoid that edge effects spoil the final results. To this end, the fields are initially solved according to a 2D-axisymmetric model for a large  $500 \text{ mm} \times 500 \text{ mm} \times 12 \text{ mm}$  un-defective block surrounded by a  $600 \text{ mm} \times 600 \text{ mm} \times 600 \text{ mm}$  air domain. Figure 2.4 shows the contour plots of the  $\varphi$  component of the magnetic vector potential  $A$  projected on the  $r$ - $z$  plane passing through the center of the coil, where  $\varphi$ ,  $r$  and  $z$  are the components of a cylindrical coordinate system. The air domain is then truncated around the region where the intensity of the magnetic vector potential drops to 0.1% of its maximum value. The width and length of the conductive block domain are also shortened with respect to the truncated size of the air domain such that each of the block's lateral faces is 10 mm apart from the nearest wall of the air domain. A new simulation is performed with this truncated model and the results do not reveal any changes in the field distribution meaning that no edge effects are introduced by truncating the model's domains to the aforementioned extent. It shall be noted that the changes in the distribution of the electromagnetic fields caused by the presence of a notch just occur locally around the notch itself. Hence, it is safe to assume that the field distribution at the boundaries of the air domain remains unchanged after introducing the notch. The truncated domain can therefore be used for further simulations of this absolute coil model.

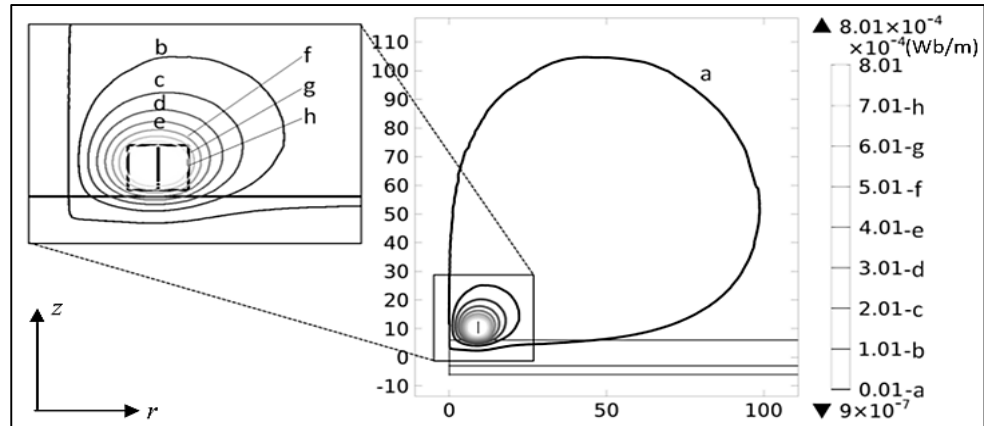


Figure 2.4 Contour of the  $\varphi$  component of the magnetic vector potential  $A$  given by a 2D-axisymmetric model of an absolute coil located over an extremely large (500 mm $\times$ 500 mm $\times$ 12 mm) un-defective sample.  $r$  and  $z$  values are in mm. According to (Burke, 1988), simulation is performed with an operating frequency of 900 Hz

### 2.3.3 Mesh assignment

A sound understanding of the impact caused by each FE parameter on the model is critical for attaining accurate simulation results. The mesh sizes (*i.e.* the density of finite elements) as well as the distribution of these elements within the model are certainly two of them. Mesh is a geometrical dependent feature. While generating the elements within each domain, special attention has to be paid to the physics used and to the dimensions of the domain. It is also important to have a satisfactory resolution for the solved fields, which is fully dictated by the element's type and size.

In the current problem, the aluminum block is partitioned using a cylindrical surface in order to create a more concentrated mesh underneath the coil. The diameter of the partitioned region is twice the diameter of the coil. When surface scanning is simulated using parametric sweep, this cylindrical region in the aluminum block moves together with the coil at each displacement step so as to always maintain the concentrated mesh underneath the coil.

Because of the skin effect, eddy currents are almost completely contained within the first three standard penetration depth ( $\delta$ ) as defined by

$$\delta = \sqrt{\frac{2}{\omega\mu\sigma}} \quad (2.8)$$

So, resolving the induced currents within their first three standard penetration depth, which is 3 mm, is crucial for obtaining the correct values of the coil's complex impedance. Initially, six boundary layer meshes made of second order elements have been generated for this region within the aluminum block. Later, the number of layers has been optimized according to the sensitivity of the simulated signals to this parameter. Apart from these critical regions, free tetrahedral meshes have been created in the rest of the model's geometry including the coil domain.

In order to get accurate simulation results in the shortest computational time, a sensitivity study is performed with respect to mesh size. For this study, the mesh is generated manually for each simulation step in order to have a better control on its distribution within different regions. The sensitivity of the simulation results in terms of mesh sizes is studied in two stages. First, the number of boundary layer meshes is kept at a constant value (six across the  $3\delta$  depth within the aluminum block) while the total number of elements in the entire model is changed (*i.e.*, the element's size in the coil and aluminum block domains is refined in 3 steps). The computed impedance data are then compared to the Burke's measurements (Burke, 1988). In each step, regardless of the total number of elements, the mesh sizes in the coil and aluminum block domains are equally scaled such that the corresponding maximum size ratio remains constant. This approach enables to keep the mesh quality within an acceptable level and avoid the adverse influence of low element quality in the solution. In the second stage of this study, the best element size obtained previously is applied to all domains and kept constant. Then, the number of boundary layer meshes is varied from 1 to 3 per  $\delta$  depth within the aluminum block. It is noteworthy that for mesh sensitivity studies the conductivity of air is initially set to 1 S/m, as suggested by Comsol's guides.

Figure 2.5(a) and Figure 2.5(b) show the variations of the coil's resistance and inductive reactance, normalized by the impedance measurements of Burke (Burke, 1988), for different element sizes as the coil scans the aluminum block containing a notch, respectively. In the normalization process, at each scanning position, the coil's inductive reactance and resistance measured by Burke are subtracted from the estimated values by simulations, and the results are divided by the maximum variations of the reported impedance measurements. The normalization scheme is in place to compare the error of the estimated impedance components and to study the convergence of the solver as different element sizes are selected. For better understanding, the coil scanning positions relative to the notch are shown schematically for 5 different coil displacements in Figure 2.5(c). According to Figure 2.5(a), changing the maximum element size for the aluminum block from 1.4 mm to 2 mm does not introduce any significant change in the resistive part of the impedance and, regardless of the scan position, the error always remains below 2%. However, the solver becomes unstable for an element size of 4 mm, resulting in unreliable resistance values for the coil. This means that element size needs to be small enough to capture the resistive losses caused by eddy currents inside the conductor. On the other hand, the error connected to the coil's inductive reactance has the same values at element sizes of 2 mm and 4 mm position wise. Furthermore, as the element size is further reduced to 1.4 mm, the inductive error is decreased by only 0.5 %. Although impedance estimations with the lowest level of error are achieved through meshing the block with the smallest element size of 1.4 mm, such a parameter increases the computational expenses unreasonably. Therefore, to avoid lengthy computational time, a maximum element size of 2 mm is selected knowing that the solver converges to consistent impedance estimations.

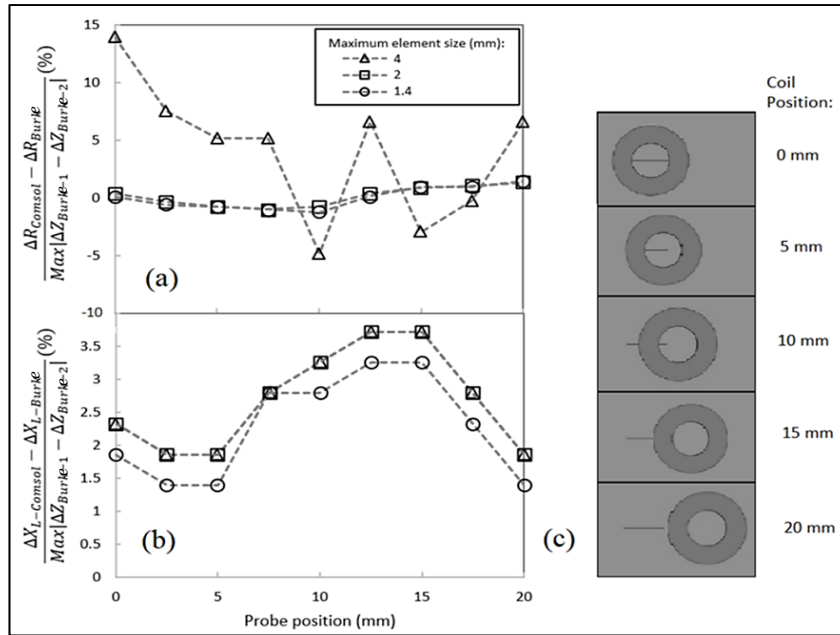


Figure 2.5 Effect of the element size on the normalized computed absolute coil's (a) resistance and (b) inductive reactance as it scans an aluminum block containing a notch, (c) Schematic of the coil position with respect to the notch location. Results are normalized by the magnitude of impedance variation in the Burke's measurements (Burke, 1988)

Figure 2.6(a) and Figure 2.6(b) depict the variations of the normalized coil's resistance and inductive reactance as a function of the coil's position for three different numbers of boundary layer meshes. The normalization scheme is similar to the one used in the previous case. As it can be observed in Figure 2.6(a), the coil's resistance is underestimated up to the scan position of 10 mm. This error is larger for 3 boundary layers as compared to the one obtained by 6 and 9 boundary layers. The estimation error becomes positive for the remaining probe positions where 6 boundary element layers provide the best estimation. For computed inductive reactance presented in Figure 2.6(b), estimated values are overestimated at all scan positions, similarly to the behavior seen in former sensitivity study. After comparing the effect of different boundary layers on coil's resistance and inductive reactance, it is evident that the estimated values using 6 and 9 boundary layers are closely attached together at each scan position. This suggests that the solver already converges with 6 boundary layers and that applying additional boundary layers would undoubtedly result in

an undesired increase of the computational time. Accordingly, 6 boundary layered elements should be sufficient across the first  $3\delta$  depth.

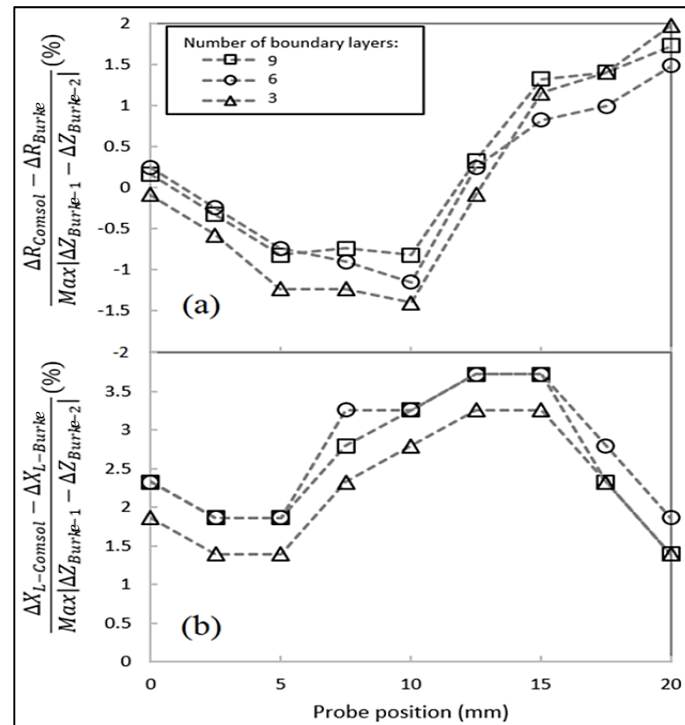


Figure 2.6 Effect of the number of boundary layers applied in the first three eddy current penetration depths on the normalized computed absolute coil's (a) resistance and (b) inductive reactance as the coil scans an aluminum block containing a notch.

Results are normalized by the magnitude of impedance variation in the Burke's measurement (Burke, 1988)

### 2.3.4 Conductivity of the air domain

Whenever a multi-turn coil domain is used in a frequency domain study within Comsol, the convergence of the solver toward a solution for the electromagnetic field equation (COMSOL, 2007) depends on the conductivity value of the surrounding air domain. A null value does not allow the solver to converge, while a very small value would delay the iterative solver's convergence remarkably. Therefore, the sensitivity of the simulation results

versus the air conductivity is studied in order to gain an idea about the optimum value for this parameter. It is important to choose the conductivity value judiciously, such that the execution time would be short and the results satisfactory. For this purpose, four conductivity values of 0.01, 0.1, 1 and 10 S/m are assigned to the air domain. The corresponding simulation results are presented in Figure 2.7.

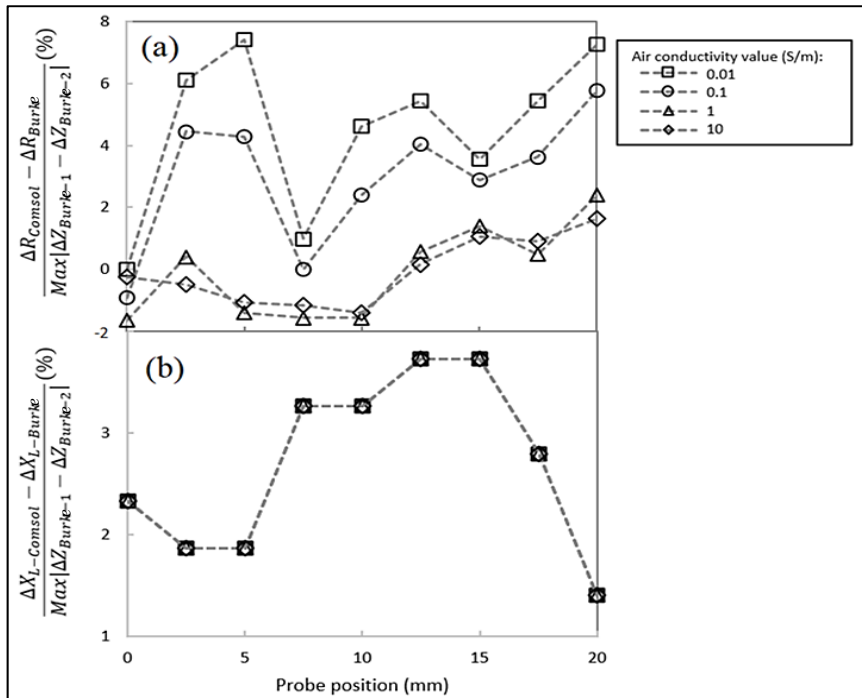


Figure 2.7 Effect of air conductivity on the normalized computed absolute coil's (a) resistance and (b) inductive reactance as the absolute coil scans an aluminum block containing a notch. Results are normalized by the magnitude of impedance variation in the Burke's measurements (Burke, 1988)

From Figure 2.7(a), it is clear that the difference between the estimated values using air conductivity of 10 S/m and 1 S/m is very small whereas, estimated error becomes larger for smaller conductivity values. According to Figure 2.7(b), the coil's reactance is not influenced by the simulation parameters. Because unreasonably large air conductivity values could affect the physics of the problem, the air conductivity of 1 S/m is preferred over others. In

addition, as a rule of thumb in Comsol, the ratio between the conductivities of air and of conductor (20 MS/m for aluminum) must be in the range of  $10^{-6}$  to  $10^{-8}$ .

### 2.3.5 Computed impedance with the optimized model parameters

The optimized simulation parameters, as concluded from the previous sensitivity studies, are applied to the model and the estimated values for the resistive and the inductive parts of the impedance are superimposed on the measured plots, provided by Burke's study, in Figure 2.8(a) and Figure 2.8(b), respectively. Although Figure 2.8 shows a quite good fit with experimental data, a small discrepancy between the calculated and the measured impedance components is observed at each scan position. Regardless of the parameters in use, the calculated inductive reactance is always at least 1.5 % higher than the measured values. Deeper investigation into the model indicates that the reference edge specified within the circular coil's model, which determines the direction of current flow in a relatively thick-sectioned coil, can affect the computed coil's impedance. Based on the instructions provided by Comsol for modelling 3-D coils (COMSOL, 2012), choosing a closed loop running through the middle of the circular coil's thickness is expected to provide the best computed impedance values. In an attempt to improve the accuracy of the model, the effect of the position of the reference edge would thus require further investigation. Fortunately, this issue is not a concern in the modelling of split-D probes, where the coils' cross sections are far thinner (*i.e.*, one or two layers of AWG 22 wires). Additionally, they are modelled through numeric multi-turn coil domains instead of circular multi-turn coil domains. In such a modelling tool, there is no need to specify reference edges since the direction of the current is determined by defining an additional step within the solver.

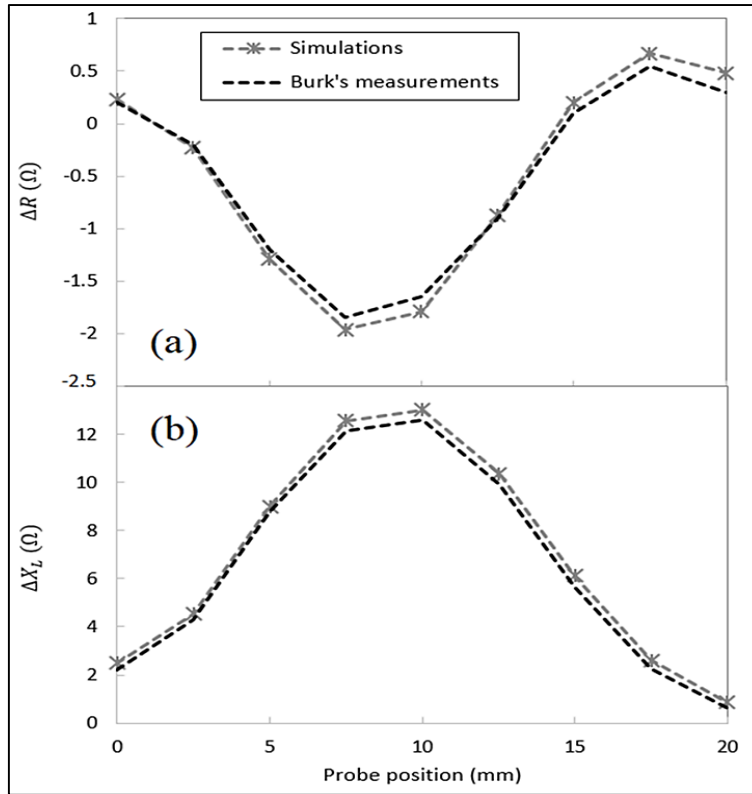


Figure 2.8 Calculated values of the absolute coil's (a) resistance and, (b) inductive reactance as the coil scans over a notch. Comparison with impedance measurements extracted from Burke's work (Burke, 1988)

## 2.4 FEM analysis of a split-D differential coil

A half scale 3-D CAD model for a differential probe is developed in Comsol based on the probe's dimensions presented in Table 2.1. Instead of generating a complex CAD model for the coils including all coil turns and the corresponding geometrical complications such as winding angles and separations, three solid domains are generated for the coils, and the multi-turn coil domain within Comsol is assigned to each of them. Two solid geometries are created for the cores by cutting in half a cylinder across its diameter. A hollow cylinder is also created for the probe's shielding, and all components are assembled properly respecting the dimensions of the commercial split-D probe. A very small 0.03 mm lift-off is introduced to the probe's model according to experimental setup.

Unlike the scan path used in the experimental tests (-2 mm to +2 mm), it is optimized for simulations to shorten the time of the solver. Therefore, simulations are performed in the range of 0 to 1.3 mm (*i.e.*, starting from a position where the center of the coil is aligned with the notch's centerline, and ending at a position where the coil is 1.3 mm away from the notch's centerline). The complete impedance signal is supposed to be a perfect mirror image of the signal so obtained, resulting in the distinctive 8-shaped signal. Usually, the simulations at 0.1 mm steps along the scanning path are carried out all together in a single run. In few cases, however, due to the complexity of the mesh structure, each 0.1 mm scanning step is treated individually.

A 6V, 500 kHz alternating voltage is applied to the driver coil and both receiver coils are considered open (no current flow through them). At every scanning step, the voltage across each of the two receiver coils is obtained. As given by equation 2.9, the differential impedance of the probe ( $\Delta Z$ ) can be expressed as the difference of voltages across the serially connected receiver coils ( $V_{R2} - V_{R1}$ , where  $V_{R1}$  and  $V_{R2}$  are the voltages across the receiver coils 1 and 2, respectively) divided by the current flowing in the driver coil ( $I_D$ ).

$$\Delta Z = (V_{R2} - V_{R1}) / I_D \quad (2.9)$$

Because the differential voltage for un-defective block is extremely small (theoretically zero),  $\Delta Z$  represents the variation of the probe impedance with respect to the one obtained in sound areas of the sample.

The Nortec-500 flaw detector, the equipment used to experimentally acquire impedance data in the current work, provides relative impedance values rather than absolute ones. Therefore, in order to enable comparison between simulated and measured impedances, data conversion procedure is required. As previously mentioned, the relative probe impedance, which is displayed on the Nortec screen as a moving dot, is collected through the acquisition of two voltage signals ( $V_H$  and  $V_V$ ), which are respectively proportional to the horizontal and the

vertical positions of the dot on the screen. These two voltages are first combined into a complex phasor given by

$$\Delta V = (V_H - V_{H0}) + (V_V - V_{V0}) \cdot j = M \angle \theta \quad (2.10)$$

$$\text{where } M = \sqrt{(V_H - V_{H0})^2 + (V_V - V_{V0})^2} \quad (2.11)$$

$$\text{and } \theta = \tan^{-1} \left( \frac{V_V - V_{V0}}{V_H - V_{H0}} \right) \quad (2.12)$$

With the horizontal and vertical gains selected on the Nortec system equally to be 56 dB,  $\Delta V$  shall be systematically multiplied by 0.0016 ( $\Delta V_2 = \Delta V_1 / (10^{(gain/20)})$ ), and phase shifted by 22 degrees clockwise to be able to compare the results of measurements to simulated  $\Delta Z$  values. This phase shift is believed to be due to the Nortec amplification circuitry that could introduce a gain and a frequency dependent phase shift in the displayed signal.

Following the same development described in Section 2.3 for the modelling of the absolute coil, a sensitivity analysis is carried out for the case of the split-D differential probe to understand how the changes in the model's parameters affect the simulation results.

#### 2.4.1 Extent of the simulation domain

Depending on the probe lift-off, the operating frequency, the probe shielding, the coils' geometry and their configuration, the effective probe footprint may vary. Accordingly, because the operating frequency is significantly higher and the probe geometry much smaller, the truncation sizes of the air and aluminum block domains, as deduced in Section 2.3, are no longer applicable to the case of the split-D probe. However, in order to reduce the computation time, the air and aluminum block domains are still truncated following the same strategy based on the magnitude of the magnetic vector potential. Figure 2.9 illustrates the contour map of the magnetic field potential component perpendicular to the symmetry plane at 500 kHz along with the model's initial mesh distribution. As demonstrated, the outermost

contour shows the region at which the amplitude of vector potential reduces to approximately one thousandth of its maximum value. Since the vector potential field is concentrated inside the shielding, the air domain can be truncated up to twice the size of the shielding diameter.

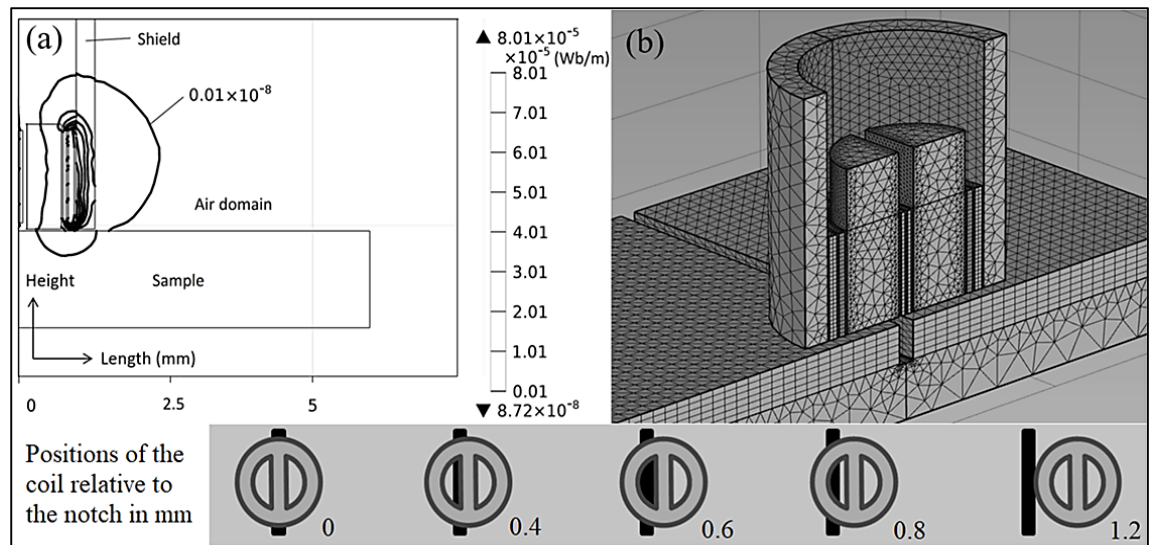


Figure 2.9 (a) Contour map of the magnetic vector potential component perpendicular to the symmetry plane at 500 kHz for a split-D probe over an un-defective aluminum block, (b) model's mesh distribution for a split-D probe scanning an aluminum block with a 0.503 mm deep notch

## 2.4.2 Mesh size

To study the dependency of the simulation's results on the mesh element size, the maximum element size in the aluminum block domain is changed in three steps while the element size of other domains is scaled proportionally. Based on the conclusion given about the absolute coil model (Section 2.3), an air conductivity value of 1 S/m is initially used for the simulation of the split-D probe's model. The material properties presented in Table 2.1 are also assigned to each component of the model. This study is performed for the cases of both the shallowest (0.188 mm deep) and the deepest notches (1.008 mm deep).

Figure 2.10 and Figure 2.11 show the variations of the real and imaginary parts of the normalized probe's impedance scanning over the 0.188 mm and the 1.008 mm deep notches, respectively. The same normalization scheme used in section 2.3 is applied here however, the curves are normalized by the impedance measurements of the notches using the split-D probe. According to these figures, imaginary and real parts of the computed impedance seem to converge as a total number of 388,000 mesh elements are used in the model. In order to leave some room for higher resolution results, a total number of 690,000 volumetric tetrahedral elements will be used for this probe model in the following simulations.

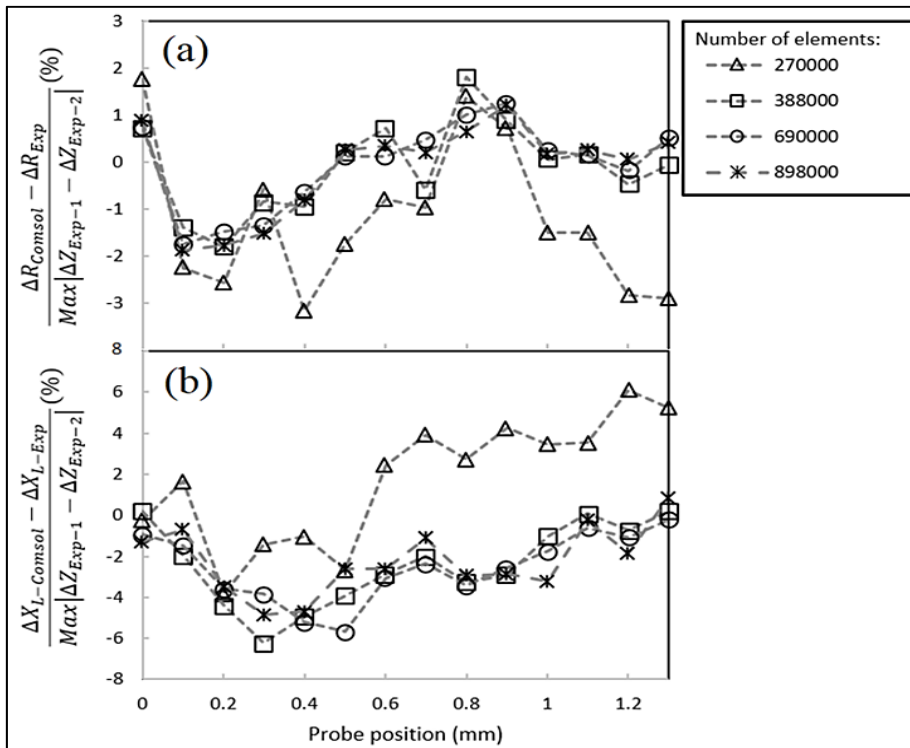


Figure 2.10 Effect of the element size on the normalized computed (a) real and (b) imaginary parts of the differential impedance for a 0.188 mm deep notch in an aluminum block. Simulations are performed using four different numbers of volumetric tetrahedral elements

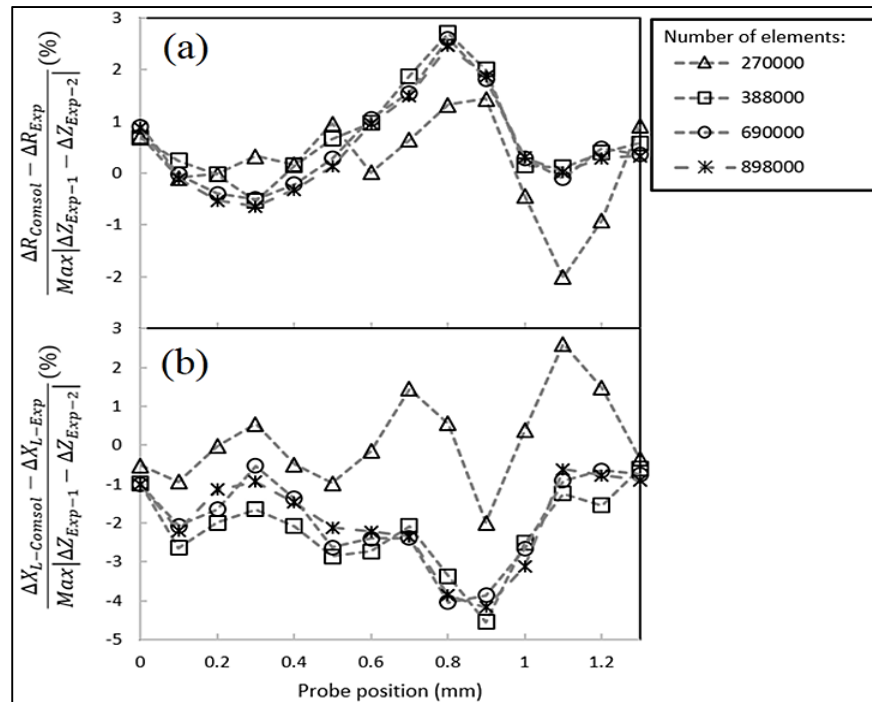


Figure 2.11 Effect of the element size on the normalized computed (a) real and (b) imaginary parts of the differential impedance for 1.008 mm deep notch in an aluminum block. Numerical simulations are performed using four different numbers of volumetric tetrahedral elements

### 2.4.3 Conductivity of the air domain

Similar to the sensitivity studies performed about the absolute coil model (Section 2.3), the sensitivity of the simulation results to the value of air conductivity is repeated for the split-D probe model. For this purpose, three values of air conductivity, namely 0.1, 1 and 10 S/m, are considered. Figure 2.12 demonstrates the impact of this parameter on the real and imaginary parts of the normalized probe's impedance as the probe scans a 1.008 mm deep notch. As revealed by Figure 2.12, choosing the highest value of 10 S/m for the air conductivity affects the imaginary part of the normalized impedance and therefore, the solution becomes unstable. Based on these results, the air conductivity of 1 S/m seems to provide the most reliable estimations and this is clearly in agreement with the case of the absolute probe presented in Section 2.3.

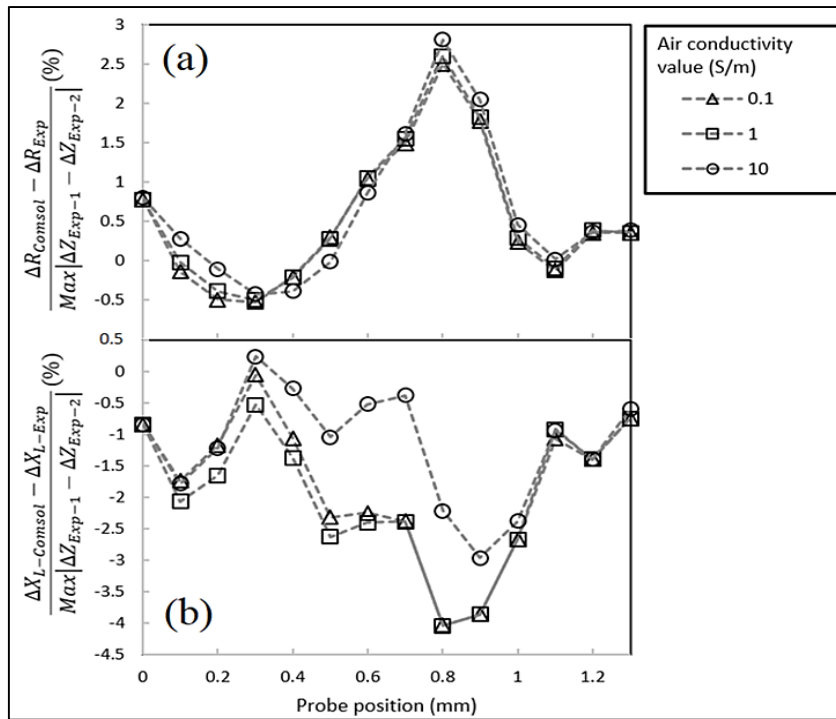


Figure 2.12 Effect of air conductivity on the normalized computed (a) real and (b) imaginary parts of the differential impedance for 1.008 mm deep notch in an aluminum block. Numerical simulations are performed for three different values of the air conductivity

#### 2.4.4 Simulation results and discussion

The response of the split-D probe is here investigated numerically and experimentally as it scans three EDM notches with different depths engraved on an aluminum block. Measured and numerically calculated imaginary and real parts of the differential probe impedance are shown in Figure 2.13, Figure 2.14 and Figure 2.15 for 1.008, 0.503 and 0.188 mm deep notches, respectively. Figure 2.16(a), Figure 2.16 (b) and Figure 2.16 (c) display, on an impedance plane, the same results as the ones presented in Figure 2.13, Figure 2.14 and Figure 2.15, respectively. All the three impedance planes of Figure 2.16 are shown with the same scale to ease comparison between the given signals. Again, because of the symmetry of the model, only a single loop of the 8-shaped signal is shown.

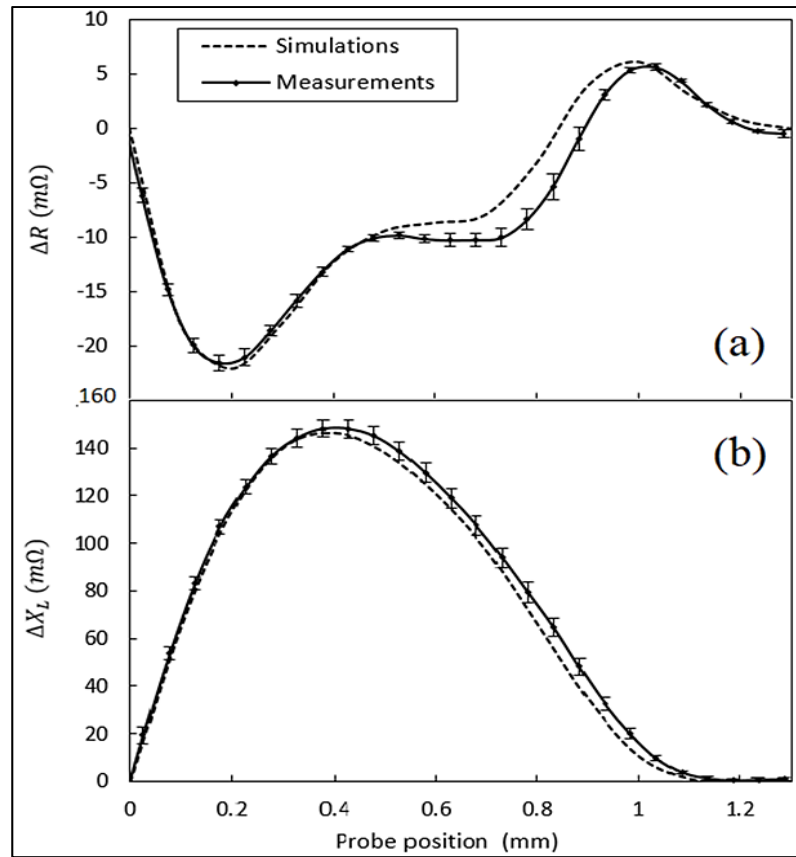


Figure 2.13 Imaginary (a) and real (b) parts of the differential impedance obtained through numerical calculation and measurement with the Nortec-500 flaw detector for a 1.008 mm deep notch in an aluminum block

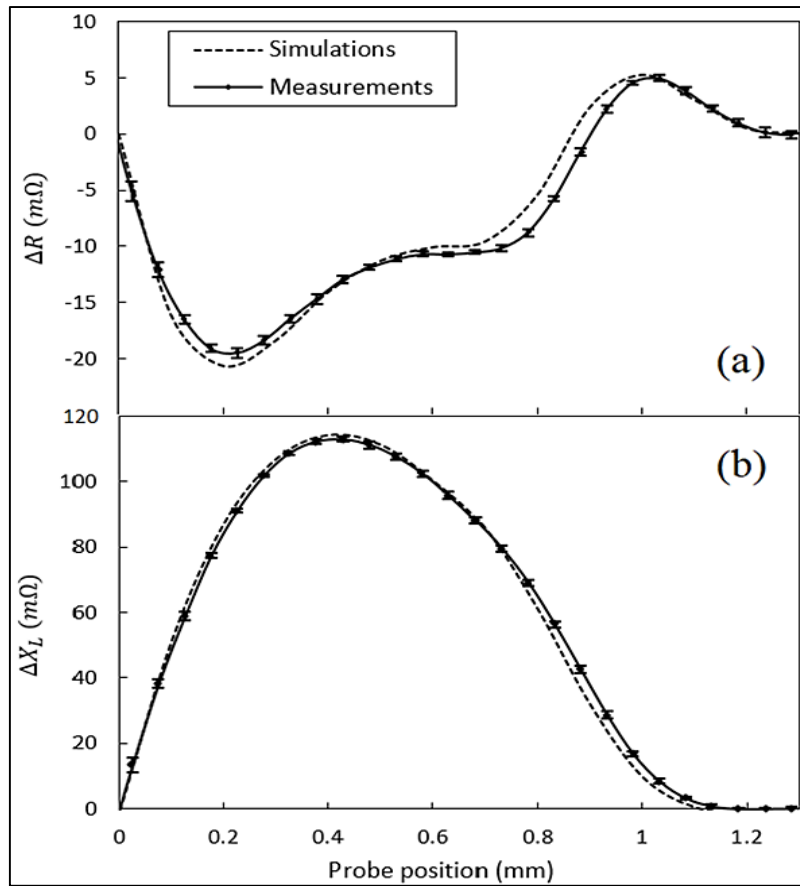


Figure 2.14 Imaginary (a) and real (b) parts of the differential impedance obtained through numerical calculation and measurement with the Nortec-500 flaw detector for a 0.503 mm deep notch in an aluminum block

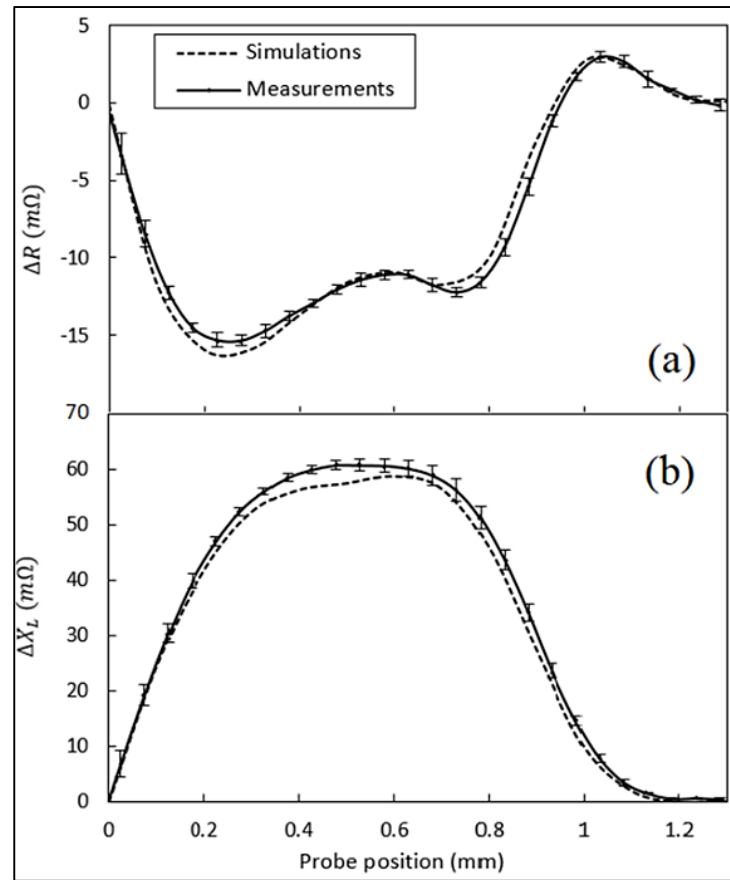


Figure 2.15 (a) Imaginary and (b) real parts of the differential impedance obtained through numerical calculation and measurement with the Nortec-500 flaw detector for a 0.188 mm deep notch in an aluminum block

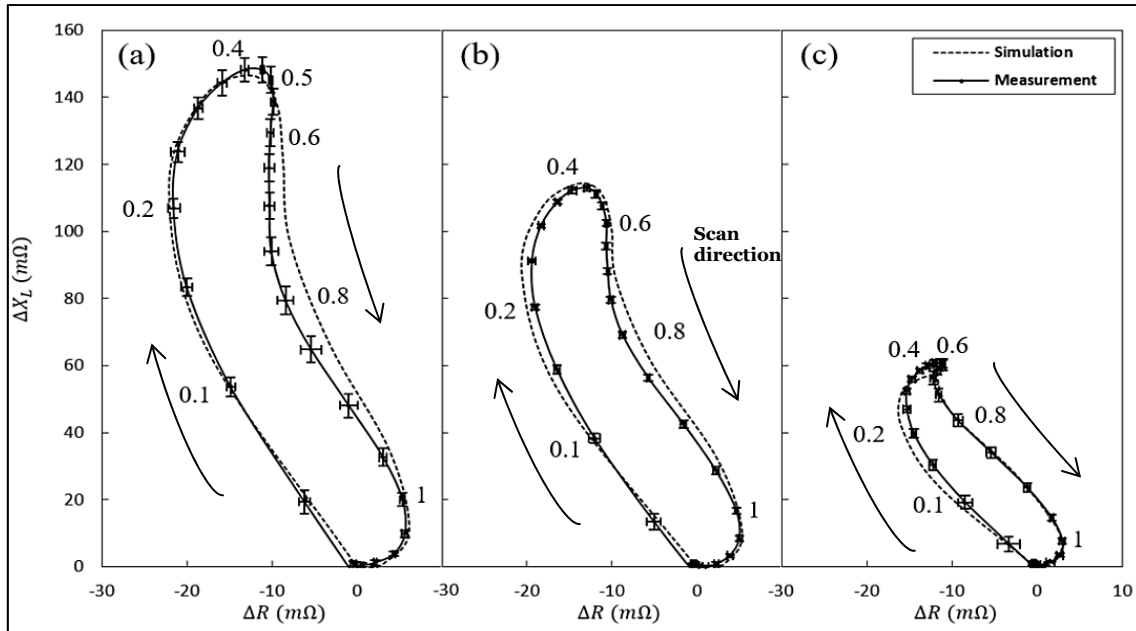


Figure 2.16 Single loop of the 8-shaped signals obtained by plotting the imaginary and real parts of the probe's impedance (Figures 2.13, 2.14 and 2.15) directly on the impedance plane. (a) 1.008 mm , (b) 0.503 mm and (c) 0.188 mm deep notch

Referring to Figure 2.13, Figure 2.14, Figure 2.15 and Figure 2.16, it is observed that the shape of simulated and measured results is in good agreement for all the notches. The most significant discrepancy appear in the imaginary component of the impedance. From Figure 2.10 and Figure 2.15 (the shallowest notch), it could be seen that the imaginary part is underestimated by 6 % at a probe position of about 0.5 mm. This discrepancy in the imaginary part of the probe impedance is reflected in the signal peak of the simulated complex impedance loops in Figure 2.16(c). Moreover, referring to Figure 2.11 and Figure 2.13 (the deepest notch) the signal is underestimated by 4 % at the scan position of 0.8 mm. This deviation of simulation form measurement appears as widening of the simulated signal in Figure 2.16(a). Otherwise, most of the simulated impedance values are contained within the measurement error. To derive the error, each of these notches is scanned 5 times using the split-D probe and the impedance variations in each scan are recorded. Afterwards, the mean value and the standard deviation ( $\sigma$ ) of the 5 impedance measurements are calculated for each notch. Accordingly, the measurement error is presented by  $\pm\sigma$  at each probe's position.

Discrepancies between simulated and measured impedances are believed to be somehow related to the deviation of the manufactured notches geometry from the ideal simulated ones (rectangular slot). In an EDM process, thin electrodes are used to erode narrow surface notches. As the notch gets deeper, the electrode's lateral faces may further remove metal from the notch walls. Accordingly, the resulting notch is wider in the vicinity of its opening than at its tip. This nonuniformity grows by increasing the nominal depth of a notch. Correspondingly, referring to Figure 2.12, we find that the largest discrepancy in the width of the complex impedance loops is occurring with the deepest notch. Dimensions and properties of the probe components used in the model could also contribute to observed discrepancies. In addition, as the notch gets shallower, the sensitivity of the probe's signal to geometrical imperfections grows significantly. Accordingly, the largest discrepancy between simulations and measurements is observed for the shallowest notch.

The desired precision level of each signal's feature is strongly application-oriented. For instance, in order to have a good estimation of the crack characteristics in inversion approaches, the crack signals shall be accurately reproduced using modelling. However, the importance of signal shape and phase is undoubtedly less in reliability studies (POD studies) where the signal amplitude is the primary influential factor (Lemire et al., 2010; P. R. Underhill & T. W. Krause, 2011). Nonetheless, results reported in this work confirm that COMSOL model can reasonably predict probe impedance variations (in shape and amplitude) as it is scanned across a notch.

The use of such a model could also help to properly design a specific probe as the impact of design parameters on probe performances could be accurately simulated. Indeed, in addition to probe impedance, magnetic and electric vector fields could be displayed to understand the probe behavior. As an example of this, Figure 2.17 shows the surface distribution, using the vector field representation, for the  $z$  and  $x$  components of  $\mathbf{J}_{in}$  (induced current density) in the vicinity of 0.188 mm deep notch for three different probe positions over this notch.

Moreover, beneath these figures, the surface distribution for the  $y$  and  $x$  components of  $\mathbf{H}$  (magnetic field intensity) is depicted as well.

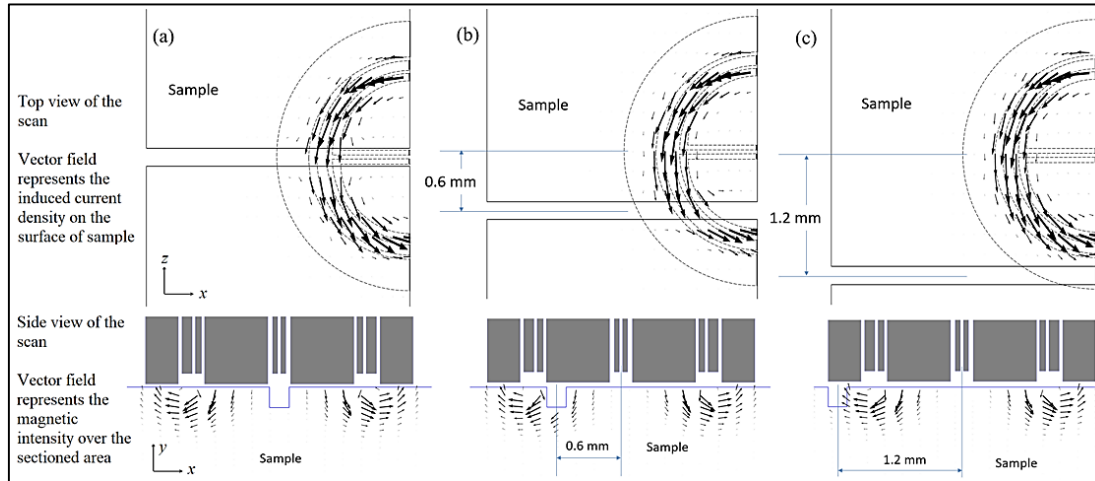


Figure 2.17 Distribution of the  $z$  and  $x$  components of the induced current density, represented by a vector field, in the vicinity of the 0.188 mm deep notch as the probe is displaced by (a) 0 mm, (b) 0.6 mm and (c) 1.2 mm. Side view of the scan shows the distribution of the  $x$  and  $y$  components of the magnetic field intensity

As demonstrated, the surface current density is significantly perturbed at the scan positions of 0 mm and 0.6 mm. At the scan position of 0 mm, the perturbation is seen by both of the receiver coils equally. However, at the scan position of 0.6 mm, the notch and its corresponding perturbation zone are directly located underneath one of the receiver coils. This results in the maximum amplitude of the differential impedance of the receiver coils for the shallowest notch.

## 2.5 Summary and conclusions

In this paper, a model based study of an absolute probe and a split-D reflection differential surface probe is performed using Comsol Multiphysics. The half scale 3-D model of the absolute coil is generated and the numerical simulations are carried out for the scan of a rectangular notch engraved on aluminum as per the Burke's benchmark problem (Burke, 1988). In an attempt to obtain reliable results, sensitivity to two simulation parameters have

been studied, namely the air conductivity and the model mesh size. Simulations revealed that an air conductivity of at least 1 S/m is required to allow the model to converge in a reasonable timeframe. Similarly, it has been found that the optimum mesh parameters was to use 6 boundary layer meshes across the first three penetration depths in the conductor block, with a maximum element size of 2 mm. Based on these parameters, a quite good agreement is achieved between the numerical results and the benchmark measurements (Burke, 1988). In fact, the error on the estimation of the coil's resistance is less than 2% of the impedance variation range while it is less than 4% for the coil's inductive part. It has also been noted that the coil's inductive reactance was always overestimated by the model (by at least 1.5%) most likely because of a parameter used to define the direction of current flow in a relatively thick-sectioned coil.

Taking advantage of the knowledge acquired from the Comsol simulation of the absolute probe, a half scale 3-D model of a commercial split-D reflection differential surface probe has been investigated as well. Similar to the previous case, a sensitivity study to the same two simulation parameters has been carried out. For this smaller probe operating at a much higher frequency (500 kHz), an optimum air conductivity of 1 S/m has been found together with a minimum number of 388,000 volumetric elements in the model. Again, 6 boundary layer meshes across the first three penetration depths in the conductor block have been used. Based on these parameters, the computed impedance values have been found to pretty much match measurements. Only a slight widening of the simulated complex impedance loops has been observed. This minor discrepancy is believed to be due to non-ideal notch geometry in the measurements or inaccurate constituents' dimensions or properties in the numerical probe model. The objective of the present work was to evaluate the reliability of Comsol Multiphysics as a tool to accurately estimate a split-D probe impedance while it scans surface cracks. Results obtained herein seem to confirm that signal amplitude could be simulated to a level of accuracy that should be sufficient for probability of detection studies. However, if the goal is to characterize the crack depth and shape through a fuzzy logic inversion algorithm, accuracy of the model outputs shall be further improved. To do so, information

about probe's material and geometrical parameters need to be better defined. This aim will be pursued in future investigations

### **Acknowledgments**

This research is mainly funded by the Natural Sciences and Engineering Research Council of Canada (NSERC). The authors would like to acknowledge our collaborating industrial partners; Pratt and Whitney Canada, L-3 Communications and National Research Council of Canada (NRC). This work was performed as part of CRIAQ (*Consortium de Recherche et d'Innovation en Aérospatiale du Québec*) MANU-418 project. The authors wish to acknowledge the CMC Microsystems for providing access to computer aided design (CAD) software.

## CHAPTER 3

### ADAPTIVE NEURO-FUZZY INFERENCE SYSTEM TRAINED FOR SIZING SEMI-ELLIPTICAL NOTCHES SCANNED BY EDDY CURRENTS

Ehsan Mohseni<sup>a</sup>, Martin Viens<sup>a</sup>, and Wen-Fang Xie<sup>b</sup>

<sup>a</sup> Department of Mechanical Engineering, École de technologie supérieure (ÉTS),  
Montréal (Québec), H3C 1K3, Canada

<sup>b</sup> Department of Mechanical & Industrial Engineering, Concordia University, Montréal  
(Québec), H3G 1M8 Canada

Paper submitted to the Journal of Nondestructive Evaluation, June 2018

#### Abstract

The present study explores the capability of Comsol Multiphysics, as a finite element modelling (FEM) tool, to model the interaction between a split-D differential surface eddy current (ECT) probe and semi-elliptical surface electrical discharge machined (EDM) notches. The effect of the small probe's lift-off and tilt on its signal is investigated through modelling and subsequently, the simulation outcomes are validated using the probe's impedance measurements. In the next stage, an adaptive neuro-fuzzy inference system (ANFIS) is designed to take the signal features as inputs and consequently, provide the length of the scanned notch as the system's output. The system is trained by extracted features of thirty model-generated signals obtained from scanning of the same number of semi-elliptical notches by means of the split-D probe. The trained ANFIS is tested afterwards using the measured signals of 3 calibration EDM notches together with 5 model-based ones. A very low average estimation error is observed with regard to the length estimation of the test notches and the accuracy of the length estimation is found to be quite reasonable.

#### 3.1 Introduction

Depending on the configuration of eddy current testing (ECT) probes, diverse analytical and semi-analytical models have been in use to study the interaction of these probes with surface

and near surface flaws. Evolution of ECT probes through years in order to fit for sophisticated new applications adds to their complexity and hence, leads to adoption of numerical approaches for their analysis more than before. From such probe categories, reflection differential split-D probe as a conventional ECT surface probe has served long in nuclear and aerospace industries owing to the spatial configuration of its differentially connected receiver coils. It has a very small footprint, high signal to noise ratio for tiny surface breakings and least sensitivity to gradual variations of both conductivity and permeability (R. Mooers et al., 2012; Shull, 2016). The impedance evaluation for this probe as it scans defective components requires finding a solution to the forward problem developed based on Maxwell's equations. Most of these problems are tackled using semi-analytical approaches and deriving integral equations for electromagnetic fields using Green's dyadic functions (J. Bowler et al., 1990; J. Bowler et al., 1997; H. A. Sabbagh et al., 2013). Followed by these approaches, different studies investigated the performance of such probes through the developed volume integral code and some promising outcomes were presented using the method (J. Bowler et al., 1990; J. R. Bowler, Sabbagh, & Sabbagh, 1989). However, the availability of diverse numerical tools nowadays allows one to treat the problems such as the interaction between complex probe geometries and defects more realistically without the need of evaluating the complicated Green's function. Finite element modelling (FEM), as a well-known numerical method, is also very distinguished for its flexibility in processing complex geometries and has grown in popularity in ECT analysis in recent years since it is proved to be a competent mean. Unfortunately, the potential of the FEM in modelling of Split-D probes with non-axisymmetric geometries has not fully been explored yet. Accordingly, in the present study, FEM is exclusively used to compute the impedance of a split-D probe as it scans over 30 semi-elliptical electrical discharge machined (EDM) notches with different dimensions in order to form a size dependent signal archive. It is noted that semi-elliptical EDM notches are used to generate impedance trajectories since they can fairly be representative of surface fatigue cracks in terms of the shape (Yusa, Perrin, Mizuno, & Miya, 2007).

Employing various quantitative non-destructive testing techniques for crack sizing has become very important since the reliance of new structural life estimation approaches and maintenance decision-makings on accurate sizing has grown in various industries (Boukani, Viens, Tahan, & Gagnon, 2014; Iyyer, Sarkar, Merrill, & Phan, 2007). Reliable defect characterization and sizing through inversion of ECT signals can help one optimize the maintenance intervals which could result in the prevention of safety issues as well as the reduction in inspection costs. Therefore, due to their high importance, the inversion of ECT signals has been the concern of many studies in past. Most of the related publications are developed based on the Green's function with solution to ECT forward problem in form of volume integrals and the inversion is commonly carried out through minimizing a cost function representing the difference between the predictions made by the forward problem and the measurements of the probe (J. Bowler, 2000; Burke, 1994). ECT Inversion based on these approaches requires low computational resources and they are fairly fast and accurate. However, some preliminary assumptions regarding the medium and flaw are required. Although, FEM is not as fast as the other techniques and thus, cannot be used directly in inversion, one can effectively use FEM-generated impedance trajectories of surface notches in conjunction with artificial intelligence (AI) to produce a sizing scheme. Furthermore, the primary task to adopt such a scheme is ensuring the reliability of FEM predictions for ECT signals.

AI techniques such as fuzzy logic, neural networks, and genetic algorithms are developed based on the inspirations from biological and behavioural nature of human and they have been used in many real world applications. Integrating two or three of these techniques can be advantageous in designing intelligent soft computing systems (Tsoukalas & Uhrig, 1996). Soft computing has been in use in the field of flaw characterization and classification using ECT signals for a while (Grimberg, Savin, Iancu, & Chifan, 2000; Udpa & Udpa, 1991; Upadhyaya, Yan, Behraves, & Henry, 1999). Among all these approaches, neural networks (NN) and fuzzy logic (FL) are frequently used together either in series or as an integration to form hybrid systems in which the reasoning and inference power of the FL can be complemented by adaptive learning nature of NN.

In this paper, a hybrid system integrating NN and FL has been proposed for the notch length prediction. In FL, the values are transformed to membership degrees of linguistic information through fuzzy set theory by applying linguistic labels to which membership functions are assigned. Subsequently, a fuzzy inference system (FIS) composed of if-then rules is defined based on human perception and serves as the reasoning engine. Finally, the system outputs are defuzzified to quantitative values. Although the FIS is structured based on the human expertise, it does not adapt to changing environment. In order to optimize a designed FIS through training with sets of input/output data, an adaptive neuro-fuzzy inference system (ANFIS) can be of benefit. The training procedure for these systems requires several training data sets comprising of both known flaw dimensions and features of their corresponding signal. Fabricating such samples containing flaws with given dimensions is really costly and time consuming whereas modelling them by FEM allows one to generate as many signals as required to train ANFIS to cover a desired dimensional range for a certain flaw type. Therefore, in the present study ECT signals of the probe scanning over thirty notches with diverse lengths are obtained through FEM simulations in Comsol Multiphysics®. Afterwards, their signals are post-processed to extract the features which are fed as inputs to an ANFIS for training purposes. The initial Sugeno type FIS has the notch length as output. The trained system is tested subsequently using the measured signals of three calibration notches as well as the model-generated signals of 5 arbitrary semi-elliptical EDM notches.

In industries, the demand for automated inspections is growing every day. Automation can eliminate the errors introduced by human factor as well as reducing the cost and time of inspections. However, there are also a few drawbacks linked to automated scans. For instance in the case of ECT automation, the probe manipulation is of high importance since even a very small tool alignment/positioning error affects the ECT signal significantly. In ECT, such errors appear in form of probe's tilt and lift-off. Presence of any of these two can change the nature of the recorded signals of scanned flaws, which in turn introduces errors in crack characterizations. Therefore, the impact of small variations of the probe's lift-off and tilt on ECT signal is investigated through FEM as it scans notches. Subsequently, the extent of the

error introduced into sizing caused by these small probe lift-offs and tilt angles is examined through feeding their signal features into the trained FIS.

This study is organized in the following order. In section 3.2, the experimental setup and FEM preparations are explained. Initially, the credibility of FEM for predicting the probe's signal as the tilt and lift-off vary is assessed by comparing their simulation results to the impedance measurements. Afterwards, the effect of probe's tilt angle and lift-off variations on ECT signals of three calibration notches is investigated through simulations. In addition, a series of simulations concerning thirty semi-elliptical notches possessing different lengths and depths is performed and consequently, a size dependent table of the notch signals is formed (Mohseni, Viens, & Franca, 2016). In section 3.3, each of the signals is analyzed by means of a MATLAB script in order to extract their features such as the peak-to-peak amplitude, the maximum width and the shape type. Besides, an initial FIS is generated having the signal features as inputs and notch length as its output. The set of inputs and output related to each notch is prepared in form of vectors and used for training of ANFIS based on the hybrid method composed of back propagation and least squares optimization methods. Subsequently, the trained FIS is tested by the signals obtained from the 3 calibration notches. Additional tests are carried out using the model-based simulated signals of 5 EDM notches randomly sized within the length size interval used in the training. At last, the signals acquired from the three calibration notches as the probe's tilt angle and lift-off varies are analyzed. Following that, the extracted features of these signals are fed into the trained ANFIS to explore the level of error introduced in notch length estimation as a result of probe's tilt and lift-off variation.

### **3.2 Experiments and modelling**

Three semi-elliptical EDM notches in an aluminium 7075-T6 sample, as listed along with their dimensions in Table 3.1, are used for experimental measurements. The dimensional features of these notches are shown in Figure 3.1. The thickness of the aluminium sample is 6 mm and it is extremely thick as compared to the penetration depth of eddy currents at

selected test frequency of 500 kHz, which is approximately 50  $\mu\text{m}$ . A reflection differential split-D surface pencil probe working in frequency range of 500 kHz to 3 MHz together with a Nortec 500S ECT unit are used for scanning of the notches and recording the signals. The probe is fixed within an alignment device through which operator is able to set a tilt angle for the probe. The sample is mounted on an X-Y micrometric table which can be programmed to follow a scan trajectory. The experimental set up is demonstrated in Figure 3.2(a). An initial lift-off of 30  $\mu\text{m}$  is introduced to the probe and maintained during all the experimental and modelling scans. The probe is oriented in a way so that the flat surface of D-cores, cutting a cylinder in half, becomes parallel to the notch side wall. Besides, the perpendicularity of the probe to the sample's surface is ensured by checking the symmetry of the 8-shaped signal of a perpendicular to surface calibration through width notch. Afterwards, raster scans are conducted on each of the 3 notches in the way shown in Figure 3.2(b). The scans are performed with an index of 0.1 mm when the probe is tilted 0°, 2° and 4°. Figure 3.2(c) shows the tilt angle introduced to the probe while an initial lift-off of 30  $\mu\text{m}$  is in place. In this figure, the tilt axis, which is perpendicular to the scan direction, passes through point A and is parallel to the surface of the sample. After recording the signals for tilt angle variations, notch signals are also acquired at probe's lift-offs of 30  $\mu\text{m}$ , 100  $\mu\text{m}$  and 140  $\mu\text{m}$  with no tilt. The impedance data recorded via a data acquisition card possessing a high sampling rate relative to the scan speed. The scan data is then analyzed using a MATLAB script to indicate the scan line being the closest to the line which cuts the notch length in half (i.e. notch center line). Clearly, the accuracy of finding the scan line passing over the notch center line depends on the scan index, symmetry of the notch relative to the plane cutting it in half along its length, the probes internal imperfections and, the surface waviness and non-parallelism.

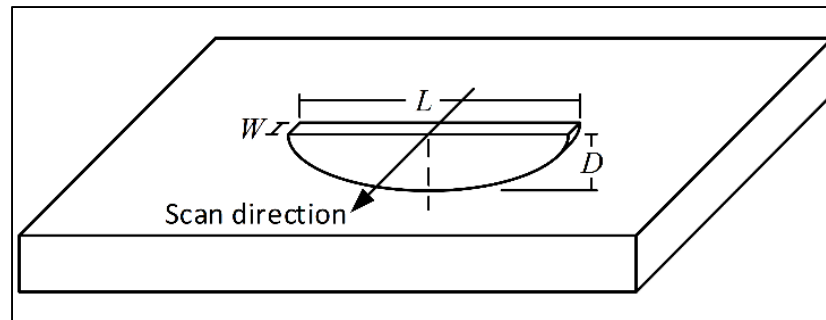


Figure 3.1 Geometrical features of a semi-elliptical notch

Table 3.1 Geometry of semi-elliptical EDM notches.

Notch	Length, L (mm)	Depth, D (mm)	Opening, W (mm)
A	2.84	1.11	0.1
B	1.62	0.63	0.1
C	0.81	0.31	0.1

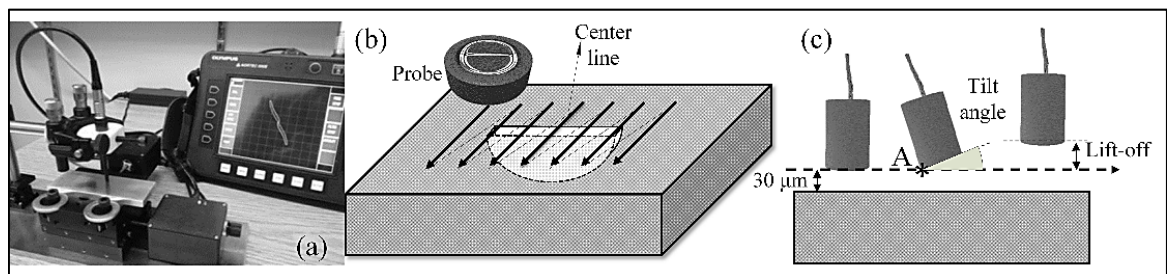


Figure 3.2 (a) Setup for measuring the probe's impedance as it scans the notches, (b) direction of the raster scan relative to the notch length, and (c) representation of the lift-off distance and tilt angle applied to the probe

For the purpose of modelling, the three dimensional (3D) CAD model of the probe is generated and imported into Comsol Multiphysics®. The model is cut in half along its symmetry plane which is parallel to the scan direction. Dimensions of the probe geometry, which are presented in detail previously (Mohseni et al., 2016), are extracted from X-ray tomography reconstruction. The X-ray scans are carried out using a Nikon XTH 225 micro

focus tomography unit and the reconstructed model is post processed via VG studio MAX. A schematic of the cut in half 3D rendering of the stack of the probe's X-ray images is provided in Figure 3.3(a). Besides, the half-scaled 3D CAD model including the assembly of the probe and the sample prepared in Comsol along with a small region of the mesh which is applied to the model are illustrated in Figure 3.3(b). As shown in the figure, in order to shorten the simulation's run time and save resources, a box encapsulating the probe and sample is defined to truncate the solution domain.

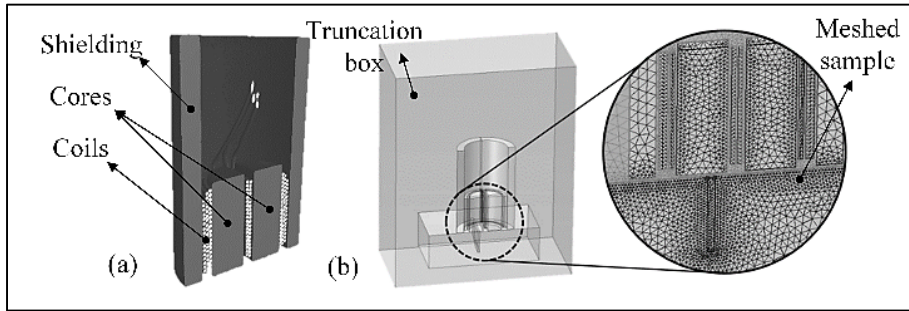


Figure 3.3 (a) Cut in half 3D reconstruction of X-Ray tomography images of the split-D probe, (b) the probe and sample assembly model prepared within Comsol showing a small meshed region in close proximity to the notch geometry

Followed by the assembly preparation, material properties for each domain are defined. Where the relative permeability of 2500 is assigned to the probe cores and the sample's electrical conductivity is considered as 17.8 MS/m. Subsequently, a pre-defined magnetic field physics equation formulated as Equation 3.1 within AC/DC module of Comsol is employed and the magnetic insulation boundaries are placed on the faces of the truncation box.

$$(\nabla \times (\nabla \times \mathbf{A})) / \mu + (j\sigma\omega - \omega^2 \epsilon) \mathbf{A} = \mathbf{J}_e, \quad j = \sqrt{-1} \quad (3.1)$$

In Equation 3.1,  $\mathbf{A}$  is the electromagnetic vector potential,  $\mathbf{J}_e$  is the externally applied current density,  $\epsilon_0$  and  $\epsilon_r$  stand for the electrical permittivity of the free space and relative

electrical permittivity, respectively,  $\mu_0$  and  $\mu_r$  are the permeability of the free space and the relative permeability, respectively. In addition,  $\sigma$  and  $\omega$  are the electrical conductivity and angular frequency. In order to mesh the problem geometry, second order tetrahedral elements are used for each domain. The mesh global size within each domain is adjusted considering the constraints dictated by geometry of each domain and it is locally refined for regions where a high concentration of eddy currents is expected. Therefore, the maximum element size is set to be 0.08 mm on the surface of the sample. The size value is almost half the standard penetration depth of eddy currents ( $\delta$ ) in aluminium at the frequency of 500 kHz. Following that, a small element growth rate of 1.1 is assigned to the sample volume. In this manner, the size of elements across the first few mesh layers under the surface remains below 0.09 mm. Similarly, as depicted in Figure 3.3(b), a locally finer mesh is generated along the notch walls where eddy current density is expected to be high due to the flow perturbation caused by the notch. Afterwards, an iterative solver with frequency domain analysis step is used to run simulations. In each simulation, the notch is scanned by the probe having 0.1 mm displacement increments. This is defined as a parametric sweep step within the solver. Noteworthy, in all simulations presented here except those of the probe tilt study, the probe and the notch are both perpendicular to the surface of the sample. Therefore, there is a plane symmetry for the probe's receiver coils and this plane is also parallel to the notch length during the scans. Accordingly, the notch signals are entirely symmetric relative to the impedance plane's origin and because of that, only a half of the scan can be simulated for each notch. In this manner, the scan starts where the probe is centered with the notch and it continues until the notch is completely passed by the probe. Consequently, the probe finishes its scan at the position of 1.3 mm away from the notch center where it is located over the undefective region of the sample. However, in tilt study the probe's full scanning path, which is twice 1.3 mm, is used since the signal is not symmetric anymore. Differential impedance of the probe at each scan position is calculated using Equation 3.2.

$$\Delta Z = (V_{R2} - V_{R1}) / I_D \quad (3.2)$$

where  $V_{R1}$  and  $V_{R2}$  are the voltages induced across the receiver coils 1 and 2, respectively and,  $I_D$  stands for the current flowing in the driver coil.

Simulations presented in the subsequent sections are categorized in the following order:

1. The scan of calibration notches as the probe has lift-offs of 60  $\mu\text{m}$ , 80  $\mu\text{m}$ , 100  $\mu\text{m}$ , 120  $\mu\text{m}$ , and 140  $\mu\text{m}$  are simulated. The model-based signals obtained at lift-offs of 100  $\mu\text{m}$  and 140  $\mu\text{m}$  are compared with measurements to validate the study.
2. The scan of the calibration notches as the probe's tilt angle varies from  $1^\circ$  to  $4^\circ$  with steps of  $1^\circ$  are simulated. The model-based signals obtained at tilt angles of  $2^\circ$  and  $4^\circ$  are compared with measurements to validate the study.
3. The signal of thirty notches possessing different sizes, as presented in Table 3.2, are simulated to establish a size dependent signal archive for ANFIS training.

All the semi-elliptical notches used in these simulations have 0.09 mm of opening.

Table 3.2 Dimensions of semi-elliptical EDM notches used in the simulations.

Notch No.	D*	L**	Notch No.	D	L	Notch No.	D	L	Notch No.	D	L	Notch No.	D	L
1	0.3	0.3	7	0.3	0.45	13	0.3	0.6	19	0.3	0.75	25	0.3	0.9
2	0.5	0.5	8	0.5	0.75	14	0.5	1	20	0.5	1.25	26	0.5	1.5
3	0.7	0.7	9	0.7	1.05	15	0.7	1.4	21	0.7	1.75	27	0.7	2.1
4	0.9	0.9	10	0.9	1.35	16	0.9	1.8	22	0.9	2.25	28	0.9	2.7
5	1.1	1.1	11	1.1	1.65	17	1.1	2.2	23	1.1	2.75	29	1.1	3.3
6	1.3	1.3	12	1.3	1.95	18	1.3	2.6	24	1.3	3.25	30	1.3	3.9
* Depth in millimetres														
** Length in millimetres														

### 3.2.1 Lift-off and tilt studies

The results of FEM simulations for the probe's lift-offs of 100  $\mu\text{m}$  and 140  $\mu\text{m}$  when it scans the three calibration notches of Table 3.1 are plotted along with the impedance measurements carried out under the same conditions in Figure 3.4.

The nature of the small discrepancies that could be observed between the simulations and measurements results in Figure 3.4 vary depending on the notch dimensions. These differences can be categorized into three classes:

- The difference in maximum signal amplitude that can be mainly observed for the signals of notch A as demonstrated in Figure 3.4(a). This type of discrepancy is believed to be caused by one point calibration which is used for adjusting the initial lift-off of the probe. Depending on the initial spot chosen for lift-off calibration, the actual probe's lift-off might slightly alter as the probe scans locations apart from the calibration point due to the possible non-parallelism of the sample's top and bottom surfaces as well as surface waviness. It shall be noted that all three notches are located at a certain distance from each other on the same sample and changing the scan spot can affect the lift-off of the probe.
- The shape discrepancy between the simulated and measured signals is mostly present for the smaller notches B and C as can be noticed in Figure 3.4(b) and Figure 3.4(c). This difference type is most likely associated to the deviations of the actual notch geometry from the ideal one used in simulations. This kind of difference is more visible for notches B and C as compared to notch A since their signature on impedance plane is smaller and more complex. In addition, the EDM manufacturing method that used to carve these notches reaches its limitations for the small sized B and C notches and hence, the likelihood of deviation from the nominal geometry becomes higher.

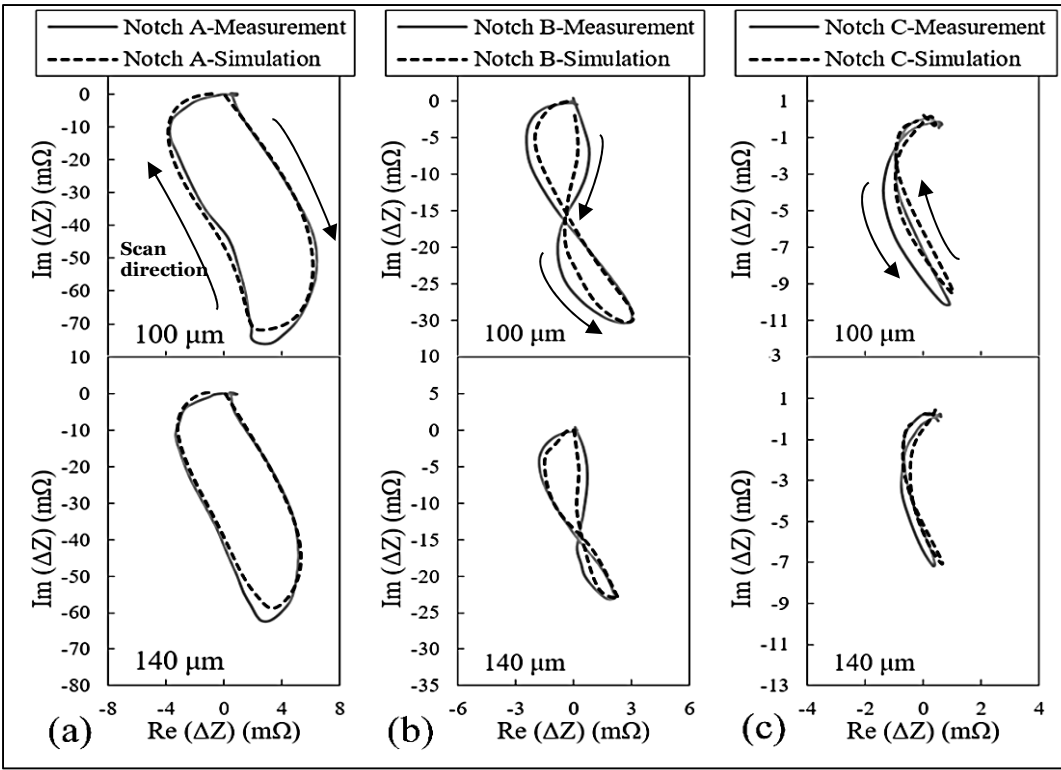


Figure 3.4 Comparison between the measured and simulated signals of (a) notch A, (b) notch B, and (c) notch C at two different lift-offs of 100 and 140  $\mu\text{m}$

- The impedance plane's origin for simulated signal slightly shifts relative to the one from measurement for notch C according to Figure 3.4(c). This difference mostly comes to sight for the smallest notch for which a high device gain is used during the measurements. This effect is connected to the nulling procedure used in simulations where the impedance of the probe scanning the defective parts of the sample is subtracted from the probe's impedance when it is located on undefective parts. Depending on the mesh inhomogeneity in sample, the impedance may not be correctly nulled. Besides, the measured signal is not essentially passing the origin of impedance plane as there is a slight unbalance between the shape of the probe's cores (Mohseni et al., 2016). The difference might as well be present for the larger notches however, owing to their higher signal amplitudes, the origin shift is negligible relative to the size of the impedance trajectory.

Despite of these discrepancies, the predictions made by simulations are reasonably good and the model can be used further to study the signal variations as the lift-off changes. Consequently, for each notch, three more scans at probe's lift-offs of 60  $\mu\text{m}$ , 80  $\mu\text{m}$  and 120  $\mu\text{m}$  are simulated and resulting signals along with the previous ones as the lift-off varies are presented in Figure 3.5.

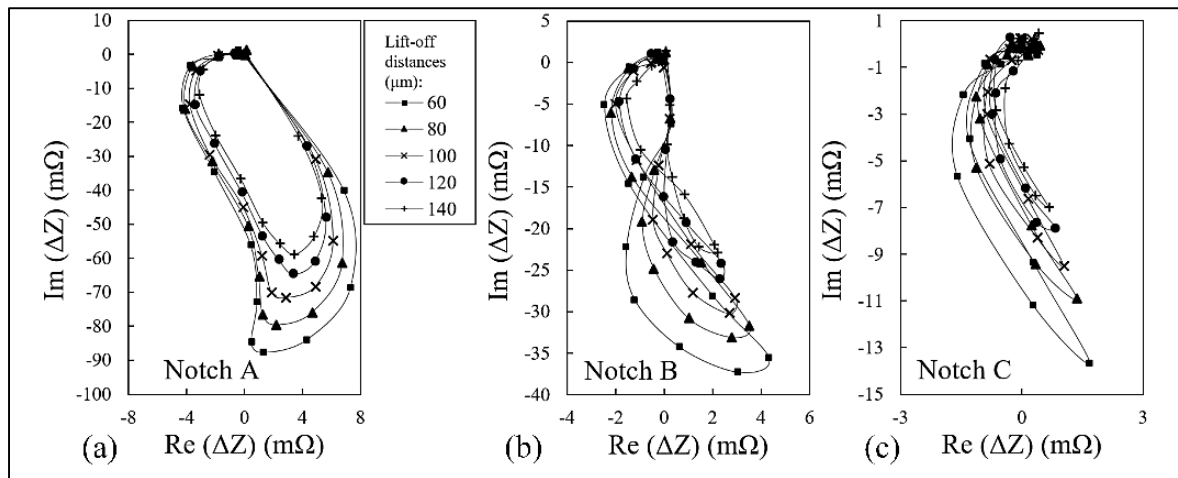


Figure 3.5 Effect of lift-off variations on the ECT signal of (a) notch A, (b) notch B, and (c) notch C

The previously presented validation strategy for lift-off variations is employed again to assess the performance of Comsol in tilt modelling. Therefore, the three calibration notches are scanned with the probe having tilt angles of  $2^\circ$  and  $4^\circ$ . Subsequently, as illustrated in Figure 3.6, the simulated signals are plotted alongside the probe's measurements for comparison purposes.

The slight discrepancies between the signals presented in Figure 3.6 are originated from the same sources that are listed previously with regard to the validation of the lift-off study. The influence of these estimation errors on the signal features that are used for ANFIS training is trivial and thus, the predictions are sufficiently satisfactory serving that purpose. For this reason, additional tilt angles of  $1^\circ$  and  $3^\circ$  are also simulated. The signal variations as the tilt angle varies from  $1^\circ$  to  $4^\circ$  with steps of  $1^\circ$  are depicted in Figure 3.7.

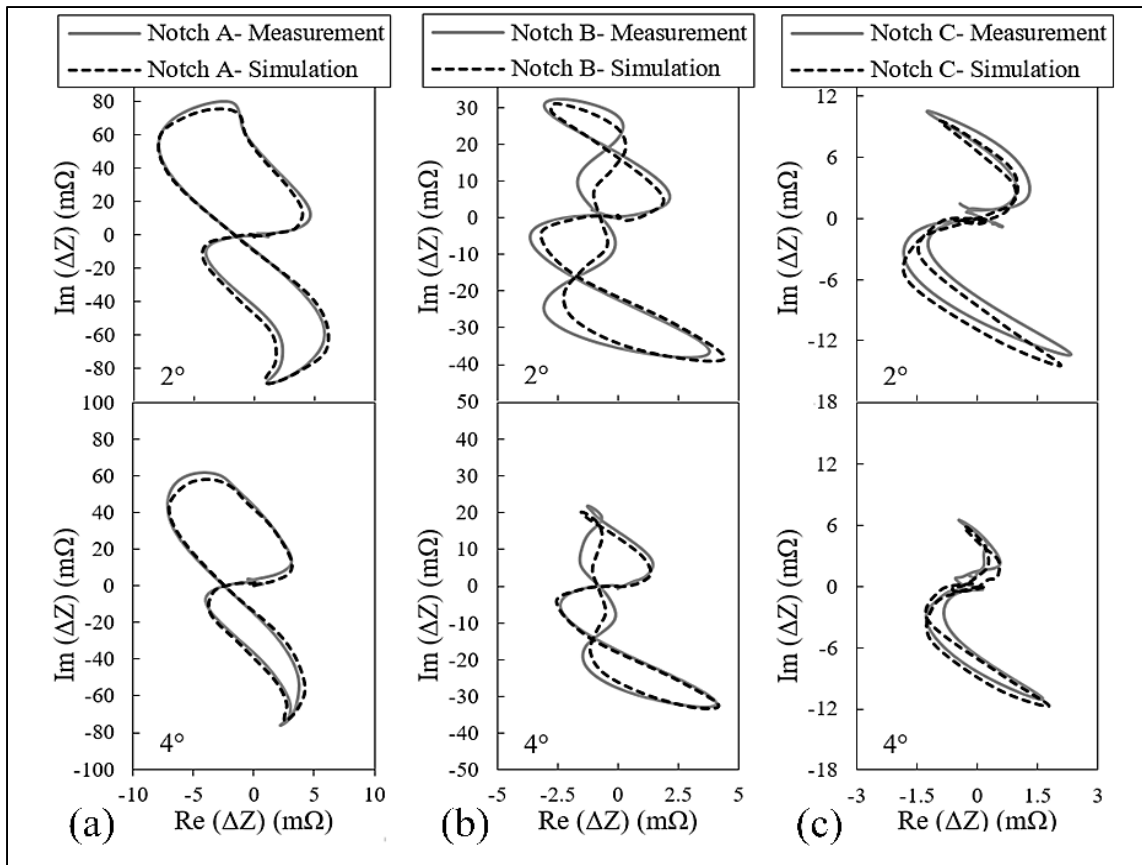


Figure 3.6 Comparison between the measured and simulated signals of (a) notch A, (b) notch B, and (c) notch C for two probe tilts of 2° and 4°

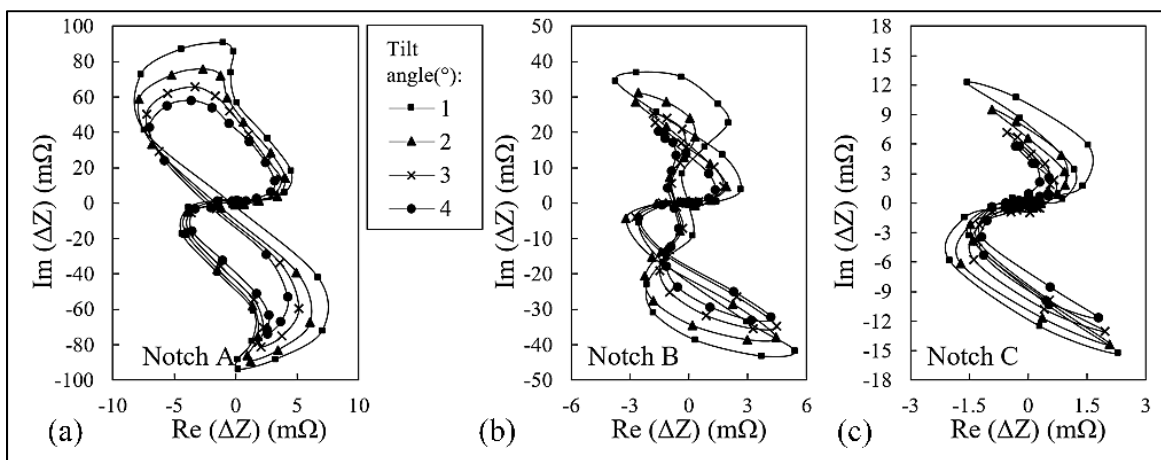


Figure 3.7 Effect of the probe's tilt angle variations on the signal of (a) notch A, (b) notch B, and (c) notch C

According to Figure 3.5 and Figure 3.7, the maximum signal amplitude of each notch decreases as either the lift-off distance or tilt angle grows whereas the signal phase changes are insignificant. Variations of the signal amplitude versus the lift-off distance and tilt angle are plotted in Figure 3.8(a) and Figure 3.8(b), respectively. In these figures, it can be observed that the probe's signal amplitude variations are the largest when it scans notch A as either lift-off or tilt varies. As the notch gets smaller, the variations of amplitude reduce. This phenomenon is directly connected to the notch size. In fact, notch A with a depth almost equal to  $7\delta$  is counted as a broad barrier to eddy current flow. Therefore, this notch perturbs a high percentage of eddy currents regardless of the density imposed by either the lift-off distance or the tilt angle. Accordingly, increasing the lift-off/tilt reduces the absolute value of the signal amplitude remarkably for this notch. As for the smallest notch C, possessing a depth equivalent to  $2\delta$ , the interaction with eddy currents is less as compared to the previous case of notch A. Meaning that eddy currents partially flow beneath the notch. Thus, as a result of weaker interaction between the notch and eddy currents, the signal amplitude is much smaller and hence, the variations of the amplitude caused by the lift-off/tilt changes is limited to the changes of EC density in depth of  $2\delta$ . So, a minor amplitude variation is observed for notch C as compared to the larger notches. However, plotting the normalized amplitude variations, as shown in Figure 3.12, would prove that the amplitude of the smallest notch has higher sensitivity to these lift-off/tilt variations. Clearly, the behavior of amplitude variations for notch B falls in between the other two.

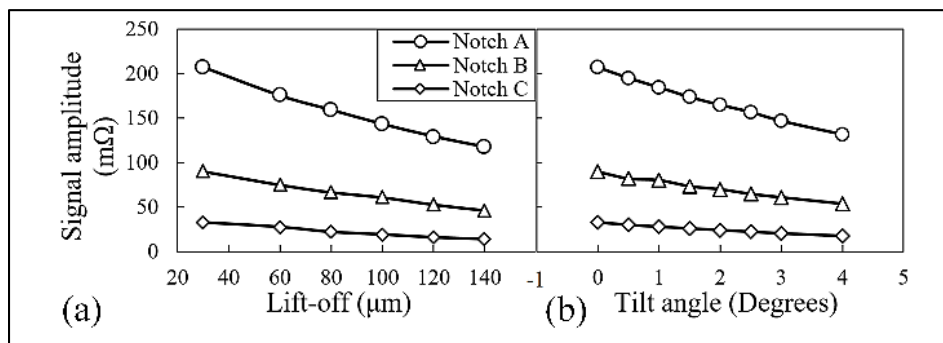


Figure 3.8 Variations of the probe's signal amplitude as it scans three notches A, B and C versus the probe's (a) lift-off, and (b) tilt angle

### 3.2.2 Size dependent signals for ANFIS training

The agreement between the signals obtained by simulations with those of measurements when the probe has its initial lift-off and does not have any tilt angle is previously verified for three calibration notches providing a proof on the versatility of the model in predicting the signals of notches having different sizes as well as the consistency of the outcomes (Mohseni et al., 2016). Accordingly, the model is used henceforth to simulate the scan of thirty notches presented in Table 3.2. Simulated signals of the notches numbered 13 to 18 are presented in Figure 3.9(a). As it can be seen, apart from the variations of the signal phase and amplitude, the signals can be classified into three distinctive shape classes which can be correlated to the ratio of the notch length to the probe's diameter. These three types can be discriminated by the number of the loops that appears in impedance trajectory. A schematic of these three types are presented in Figure 3.9(b). As depicted for type 1, the half-scaled trajectory made by the movement of impedance loci forms only one loop as the probe scans a notch until it reaches the notch center. Both the 2 and 3 type half-scaled signals have two loops however, for the type 2 signal, the magnitude of vector  $\mathbf{X}$  connecting the impedance plane's origin to the point at which the curve intercepts itself is larger than 20% of the vector  $\mathbf{Z}$  magnitude (i.e. the half of the peak to peak signal amplitude). Beside other parameters, the type classification presented here is used as a training input for ANFIS in the next chapter.

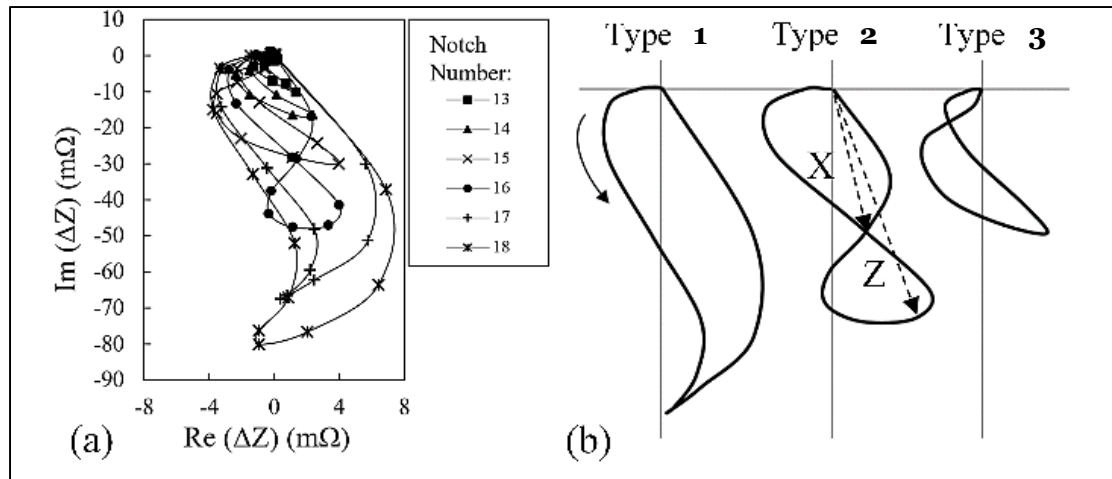


Figure 3.9 (a) Variations of the form of the probe's signal as it scans 6 different notches with different dimensions and (b) three signal shape categories used for training ANFIS

### 3.3 Adaptive neuro-fuzzy inference system

A grid type ANFIS with an initial three inputs/single output Sugeno FIS is used in training. The set of inputs/output data used for this system is listed in Table 3.3. In Figure 3.10(a), the signal features used as inputs to ANFIS are marked on one of the simulated signals. Noteworthy, on each signal, the point at which the signal amplitude becomes maximum is determined and connected by a line  $Z$  to the plane's origin. Afterwards, the hypothetical lines perpendicular to the line  $Z$  that intercept the impedance trajectory at two points are considered and the distance between the two points on each of these hypothetical lines is measured. Accordingly, the maximum distance is taken as the signal width. These features are calculated using a MATLAB script for all thirty signals.

Table 3.3 Set of inputs and output that are used in the form of a vector to train a grid type ANFIS.

Inputs			Output
Amplitude ( $\Omega$ )	Maximum width ( $\Omega$ )	Type (1, 2 and 3)	Notch length (mm)

The architecture of a grid type ANFIS having three inputs and a single output is presented in Figure 3.10(b). The demonstrated system is comprised of five layers where in layer one fuzzification happens meaning that, the membership value of the input is determined through fuzzy sets and the membership function defined for each input. In second layer, an AND operation representing the fuzzy rule is performed at each node providing an output derived from the algebraic product of the membership values of the previous layer. In third layer, each output of layer 2 is divided by the sum of all outputs for the purpose of normalizing and in layer 4, each normalized value from previous layer is multiplied by the sum of inputs having adjustable coefficients. Last layer yields the final output by performing summation on the outputs of layer 4. As it can be seen in Table 3.2, the simulated signals used for training the ANFIS are mostly dependent on the notch length since none of these notches share the same length. Accordingly, the system is trained by having the notch length as output. In Table 3.2, it can be observed that from one column to the other, the notch depth does not change while the length varies. In spite of the fact that their depth is analogous, their signal and hence, extracted features vary since the notch lengths change. Therefore, training the system with depth as an output results in inconsistency in learning which leads to unreliable depth sizing. In other words, the table of signals prepared in this study is primarily generated for notch length estimation and it is not fit for training a depth estimation system.

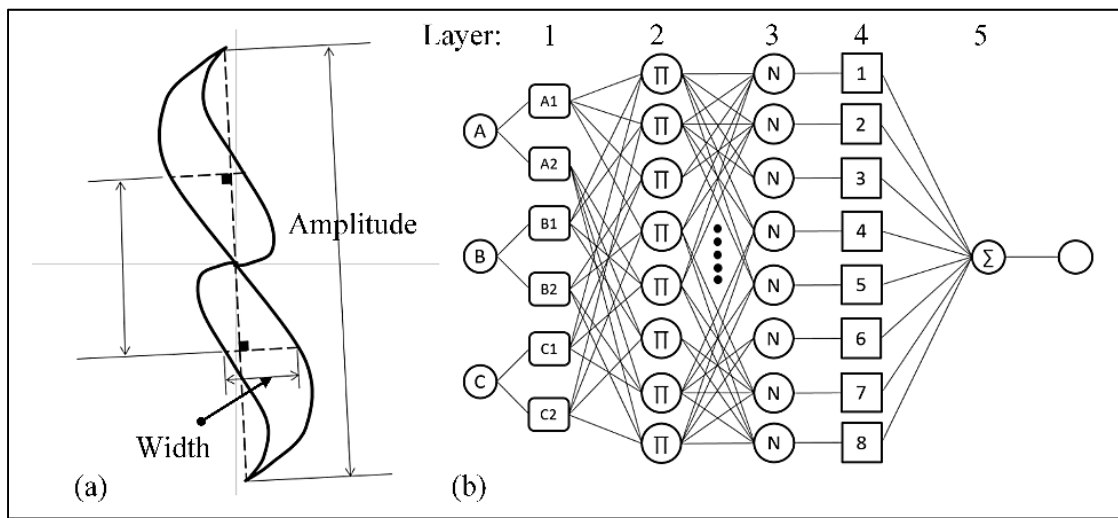


Figure 3.10 (a) Maximum signal amplitude and width shown on a simulated signal of notch A and (b) structure of a three inputs/single output ANFIS (Jang et al., 1997)

Three Gaussian curve membership functions are assigned to each of the FIS inputs. In addition, the system's output is taken constant and weight average defuzzification method is used to obtain the final output. Afterwards, the designed FIS is imported to ANFIS and trained by means of the thirty inputs/output vectors in the form of the one presented in Table 3.3. Each of these vectors is associated to one of the notches listed in Table 3.2. The structure of the resulting system has 256 fuzzy rules. The error generated during the training of the system is 2%. This error corresponds to the difference between the outputs fed to ANFIS and the predictions of the trained system for the given inputs. Performance of the system is also tested by measuring the error in length estimation for the three calibration notches as well as 5 extra notches modelled in Comsol. To this end, the features for both measured and simulated signals are inserted into the trained FIS. Accordingly, Table 3.4 enlists the both actual and estimated lengths of aforementioned test notches for which the length estimation error is also presented. The average error in length estimation of the test notches does not exceed 5%.

Table 3.4 Nominal length and the length estimated by the trained FIS for 3 calibration and 5 model-based EDM notches.

<b>Notch Name</b>	<b>Nominal Length (mm)</b>	<b>Estimated Length(mm)</b>	<b>Error (%)</b>	<b>Notch Name</b>	<b>Nominal Length (mm)</b>	<b>Estimated Length (mm)</b>	<b>Error (%)</b>
Notch A	2.84	2.86	0.70	Test 2	1.35	1.48	9.63
Notch B	1.62	1.68	3.70	Test 3	1.85	2.01	8.65
Notch C	0.81	0.83	2.47	Test 4	2.50	2.61	4.40
Test 1	1.20	1.29	7.50	Test 5	3.00	3.03	1.00

In the second phase of the study, the error introduced in length estimation caused by small variations of the probe's tilt and lift-off are examined for the longest and the shortest calibration notches. Their signals as the probe's lift-off and tilt change are previously depicted in Figure 3.5 and Figure 3.7, respectively. These signals are processed to extract their features which are subsequently fed into the trained FIS. Accordingly, the additional

error in length estimation caused by tilt and lift-off variations are acquired and plotted in Figure 3.11. According to this figure, the error connected to the length estimation made by FIS grows for both notches A and C as either the lift-off or the tilt angle of the probe increases. Moreover, the error associated to notch C grows with a higher rate as compared to notch A. To understand the phenomenon supporting the fact, it would be beneficial to plot the normalized signal amplitudes versus the lift-off and tilt variations for the three calibration notches, as depicted in Figure 3.12(a) and Figure 3.12(b), respectively.

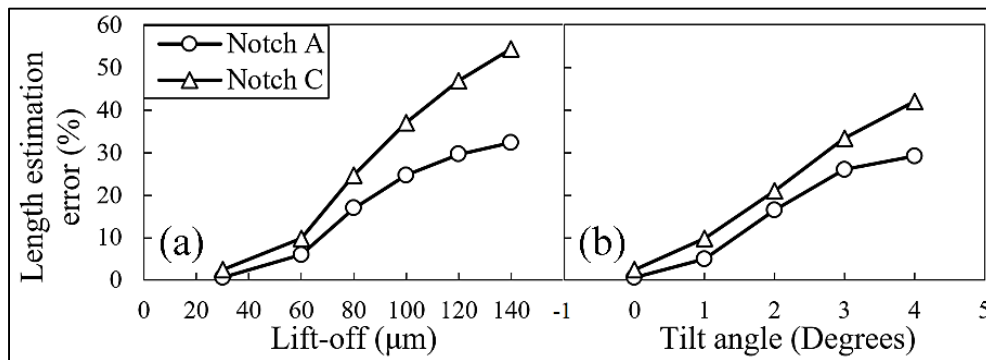


Figure 3.11 Percentage of additional error introduced into the length estimation of notch A and C because of the probe's (a) lift-off and (b) tilt angle variations

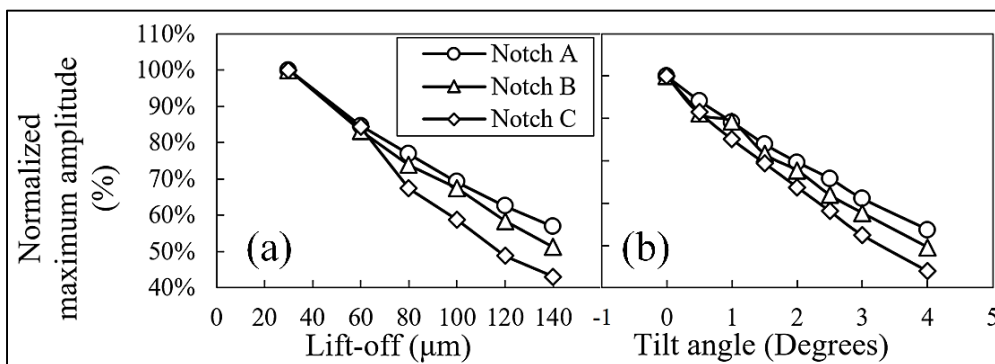


Figure 3.12 Variations of the normalized maximum amplitude of three notches A, B and C as the probe's (a) lift-off and (b) tilt angle change

For the plots of Figure 3.12, the maximum signal amplitude obtained for each notch is normalized by the maximum amplitude of the same notch at the lowest lift-off /tilt value.

Looking at this figure, it is clear that the sensitivity of the signal amplitude to both lift-off and tilt increases as the notch gets smaller yielding the highest sensitivity for the smallest notch C. Since, the interaction of this notch with eddy currents is less significant as compared to the case of notch A, it has a smaller signal amplitude. Besides, the notch is shallower than the first standard penetration depth meaning that it interacts with high density current flow. Considering these two facts, it would be evident that the smallest changes in the lift-off/tilt which in turn changes the eddy current density can have a more significant impact on the normalized amplitude of the smaller notches. In Figure 3.12, the rate of changes in the maximum signal amplitude of notch C, which is an input to the trained FIS, is higher than the notch A versus tilt/lift-off variations and hence, the error introduced into sizing would increase more rapidly. Furthermore, looking at each of the curves plotted in Figure 3.11 individually, it can be seen that there exists a turning point on each curve dividing it to two zones. Before the turning points the sizing error grows faster while the growth rate diminishes as the point is passed. One could expect these observations concerning the error curves since according to eddy current principles, the density of induced currents changes remarkably as the probe is lifted within very low lift-off distances. On the other hand, the variations in current density becomes less sensitive to lift-off changes when the probe is more distant from the sample and the coupling is weaker.

### **3.4 Conclusions**

According to the results presented in the preceding sections concerning the effect of the probe's tilt and lift-off on eddy current signal of the notch as well as the ANFIS training and testing of the trained FIS the following results can be concluded:

- Based on the validation studies carried out here, Comsol is proved to be a reliable FEM tool in predicting the behavior of eddy current signal variations as the probe's lift-off distance and tilt angle varies. The maximum signal amplitude decreases as either the lift-off or tilt increases since the coupling between the probe and the test piece weakens. These amplitude variations are greater for the largest notch A and it becomes less significant as the notch gets smaller. However, the plot of the

normalized impedance versus lift-off/tilt shows that the sensitivity of the normalized impedance to the changes of lift-off/tilt increases as the notch gets smaller.

- The size dependent table of the signals defined in this study is designed to provide ANFIS training data for length estimation. This table is comprised of thirty notches having different lengths. Obviously, the depth diversity of the notches modelled here is not sufficient to provide an efficient training for depth estimation.
- The trained FIS could estimate the length of the test notches with an average error of less than 5%, where 2% of this error is attributed to the system's inherent training error. The length estimation error for the measured signals of the calibration notches A, B and C stays less than 2.5% proving that the system can be used effectively to perform length estimation regardless of the length to depth ratio for semi-elliptical notches in this material.
- It is observed that by increasing the probe's lift-off/tilt the system underestimates the length of the calibration notches. Moreover, the growth rate in length estimation error as the lift-off/tilt increases is lower at the beginning, and it intensifies as the lift-off/tilt increases. This growth rate drops at higher lift-off distances and tilt angles. In addition, the rate of the variations for the length estimation error is the highest for the smallest notch C since its signal demonstrates to be the most sensitive to the lift-off/tilt changes.

### **Acknowledgments**

The present research is conducted as a part of MANU418 which is a project defined by Consortium de Recherche et d'Innovation en Aérospatiale au Québec (CRIAQ). The authors are grateful for the supports provided by Natural Sciences and Engineering Research Council of Canada (NSERC) and industrial partners: CNRC Aerospace, Pratt & Whitney Canada, and L-3 Communications. Authors would like to acknowledge the CMC Microsystems for their help in providing an easy access to Comsol Multiphysics.

## CHAPTER 4

### A RELIABILITY STUDY ON AUTOMATED AND MANUAL EDDY CURRENT TESTING

Ehsan Mohseni<sup>a</sup>, Hamid Habibzadeh Boukani<sup>b</sup>, Demartonne Ramos França<sup>c</sup>, Martin Viens<sup>a</sup>

<sup>a</sup> Department of Mechanical Engineering, École de technologie supérieure (ÉTS),  
Montréal (Québec), H3C 1K3, Canada

<sup>b</sup> Zetec Inc. Québec (Québec), G1N 2C9, Canada

<sup>c</sup> John Abbott College, Montréal (Québec), H9X 3L9 Canada

Paper submitted to the Journal of Nondestructive Evaluation, July 2018

#### **Abstract**

Applying life estimation approaches to determine in-service life of structures and plan the inspection schedules accordingly are becoming acceptable safety design procedures in aerospace. However, these design systems shall be fed with reliable parameters related to material properties, loading conditions and defect characteristics. In this context, the role of non-destructive testing (NDT) reliability is of high importance in detecting and sizing defects. Eddy current test (ECT) is an electromagnetic NDT method frequently used to inspect tiny surface fatigue cracks in sensitive industries. Owing to the new advances in robotic technologies, there is a trend to integrate the ECT into automated systems to perform NDT inspections more efficiently. In fact, ECT can be effectively automated as to increase the coverage, repeatability and scanning speed. The reliability of ECT scanning, however, should be thoroughly investigated and compared to conventional modes of applications to obtain a better understanding of the advantages and shortcomings related to this technique. In this contribution, a series of manual and automated ECT tests are carried out on a set of samples using a split-D reflection differential surface probe. The study investigates the level of noise recorded in each technique and discuss its dependency on different parameters, such as surface roughness and frequency. Afterwards, a description of the effect of crack orientation on ECT signal amplitude is provided through experimental tests and finite element simulations. Finally, the reliability of each ECT technique is investigated by means

of probability of detection (POD) curves. POD parameters are then extracted and compared to examine the effect of scanning index, frequency and automation on detection reliability.

#### **4.1 Introduction**

Fatigue failure is the most important source of damage in systems subjected to cyclic loads. In the aerospace industry, this phenomenon is frequently observed as the dynamic nature of stresses during flight, takeoff and landing promotes the nucleation of micro-cracks and their propagation. In order to make decisions on the continuation of operation and also on the maintenance intervals, risk assessment programs have been introduced (Ghiocel & Wang, 2004). In this framework, probabilistic physical models are used to estimate the remaining fatigue life of in-service components. These models are mostly developed based on the damage tolerance approach, which requires several input parameters including flaw characteristics, material properties and loading conditions (Dillström & Nilsson, 2007). Optimal definition of these input parameters considering their uncertainty would lead to more accurate remaining life estimation; thus, the maintenance intervals would be set based on more realistic results, and unexpected failure could be avoided (Bagaviev & Ulbrich, 2004). Concerning the flaw characterization, NDT methods are the most available and practical means. The uncertainty of flaw characterization is largely influenced by the NDT method, inspection device, test conditions, component under test and inspector (Olin & Meeker, 1996). To address this issue, the reliability and capability of NDT methods in flaw characterization should be properly assessed. Probability of detection (POD) has been developed as a measure to quantify such reliability. Based on POD results it would be possible to make a better decision about the largest flaw which may be missed by a given NDT method (Annis, 2009). Beside POD as the main reliability parameter, probability of false indication (POFI) could also be investigated in the context of NDT reliability. Most of the programmed inspection plans employ POD curves along with POFI as an advantageous means to determine the inspection intervals in some critical safety fields, in particular aerospace industries (Carboni & Cantini, 2015; Georgiou, 2007). It is always of high importance to select the NDT technique and related equipment objectively to efficiently

detect flaws within structures. The appropriate selection of technique and inspection apparatus as well as the test parameters can increase the POD and assure the integrity and reliability of the in-service component over its expected life time (Volker, Dijkstra, Terpstra, Heerings, & Lont, 2004).

Considering its simplicity of operation and effectiveness, eddy current testing (ECT) is one of the NDT methods widely used for detecting and sizing fatigue cracks in the aerospace industry (Boller, 2001). ECT, which is based on electromagnetic principles, is one of the preferred methods for the inspection of surface discontinuities in electrically conducting materials (Cecco et al., 1983). Since the nucleation sites for fatigue cracks are mainly located on the surface and near surface areas of materials, reflection differential split-D ECT probes can be a good option for the detection of such cracks. The placement of D-shaped receiver coils in the housing and their differential configuration provide a small footprint and high signal to noise ratio. This could be translated into high detection sensitivity for surface cracks, reducing undesirable noises caused by the probe's lift-off and tilt (Mohseni et al., 2016; R. Mooers et al., 2012). The advantages of using this type of probe configuration become more pronounced when inspecting ferromagnetic materials (*e.g.*, martensitic steels), since the ECT signals detected from these materials could be very noisy. Different studies have investigated the performance of split-D probes through model-based approaches (R. Mooers et al., 2012; R. D. Mooers, Aldrin, & Knopp, 2015a; R. D. Mooers et al., 2015b; R. D. Mooers et al., 2013, 2014; Norio Nakagawa et al., 2009), while some others have tried to perform model-based inversion based on the flaws scanned by the probes (J. C. Aldrin et al., 2015; J. C. Aldrin et al., 2014; Shell et al., 2014).

Knowing that ECT is often used in the modern aerospace industry, where the quality of the inspection method plays a critical role in the public safety, it is crucial to investigate the reliability of the ECT method through POD studies. Like any other NDT technique, ECT signals are always accompanied with variability in tests that could impact the POD (Rajesh, 1997). Therefore, POD studies on ECT have become increasingly important in recent years. Rosell et al. presented a comparative study on automated and manual scans of surface cracks

using an absolute ECT probe (Rosell & Persson, 2013). Moreover, a series of studies regarding POD of ECT inspections of bolt-hole were conducted by Krause et al. (Lemire et al., 2009; Lemire et al., 2010; P. R. Underhill & T. W. Krause, 2011). They generated PODs based on the inspection results for fatigue cracks and EDM (electrical discharge machined) notches located in bolt holes of bi-layer 7075-T6 aluminum sheets. Their inspections were performed using rotary split-D ECT probes, and the effect of different calibration schemes, such as two-point calibration, on the obtained POD were investigated.

The present research aims to investigate, for the first time, the reliability of both manual and automated (encoded) scans for detecting surface fatigue cracks in a set of flat AISI 410 steel samples using a split-D probe. To this end, the signal response POD is considered as the quantitative tool for this comparison study, where only the most influential parameters (*i.e.* parameters that their variation affects the ECT signal significantly), namely the test frequency, the crack orientation, the index of automated raster scan and the inspector are considered. The methods used herein for POD data analysis are in accordance with the MIL Handbook 1823A standards (Annis, 2009) and are using the mh1823 POD algorithms package, which is available online (Annis, 2018). Even though this study does not cover all the usual round robin of test parameters, the small matrix of laboratory tests conducted herein shows to be fairly conclusive as a comparative study.

During the analysis of the signal amplitude as a function of the relative orientation between the scan and crack lines, it is observed that for each specific orientation there is a threshold crack length above which the changes of eddy current signal amplitude become less than 5%. Hence, one could speculate that the signal amplitude is becoming almost insensitive to the crack length. Unfortunately, the crack length interval used in the experiments is limited. In order to expand the extent of this study to larger crack sizes, and thus gain a better insight into the experimental observation, finite element modelling (FEM) is employed. For this purpose, a FEM is prepared for a split-D probe interacting with samples containing semi-elliptical notches representative of fatigue cracks. Subsequently, the effect of notch length and orientation on the signal amplitude is analysed through FEM simulations.

The paper structure is organized in the following manner. The variables treated as the source of variability in ECT response for both automated and manual ECT scans are presented in section 4.2. Section 4.3 provides the details of experimental procedures and calibration system. In section 4.4, noise analysis for each technique is presented, and the dependency of the noise on different test parameters is investigated. The effect of crack orientation on the signal amplitude is studied experimentally and numerically in sections 4.5 and 4.6. The reliability studies concerning both techniques through POD curves are discussed in section 4.7 and the study is concluded in section 4.8.

## **4.2 ECT POD variables**

Obtaining variable responses by repeated inspection of a flaw with a fixed size is a proof of a lack of reproducibility for a given NDT technique. Scanning responses depend on many factors including the material properties, characteristics of the flaw, equipment set-up, inspector skills and environmental factors. Accordingly, for a specific flaw size, a distribution of signal amplitudes could be obtained, which could be used further to generate a POD curve using statistical analysis.

An intuitive insight into the parameters affecting signals must be achieved when generating a POD curve for a certain ECT application. Special care should be taken to include the influential parameters while insignificant ones could sometimes be neglected. Table 4.1 lists several parameters that may contribute to the flaw response variability (Rosell & Persson, 2013).

Table 4.1 List of parameters causing variations in ECT signals during automated and hand scans

Hand scans	Automated tests
Inspector	Index and speed of scan
Squaring collar	Vibrations and associated noise
Environmental conditions	
Calibration	
ECT equipment and probe	
Test frequency	
Gain and electrical noise	
Probe orientation (differential probe)	
Probe's tilt and lift off	
Sample's surface conditions (curvatures, roughness and contaminations)	
Material properties (conductivity and permeability)	
Crack geometry (shape, opening, profile, length and depth) and orientation	
Signal acquisition and feature extraction for POD analysis	

Even though some of the parameters presented in Table 4.1, such as material properties and environmental conditions, may contribute to POD results, their contribution is negligible compared to some influential ones and might not be included in a POD study. Since the same ECT instrument and probe are used in both manual and automated scans, they are discarded as a possible source of variation in this study. During the tests, the probe is positioned randomly on the sample's surface leading to possible variations in the relative angle that the scan direction makes with the orientation of milling tool marks on the surface. Although effort is put in keeping the perpendicularity of the probe relative to the surface, small tilt angles may still remain. The small tilt variations along with the effect of tool marks orientation are considered as contribution to lift-off. The speed of automated scans is significantly low relative to the data acquisition sampling rate; therefore, the effect of scanning speed is disregarded. In view of these assumptions, the list of the remaining influencing factors is summarized in Table 4.2.

Table 4.2 List of parameters examined in this work for monitoring their effect on the distribution of ECT response

Hand scans	Automated tests
Inspector	Scanning index
Test frequency	
Crack orientation	

### 4.3 Experimental procedure

The specimens used in this study were provided by an aircraft engine manufacturing company. They are made of martensitic AISI 410 steel with a 114.3 mm × 25.4 mm × 6.35 mm dimensions. Pristine samples were mixed with others containing artificially induced fatigue cracks. Specimens are machined from three steel plates. Fatigue cracks are grown out of a small starter EDM notch using cyclically loaded three-point bending tests. Cracks are grown to predetermined lengths to cover a useful range. Then, the top and bottom surfaces of the samples are machined off so that the starter notches and fixture marks are removed. Destructive tests performed on a subset of these samples revealed that the depth ( $D$ ) of fatigue cracks is correlated to their length ( $L$ ) through the linear regression given in Equation 4.1 with a coefficient of determination  $R^2 = 0.984$ .

$$D = -0.006 + 0.347 L \quad (4.1)$$

A Nortec 500S eddy current device along with a reflection split-D differential surface probe with a frequency band in the range of 500 kHz to 3 MHz are selected for the inspections. The experimental tests are performed in two separate stages: a) first, all samples including defective and undefective are inspected manually; b) second, an automated raster scan is conducted on the entire set of samples. In both stages, horizontal and vertical gains of the Nortec device are fine tuned to fit the largest captured signal within 80 percent of both screen height and width at each test frequency. Accordingly, the response of the largest fatigue crack included in the study (2.95 mm in length and 1 mm in depth) is used for calibration

purpose. To do so, this crack is scanned in several passes perpendicular to its length and only the maximum response is kept for gain settings. Such an approach has been suggested by Krause et al. (Lemire et al., 2010) because longer cracks would decrease the variability resulting from different inspectors. Besides, the signal obtained from these cracks is higher in amplitude giving rise to the best available signal to noise ratio.

Manual ECT scans are performed by three qualified inspectors. During the manual scans, a bell-shaped squaring collar is attached to the probe to maintain the perpendicularity of the differential probe to the sample's surface. In addition, a Teflon tape with thickness of 50  $\mu\text{m}$  is used on the probe's tip. This helps to reduce the friction between the probe and the scanning surface, making it easier for the probe to glide over the surface during the inspection process.

For automated scanning, a motorized X-Y table is utilized to perform a raster scan on the samples. The ECT probe is clamped inside an alignment holder, allowing gimbal and swivel micrometric rotation about the axis of a mounting post. The lift-off is controlled through a micrometric Z-stage and set at 30  $\mu\text{m}$  to avoid friction between the probe's tip and the sample's surface, thus preventing the probe from flexing. The experimental setup for the automated scans is shown in Figure 4.1. Before starting each scan, the probe is positioned arbitrarily on the sample's surface to randomize the relative position of the probe and cracks, if there is any. Subsequently, three scans with indexes of 2.5 mm, 1.25 mm and 0.5 mm are conducted for each sample while keeping the same probe position at the start of the scan.



Figure 4.1 Experimental setup for performing automated ECT scans

A solvent cleaner is applied on the sample's surface before starting the inspections to remove any potential contamination. All samples are tested at three test frequencies of 500 kHz, 750 kHz and 1 MHz, and orientation angles of  $0^\circ$ ,  $45^\circ$  and  $90^\circ$  (refer to  $\theta$  in Figure 4.2(a)). The signals captured by the Nortec 500S device are recorded and transferred to a computer through a data acquisition card for further processing. The 8-shape impedance trajectories are plotted from the recorded data of horizontal and vertical axes, and then are post-processed in MATLAB to find the peak-to-peak amplitude values for all indications (refer to  $V_{pp}$  in Figure 4.2(b)).

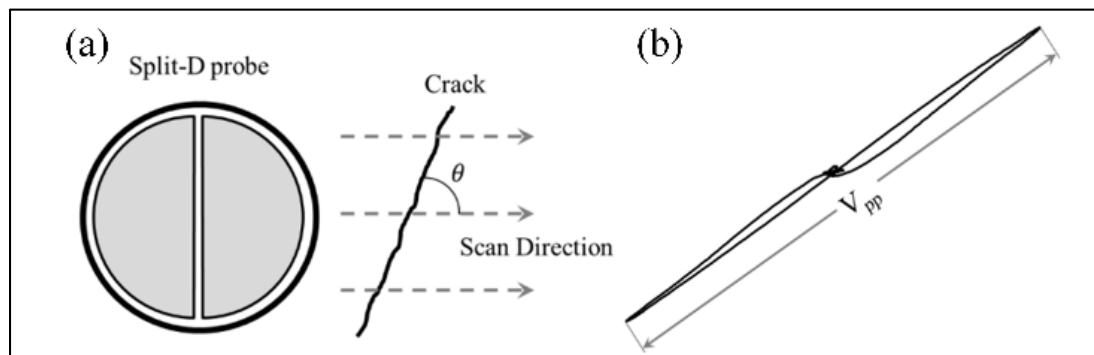


Figure 4.2 (a) relative orientation represented by the angle  $\theta$ , which is defined by the crack line and scan direction, and (b) peak-to-peak amplitude of an 8-shape ECT signal

#### 4.4 Noise Treatment

As mentioned in Section 4.2, sample surface conditions, such as roughness, contribute to ECT noise. In addition, for manual scanning, surface roughness may induce probe wobble and vibration due to improper handling and pressure variation during scan. For automated scanning, undesired effect, such as non-parallelism between the sample surface and the scan plan, is another contributor to noise. There is finally a fundamental noise coming from electrical circuitry.

Electrical noise has first been measured by nulling the Nortec device while the probe was held in the air. The signal acquired thereafter has been processed in MATLAB® to calculate the root mean square (RMS) variation of the probe impedance,  $Z_{rms}$ . Such a calculation is based on Equation 4.2 where  $X(t)$  and  $R(t)$  are respectively the inductive reactance and the resistance of the probe as a function of time. It has later been observed that less than 10 % of the noise level recorded during the scans is attributed to electrical noise.

$$Z(t) = \sqrt{X(t)^2 + R(t)^2}, \quad Z_{rms} = \sqrt{\frac{1}{(t_2 - t_1)} \int_{t_1}^{t_2} [Z(t)]^2 dt} \quad (4.2)$$

To calculate the noise level associated to sample scanning, the signals acquired from undefective samples are imported to MATLAB®. As depicted in Figure 4.3, typical noise signal is interrupted by intervals during which scanning direction is reversed. In order to disregard these intervals, noise samples are taken within windows that exclude these inconsistent signals. A moving average over each of these windows is calculated and subtracted from the sample's response to compensate for the effects of the probe's tilt and lift-off during each pass of the scan. This pre-processing operation is carried out in an attempt to isolate noise due to surface conditions from the one induced by non-ideal probe handling. Afterwards, the RMS impedance is calculated according to Equation 4.2 for each window, and the values of 10 windows are averaged to yield the noise level for one scanning condition.

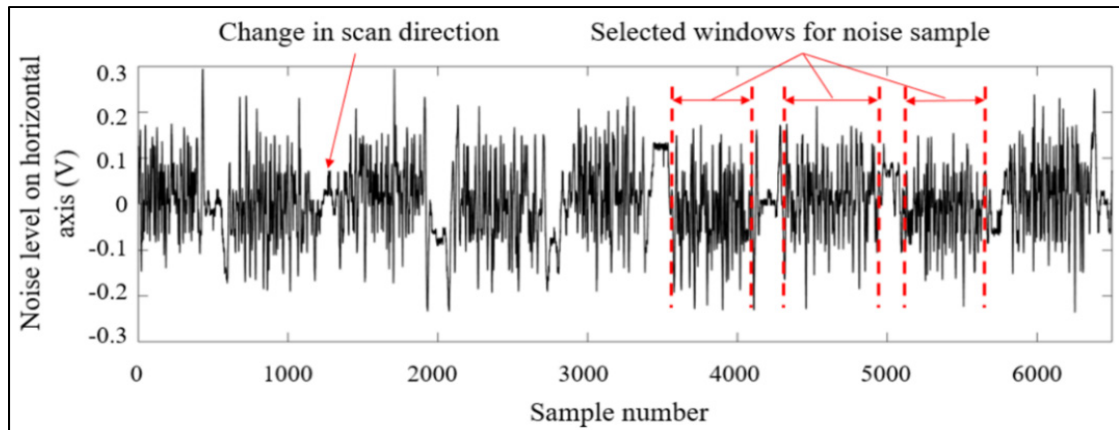


Figure 4.3 Typical noise recorded during manual scan and the windows selected for processing

Because the eddy current device gains differ with operating frequencies and scanning techniques (manual or automated), noise level shall be analysed in accordance with these settings. So, in all cases, noise level has been normalized with respect to the calibration signal amplitude. The noise variations against the orientation of the machining tool marks with respect to scanning direction are plotted in Figure 4.4. From this plot, it can be found that noise of the manual scan shows higher values at all testing conditions as compared to the automated scans. The lift-off introduced by the Teflon tape during manual scans is  $50\ \mu\text{m}$ , which is larger than the one used in automated scans. The higher lift-off distance results in weaker coupling between the probe's electromagnetic field and sample. To compensate for such an effect, gains on each axis should be increased during calibration, and this fact alone elevates the level of noise in manual scans. Moreover, in comparison to automated scans, manual scans are affected by some other sources of noise, including the non-uniformity of hand pressure during the scanning process and fluctuations imposed by the surfaces' irregularities, which raise the overall received noise on the eddy current signal.

Both manual and automated noise levels get larger as the relative angle between the probe and machining tool path direction (*i.e.*, tool marks orientation) increases from  $0^\circ$  to  $90^\circ$ . In the same fashion, the arithmetic mean deviation of the assessed profile ( $R_a$ ) increases as the surface tool marks orientation changes from  $0^\circ$  to  $90^\circ$ , according to Figure 4.5. Therefore, as

we look at the variations of the noise level with the tool marks orientation in Figure 4.4, the trend of variations closely follows the one observed for  $R_a$  against the tool marks orientation in both techniques. However, the noise growth rate of automated scans more accurately resembles the  $R_a$  variation trend. This can be explained by observing that the scan direction relative to the tool marks orientation is more accurate in the automated scan than in the manual. Furthermore, the additional noise superimposed by other sources in manual scans, as mentioned previously, could contribute to the slight deviation of the slope of manual noise variations from that of  $R_a$ .

As another influential parameter, an increase in frequency would also intensify the noise levels in both techniques. Variation of the noise level as the frequency is increased from 500 kHz to 1 MHz seems to be quasi-linear in automated scans, whereas the trend is moderately different in manual scans. As it is observed in Figure 4.4, the noise associated to the manual scan grows relatively faster as the frequency changes from 500 kHz to 750 kHz when compared to the growth rate in the 750 kHz and 1 MHz interval. Since the material under investigation is ferromagnetic, the skin depth of eddy currents at 750 kHz approaches that of the surface's roughness. Therefore, further increase in frequency has a weaker effect on the noise level.

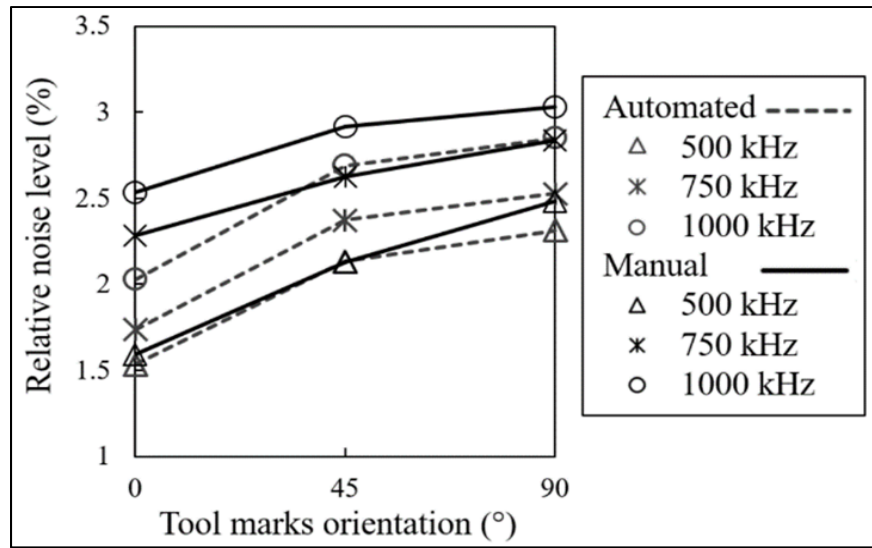


Figure 4.4 Variations of the percentage of noise level normalized by the calibration signal amplitude as angle between the probe scan direction and machining tool marks orientation changes. Results are presented for 3 frequencies for both manual and automated scans

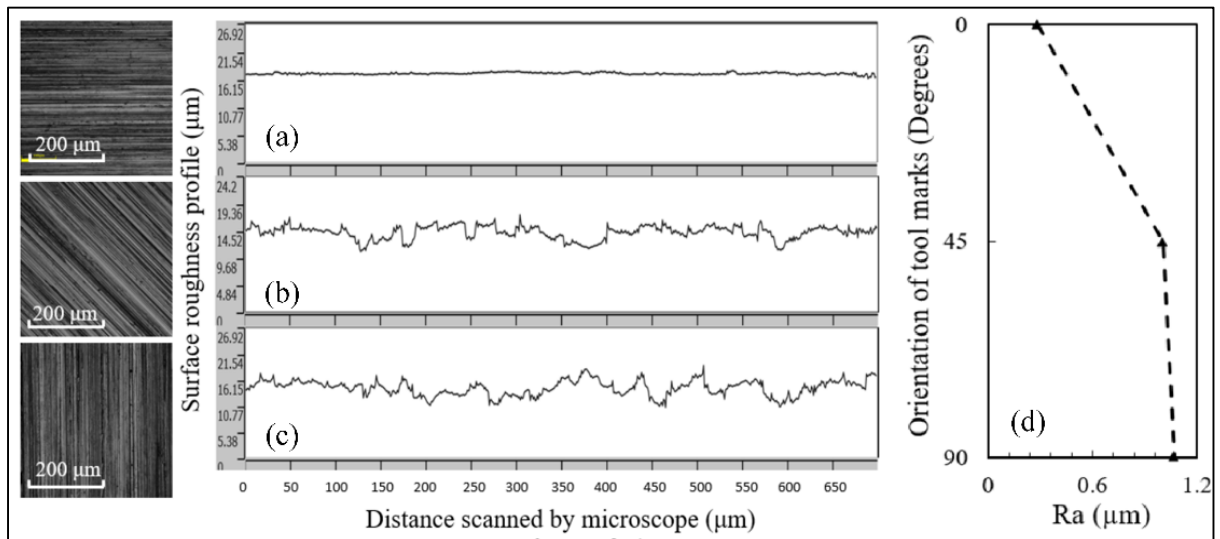


Figure 4.5 Optical laser microscope images and samples of the surface roughness profile for (a) 0°, (b) 45°, and (c) 90° angles that the probe’s scan direction makes with the orientation of tool marks on surface. (d) orientation of tool marks *versus*  $R_a$

#### 4.5 Numerical modeling for orientation study

To investigate the effect of crack orientation on the signal amplitude of the split-D probe, a three-dimensional model for the assembly of split-D probe and sample is prepared in Comsol Multiphysics. The scan of surface notches with different lengths at three orientations of  $0^\circ$ ,  $45^\circ$  and  $90^\circ$  is carried out to simulate the experimental tests. The frequency of 1 MHz is chosen for the model-based study. It shall be noted that in these simulations, fatigue cracks are replaced by semi-elliptical notches as they can fairly represent the shape of fatigue cracks. Also, the tight opening of  $20\ \mu\text{m}$  is considered for the notches to provide a better estimation of fatigue crack signals. According to the notch opening study presented in (Mohseni et al., 2016), however, the maximum signal amplitude becomes less dependent on notch opening as the notch gets larger in dimensions. The models for  $0^\circ$  and  $90^\circ$  orientations are cut in half across the symmetry plane to save simulation run time. On the other hand, the scans with  $45^\circ$  orientation have no symmetry plane, and simulations for this orientation shall be conducted with a full-scaled model. The details regarding the Comsol model for the assembly of the probe and sample along with the selected physics and solvers are discussed in (Mohseni et al., 2016). The mesh is slightly changed as compared to that study, since the material is ferromagnetic and requires a finer boundary layered mesh because of the lower penetration depth of ECs. Therefore, the entire geometry is meshed using second order tetrahedral elements and 8 boundary layers, each having a thickness of  $20\ \mu\text{m}$  starting from the surface of the sample. The thickness of each layer is almost equal to the skin depth of eddy currents in the steel sample. In addition, very fine elements (with the size of almost one standard penetration depth of eddy currents in the sample) are used for meshing the notch walls where a high concentration of eddy currents is expected due to perturbation. The rest of the model is freely meshed by selecting a very low growth rate within the domain volumes.

Before conducting the study, the validity of the model is examined by comparing the simulation results with the experimental test results for two cracks with 2.92 mm and 1.50 mm in length, both oriented at  $0^\circ$  relative to the scan direction. The procedure explained in section 2 (Equations 2.10-2.13) is used to translate the voltage recordings of Nortec to

impedance variations and compare the results of measurements to the ones from simulation. These results are plotted together in Figure 4.6(a) and Figure 4.6(b), respectively. The simulated and experimental signals are quite similar in terms of amplitude levels; however, there is a discrepancy between the shape of the simulated and experimental signals for a 1.5 mm long crack. This could be attributed to the difference between the geometry of the simulated straight notches, which possess parallel side walls, and the zigzag shaped fatigue cracks. Another possible source of error may be that the probe is not scanned over the exact position at which the simulation is carried out. Furthermore, the deviation of the notch opening and profile from the real geometry of a fatigue crack, as small as 1.5 mm in length, can contribute to the signal shape discrepancies as well. It is worthy to note that the important signal feature required for validating our model-based case study is the maximum amplitude, for which the matching between the simulation and experimental results is quite acceptable. Following the model verification, the notch length is varied with incremental steps of 0.5 mm within the size intervals presented in Table 4.3, and the simulations are performed for all the notch sizes listed in the table.

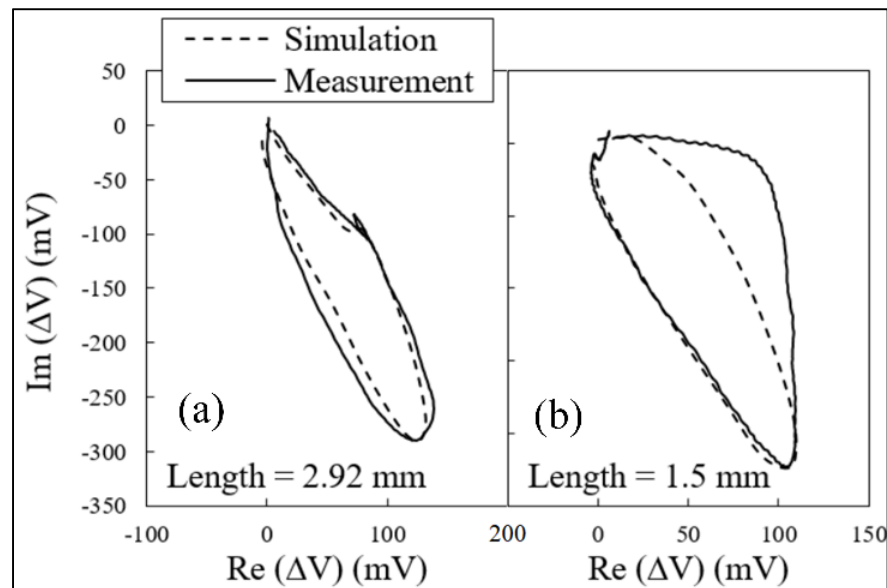


Figure 4.6 Comparison between the measured signal from a crack and simulated signal for a notch for a (a) 2.92 mm and (b) 1.5 mm long crack/notch oriented at  $0^\circ$

Table 4.3 The length interval studied through modelling for each specific orientation

Orientation	Min. Length (mm)	Max. Length (mm)
0°	0.5	3.0
45°	1.5	4.5
90°	2.0	6.0

#### 4.6 Effect of crack orientation on signal amplitude

Signal amplitudes obtained at frequencies of 500 kHz and 1 MHz from automated scans are normalized and plotted versus the crack length to driver coil's diameter ratio ( $L/D$ ) for the three orientations in Figure 4.7. At each crack length, the corresponding signal amplitude is normalized by the signal amplitude of the calibration crack oriented at 90°. According to the results of the 0° orientation, and up to a given  $L/D$ , the signal amplitude increases with the  $L/D$ . However, the amplitude remains almost constant beyond that value. Since such a threshold is dependent of the probe's geometry, it is better to describe this value as a function of  $L/D$ , where the drive coil's diameter is 1.8 mm. Referring back to Figure 4.7, the plateau for 0° starts once the  $L/D$  ratio approaches the unity. For the other two orientations, the existence of that critical value could not be observed in the measurement results, meaning that the normalized amplitude keeps increasing as the  $L/D$  grows. Comparing the two graphs, it can be seen that increasing the frequency to 1MHz would slightly augment the normalized amplitude for each  $L/D$ . In addition, each of these graphs shows that for the  $L/D$  values exceeding the unity, the 90° orientation generates higher signal amplitudes as compared to the other two orientations. A plausible explanation could be that at 90° orientation, the perturbation caused by eddy currents is more severe, and the resulting field distribution as well as the differential impedance are affected more significantly. However, for flaws with  $L/D$  approximately less than unity, the normalized signal amplitude is almost independent of the crack length. This is important in terms of probability of detection, since for flaw sizes lower than the drive coil's diameter, the flaw orientation does not have an influential effect on the probability of detection, whereas the flaw orientation becomes a principal parameter for larger sizes. (This behaviour will be also observed later herein in the distribution of the  $\hat{a}$

vs.  $a$  plot depicted in Figure 4.10(a). In that plot, it is evident that the dispersion of amplitude values for ECT signals recorded for cracks of different orientations is significantly less at crack sizes smaller than 2 mm.)

According to the results shown in Figure 4.7, for each orientation the signal amplitude is associated with some deviations from a smooth correlation with  $L/D$ . Even though the fatigue cracks are produced under controlled conditions, those deviations could be explained by observing that the shape and opening of the cracks might vary, yielding to a certain level of deviation in the amplitude-length correlation.

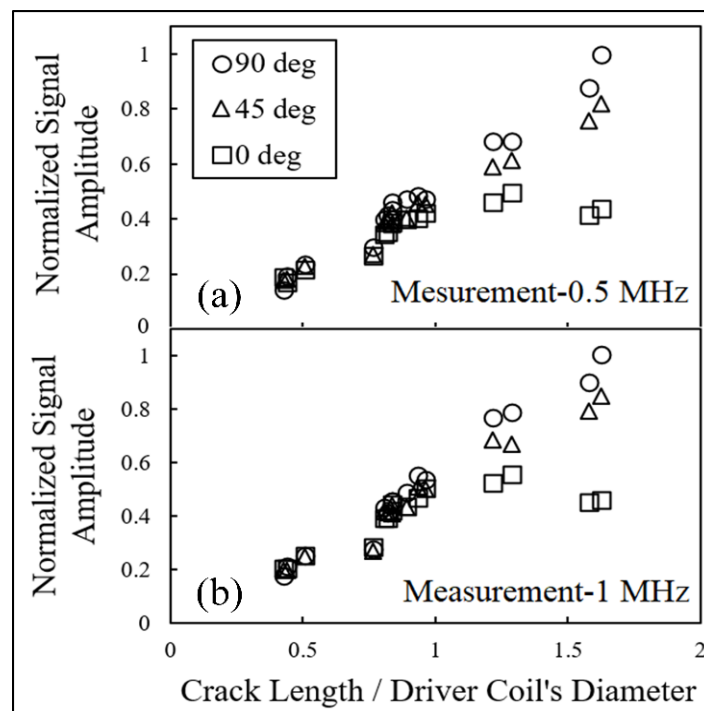


Figure 4.7 Normalized signal amplitudes *versus*  $L/D$  ratio for orientations of  $0^\circ$ ,  $45^\circ$  and  $90^\circ$  at frequencies of (a) 0.5 MHz and (b) 1 MHz

Since the thresholds for the  $45^\circ$  and  $90^\circ$  orientations do not fall within the experimental  $L/D$  intervals presented here, the  $L/D$  ratios beyond these intervals are explored with the aid of FEM simulations. The simulation results are compared (superimposed) with the experimental

measurements, performed at the same frequency, and presented in Figure 4.8. According to this figure, there is also a critical  $L/D$  for each of  $45^\circ$  and  $90^\circ$  orientations, after which the signal amplitude remains almost unchanged. Figure 4.8 shows that the critical  $L/D$  could not be determined for the  $45^\circ$  and  $90^\circ$  orientations by the measurements, since they were conducted on a limited crack length's interval having a maximum  $L/D$  value of 1.62, whereas the simulation results cover larger flaw lengths with a maximum  $L/D$  of 3.33. The threshold  $L/D$  ratios are found to be 1.38 and 1.66 for the orientations of  $45^\circ$  and  $90^\circ$ , respectively. The simulation results also show the same trend as that of the experiments for the  $0^\circ$  orientation. It is noticed that as the orientation angle increases, the normalized amplitudes *versus* the  $L/D$  grow with a higher rate until they reach the threshold  $L/D$  value. All these observations confirm that the orientation has a very significant effect on the signal amplitudes after a given  $L/D$ . Therefore, for cracks with a  $L/D$  ratio higher than unity, the sizing of the crack will be associated with larger errors if the probe does not intercept the crack in a favorable direction.

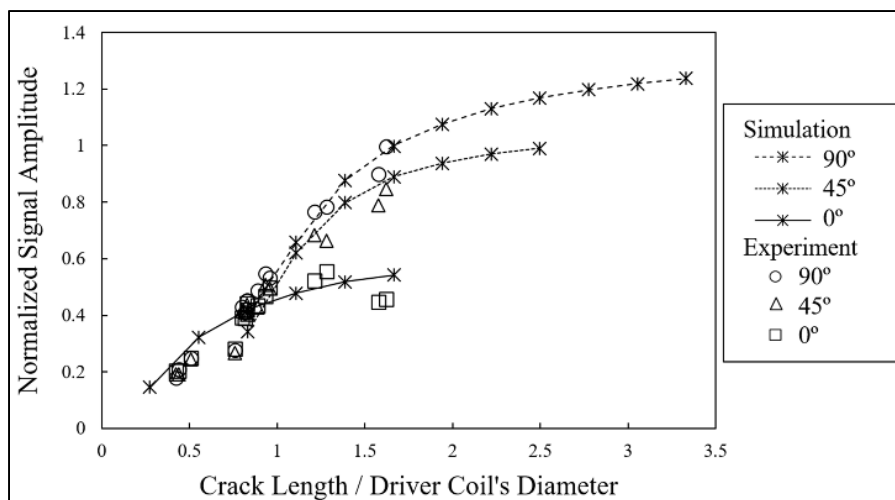


Figure 4.8 Simulated and measured normalized signal amplitudes *versus*  $L/D$  ratio for orientations of  $0^\circ$ ,  $45^\circ$  and  $90^\circ$  at 1 MHz

For the  $90^\circ$  orientation, the distribution of current density on the surface of the steel sample is demonstrated in Figure 4.9(a). As shown in this figure, for a 2 mm notch with  $L/D$  almost equal to unity, the probe's amplitude becomes maximum when the notch is positioned 0.3

mm away from the center axis of the probe. In this situation, the notch disturbs the high density eddy current loops, which are formed adjacent to the driver coil on the surface. Therefore, the concentration of surface currents increases in the extremities of the notch length, since currents flow from sides to bypass it. Figure 4.9(b) demonstrates that further increase of the notch length from 2 mm to 4 mm continues to change the distribution of eddy currents on the surface. Accordingly, the probe's differential impedance increases, as the larger notch acts as a stronger barrier, and perturbs the current flow more significantly. However, when the notch length goes beyond the threshold value of 1.66 for  $L/D$ , as it has already been discussed, the changes in the electromagnetic field distribution (and thus the current density distribution) on the surface become trivial. This can be verified by comparing Figure 4.9(b) and Figure 4.9(c). In fact, it is evident that a change from 4 mm to 6 mm in the notch length results in a very small influence on the surface current density and its distribution. The impact of the notch length on the current density distribution is more pronounced when comparing Figure 4.9(a) and Figure 4.9(b). To explain this, the fact that the probe's impedance is related to the distribution of eddy currents in the sample should be considered. Accordingly, there is not any remarkable impedance changes for crack lengths larger than the threshold  $L/D$  value, since this distribution does not change noticeably. In other words, for notches longer than 3 mm, the flow of eddy currents from the notch sides becomes insignificant. As a result, the contribution of the length to impedance variations fades away, since the preferred path of current flow would be different.

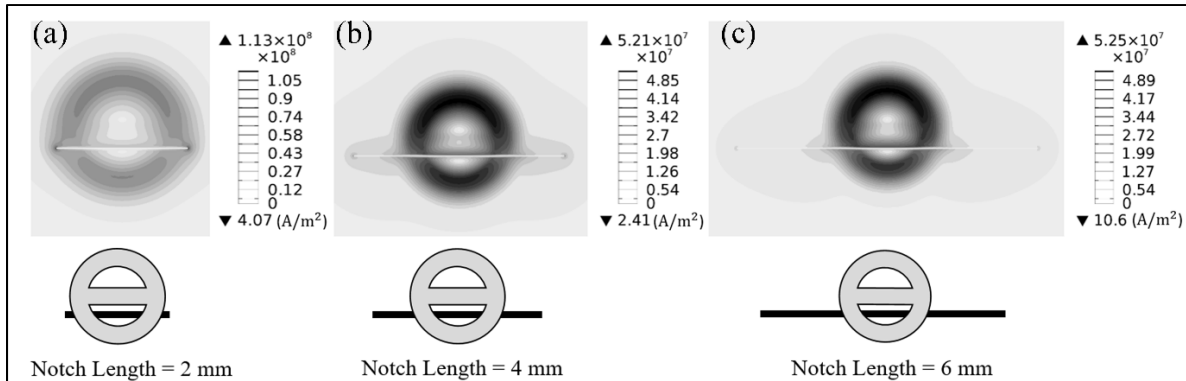


Figure 4.9 Contours of current density norm distribution on the surface of a sample. The probe center is located 0.3 mm away from the notch center. Notches with lengths of (a) 2 mm, (b) 4 mm, and (c) 6 mm are investigated

#### 4.7 POD of automated and manual tests

A signal response POD analysis, according to the procedure provided in MIL-HDBK-1823, is performed on the  $\hat{a}$  vs.  $a$  data acquired from both manual and automated scans (Annis, 2009). As the first step in this analysis, it is observed that a linear relationship can be established between  $\log(\hat{a})$  and  $\log(a)$  as presented in Equation 4.3. In this equation,  $\beta_0$  and  $\beta_1$  are the regression line's coefficients, and  $\gamma$  is the random error, which is assumed to have a normal distribution with a mean value equal to zero. The standard deviation of  $\gamma$  is presented by  $\sigma_\gamma$ . After finding the regression parameters, the POD of size  $a$  can be calculated through Equation 4.4, where  $\Phi$  stands for cumulative log-normal function and  $\hat{a}_{dec}$  is normally determined based on the noise distribution and a POFI value that is required to be achieved (Georgiou, 2007; Nath, Balasubramaniam, Krishnamurthy, & Narayana, 2010).

$$\text{Log}(\hat{a}) = \beta_0 + \beta_1 \text{Log}(a) + \gamma \quad (4.3)$$

$$\text{POD}(a) = \Phi \left\{ \frac{\text{Log}(a) - [\text{Log}(\hat{a}_{dec}) - \beta_0] / \beta_1}{\sigma_\gamma / \beta_1} \right\} \quad (4.4)$$

$\hat{a}_{dec}$  is taken as 30% of the signal amplitude of the calibration crack. Figure 4.10(a) demonstrates the regression line correlating  $\hat{a}$  and  $a$  data, as well as the corresponding POD curve plotted for the scan index of 0.5 mm in automated inspection at 500 kHz.

Figure 4.10(b) and Figure 4.10(c) also present the curves extracted for scan indexes of 1.25 mm and 2.5 mm, respectively. As expected, the comparison between these curves reveals that  $a_{90/95}$  improves as the scan index becomes smaller. Moving from scan index of 2.5 mm towards 1.25 mm,  $a_{90/95}$  improves by 50 %, and this improvement continues by 21% as the index reduces from 1.25 mm to 0.5 mm. This noticeable difference between  $a_{90/95}$  values of 2.5 mm and 1.25 mm scan occurs because any scan index larger than the driver coil's diameter increases the chance of missing cracks. This is the case especially when the crack is oriented  $0^\circ$  with respect to the scan line. As can be seen in the  $\hat{a}$  vs.  $a$  data plot presented in Figure 4.10(c), there are 4 crack sizes at which the crack is missed. On the other hand, in the case of using 1.25 mm scan index, all the cracks are detected based on the results shown in Figure 4.10(b). However, as compared to the index of 0.5 mm, there is a lower probability that the probe passes over the crack center at the index of 1.25 mm; therefore, the recorded signal response at this index can be lower for some crack sizes. It is well known by the ECT practitioners that choosing scan indexes smaller than the probe's diameter improves the detection probability. The observations presented in Figure 4.10 support this idea. Similar results have also been suggested in a POD study presented for automated inspections using an absolute probe (Rosell & Persson, 2013). Automated scans POD parameters acquired at different test frequencies and scan indexes are listed in Table 4.4.

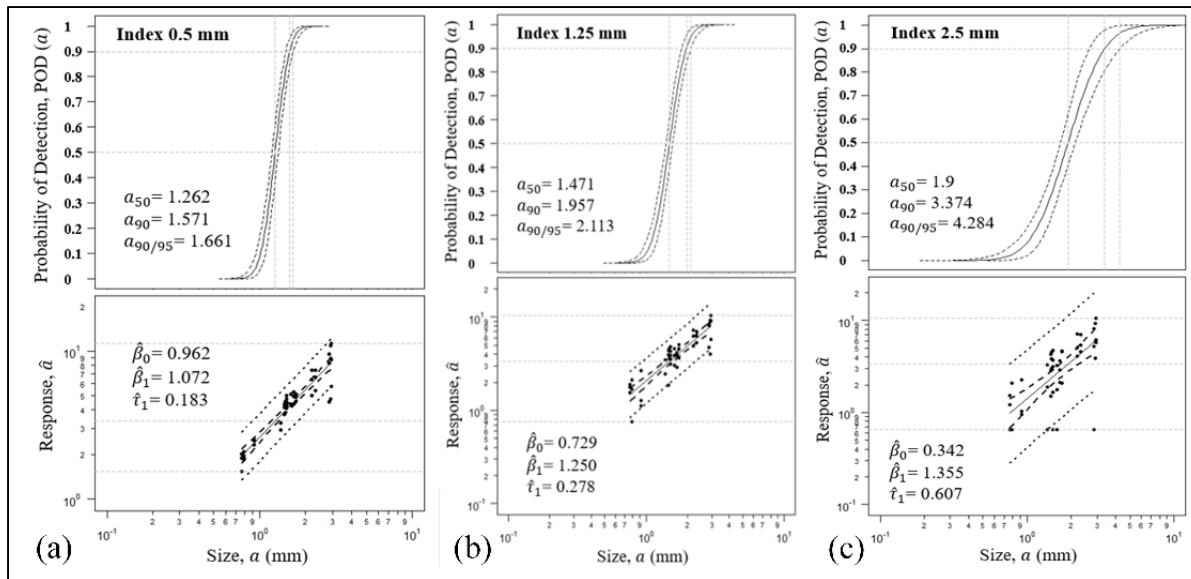


Figure 4.10 Regression lines found for  $\hat{a}$  vs.  $a$  data and related POD curves plotted for automated scans with indexes of (a) 0.5 mm, (b) 1.25 mm and (c) 2.5 mm

Table 4.4 POD parameters for automated scans

Frequency (kHz)	Scan Index (mm)	$a_{50}$ (mm)	$a_{90}$ (mm)	$a_{90/95}$ (mm)
1000	0.50	1.306	1.636	1.732
	1.25	1.510	1.997	2.153
	2.50	1.990	3.630	4.720
750	0.500	1.300	1.616	1.708
	1.25	1.510	1.993	2.147
	2.50	1.900	3.301	4.135
500	0.50	1.262	1.571	1.661
	1.25	1.471	1.957	2.113
	2.50	1.900	3.374	4.284

According to Table 4.4, and regardless of the selected frequency,  $a_{90/95}$  becomes smaller as the scan index is reduced. The table also implies that for scan indexes of 0.5 mm and 1.25

mm, an increase in the test frequency degrades the POD. The increase in the frequency can be advantageous up to a certain level at which the skin depth of eddy currents becomes comparable to the depth of surface features, such as surface roughness and scratches (P. R. Underhill & T. W. Krause, 2011). Beyond that level, signal amplitude does not improve, and using higher frequencies only adds to the level of the noise. In the case of AISI 410, a test frequency of 500 kHz is high enough to concentrate a larger portion of eddy currents flowing within the depth of surface features, since the material is a ferromagnetic martensitic steel with high permeability. Therefore, further increase of frequency improves neither the signal to noise ratio nor the POD. For the scan index of 2.5 mm,  $a_{90/95}$  decreases as the frequency is reduced from 1 MHz to 750 kHz, and it increases subsequently as the frequency is lowered again from 750 kHz to 500 kHz. As stated earlier, at this index the cracks oriented at  $0^\circ$  relative to the scan direction are not always detected, since their detection is strongly dependent on the relative positioning of the probe at the beginning of the scan and the crack. Accordingly, it is wise to not arrive to a conclusion for the effect of frequency on POD based solely on the values found for  $a_{90/95}$  at this scanning index.

Table 4.5 provides the POD parameters for the manual scans performed at three different frequencies. Based on these results, the best POD occurs at 750 kHz, unlike the automated scans. As it can be noticed, at 500 kHz some cracks are missed during manual scans. Accordingly, the POD at this frequency is lower than the one obtained for 750 kHz. However, this is not the case in automated scans, since using the scan index of 0.5 mm provides indications for every defective sample.

Table 4.5 POD parameters concerning the manual scans at different frequencies

<b>Frequency (kHz)</b>	<b><math>a_{50}</math> (mm)</b>	<b><math>a_{90}</math> (mm)</b>	<b><math>a_{90/95}</math> (mm)</b>
1000	1.257	1.638	1.702
750	1.182	1.524	1.581
500	1.261	1.660	1.727

Comparing Table 4.4 and Table 4.5, it is evident that the value of  $a_{90/95}$  for frequencies of 1 MHz and 750 kHz is lower in manual scans, implying in better POD. It is expected that the POD for manual tests is better than the automated counterpart if we assume that all cracks are detected by both techniques. In manual scans, after an indication has been observed, the inspector will try to maximize the response by repeating the scan. However, this is not the case in automated scans, where the signal strength is strongly affected by both the position of the probe on the surface and the scan index. Therefore, the scan trajectory in automated scan can intercept the crack at any point across its length, which may not be necessarily the crack's center. Based on these observations, the signals recorded during automated scans are usually weaker if the selected index is not small enough to get a response from the crack's center. In general, it is safe to assume that the main advantage of automated scans is that no cracks are missed when small scan indexes are used. On the other hand, the signal amplitude obtained for the detected defects is normally larger in manual scans as it is best practice to maximize the response as suggested by ECT inspection procedures.

#### 4.8 Conclusions

- The results of the noise treatment suggest that the level of the manual noise is higher than the automated noise. This may be related to the additional gains used to compensate for the increased probe's lift-off in manual tests. There are also some additional sources of noise which only exist in manual scans, such as variations of hand pressure and the contact between the probe and sample's surface.
- Regardless of the chosen technique, manual or automated, the noise level increases as either the frequency is heightened or the surface roughness is increased. However, the trend of these variations is steeper in manual scans. It is also observed that the variations of the noise (recorded in automated scans) versus the orientation of the tool marks on surface follow the trend of variations of  $R_a$  itself.
- It is found that the signal amplitude of a crack whose size is smaller than the diameter of the driver's coil is independent of the crack's orientation. However, for cracks larger than this threshold, the difference in signal amplitude grows as the length

increases. The amplitude growth rate falls to less than 5 % for each orientation by reaching a certain  $L/D$  value at that orientation. These values are derived from simulated signals to be 1, 1.38 and 1.66 for  $0^\circ$ ,  $45^\circ$ , and  $90^\circ$  crack orientations, respectively.

- POD of automated scans strongly depends on the selected scan index. Decreasing the index to values smaller than the driver coil's diameter improves the POD significantly; however, the effect of further increase would be less significant.
- A lower frequency (*e.g.*, 500 kHz) seems to provide the best POD in automated scans, as the noise captured from the surface features is less than that observed at higher frequencies. On the other hand, the best test frequency in manual scans is 750 kHz, since some cracks are missed when a 500 kHz testing frequency is used.
- In general, manual scans provide better POD results than automated scans. It is believed that the tendency of inspectors to maximize the signals from the detected flaws is the main reason behind this observation. The probe's trajectory in automated scans, even by selecting small indexes, does not always pass through the center of the crack, resulting in lower signal amplitude averages.

### **Acknowledgments**

The authors would like to thank the Natural Sciences and Engineering Research Council of Canada (NSERC) for funding this research. We would like to extend our appreciation to Pratt & Whitney Canada for providing the samples used in the POD demonstration. We are also thankful to CMC Microsystems for facilitating the access to FEM software.



## CONCLUSION

As implied earlier, the objective of using QNDE techniques is to develop a NDE system that can reliably detect and size the potential flaws in structures. Therefore, Chapters 2 and 3 aimed at providing a model-based strategy to size surface defects using the ECT method. Moreover, the reliability of the NDE system was assessed in Chapter 4. The following provides the contributions and conclusions of each of these chapters in summary.

In chapter 2, it is tried to develop a very basic FEM, based on the governing electromagnetic field PDEs, in order to model the interaction between the electromagnetic field of a simplified surface absolute coil and a surface rectangular notch. Through the model, which is intended to be used as a basis to model construction for more complex probe geometries, the scan of the surface EDM is simulated and the probe's impedance changes as a function of the scan position are obtained. The results of the modelling effort for the absolute probe are compared to the Burke's benchmark study to ensure the model's validity. The second part of the chapter aimed at modelling of a split-D surface probe and calculation of its differential impedance variations for scanning through width notches of different depths carved in an aluminum 7075-T6 sample. The simulation outcomes are accompanied with the impedance measurements of the actual probe scanning EDMs for validation and calibration of the model. The followings presents the conclusions drawn from the first study on modelling of ECT absolute and split-D differential probes using FEM:

- A good agreement is observed between the experimental measurements and the outcomes of the initial model, which is prepared for the assembly of an absolute coil and EDM. The absolute probe's model, designed based on the study of Burke, firstly proves that the COMSOL Multiphysics® version 5 could be used as a reliable FEM tool to simulate low/medium frequency electromagnetics. Secondly, it shows the consistency of the impedance estimations when certain parameters are set correctly in the model.
- Beside the geometry and material properties of the elements, which are inherent and should be determined as accurate as possible for model inputs, the effect of different

modelling parameters such as truncation boundaries, surrounding air properties and mesh distribution is investigated. It is observed that truncating the problem's geometry to an extent that encompasses  $A$  field down to thousandth of its maximum amplitude provides reasonable estimation of the electromagnetic field calculation at the selected frequency. The air conductivity cannot be zero in COMSOL magnetic field interface solver and should have a small positive value. The parametric sweep of this value demonstrates that the impedance readings become stable for values superior to 0.1 S/m. It is conservative to have at least six mesh layers across the first three standard penetration depths however, depending on the notch and probe's geometry, assigning one layer of mesh to each penetration depth could also provide reliable results if computation resources are limited.

- To determine the boundaries of the problem for modelling of the split-D probe the same strategy used for the FEM of absolute probe can be effectively applied. The number of mesh layers required on the surface also follows the same rule. Mesh non-uniformities in undefective areas give rise to instability of differential impedance of the split-D probe passing over these regions since the probe compares the readings of two adjacent coils. Accordingly, a mirrored structured mesh is defined for undefective regions captured within the first few standard penetration depths. In this manner, while the probe is centered with the notch, the differential impedance is equal to zero. Alike the former model, air conductivity of 0.1 S/m shows to be a promising value for the case of split-D model.
- The model impedance predictions closely follow the impedance measurements of the split-D probe. The peaks of the imaginary part estimated by model always fall within the measurement error however, as the notch depth decreases a small discrepancy appears between the real part of impedance estimated by model and the one from measurement. The shape agreement between the signal obtained by simulation and measurement is fair although the measured figures possess a smaller width as compared to simulated ones. The sources that could contribute to these discrepancies are the deviation of the actual EDM geometry from the ideal one used, unbalance of the D-cores and coils as well as the faulty positioning of the coil assembly in housing,

and inaccuracies of the material properties used as model inputs. In general, experimentally measured signal amplitudes are predicted by the numerical results for accuracies of more than 97%.

In pursue of the flaw-sizing objective and as an evolution to the modelling approach investigated in chapter 2, the model is completed further and put to test for the study of semi-elliptical surface EDM in chapter 3. In this chapter, bearing the experience of previous simulations, a model of the split-D probe scanning three semi-elliptical notches having different sizes is prepared. The model's impedance predictions are compared to the result of experiments to verify its reliability. Once it is found acceptable, the sensitivity of the signal to probe's tilt and lift-off, as common sources of error affecting the ECT signal in actual inspections, is explored during performing scans. The calibrated model is also used to establish a size dependent signal table covering a certain notch length size interval. Moreover, an adaptive network designed based on a fuzzy Sugeno inference system is trained using the signal table to carry out length estimations. This study including the modelling approach, sensitivity of ECT signal to tilt and lift-off, training of soft computing algorithm using model-based signals for notch length estimation suggests the following conclusions:

- The signals obtained from three EDM notches have three distinct signatures depending on the probe's diameter to notch length ratio. For notch lengths larger than the diameter of the driver coil, there is one distinctive loop in the half-scaled 8-shaped signal. However, as the length reaches the diameter of the driver coil a second loop emerges. For very small notch lengths as compared to the driver coil's diameter, the signal reshapes again to one loop where the direction of forming the loop is apposite to the first one stated here as the probe scans over the notch (Mohseni et al., 2016).
- The impedance trajectories acquired by experiments at different lift-off values slightly deviate from the predictions of the model. These discrepancies are classified in three groups, each originated by a different source. As reported, the first one is the difference in maximum signal amplitude, which can be mainly observed for the signals of the largest notch and it is attributed to one point calibration of the lift-off. The second one is perceived as shape discrepancy between the signals. It is mostly

present for the smaller notches B and C where the cause is mainly connected to the erroneous notch fabrication. The third type is concerning the impedance plane's origin shift, which mostly comes to sight for the smallest notch for which a high device gain is used. This defect reflects the imperfection of nulling approach applied to simulations.

- The amplitude of the signal decreases as the lift-off and tilt increase. Clearly, these variations are larger for the largest notch since the surface impeding the eddy current flow is larger and therefore, small changes in eddy current density caused by lift-off/tilt are reflected as vast amplitude changes in signal. These amplitude changes as a function of lift-off/tilt reduce for smaller notch size. The variations in the signal phase caused by tilt and lift-off are mostly visible for the largest notch since eddy currents interact with this notch wall across several penetration depths.
- The ANFIS network trained by the model-based ECT signals provides good length estimations the actual surface EDMs as well as the modelled ones. The estimation error in predicting the length of EDMs is below 4% while in length estimation for model-based notches, this error increases to a maximum of 10%. In general, considering that the average error remains below 5%, the trained network demonstrates an acceptable performance.
- Increasing the lift-off distance and tilt angle of the probe during the scans of surface notches result in larger errors in length estimation provided by the trained ANFIS. The error introduced into sizing versus lift-off/tilt has the form of a logistic function.
- The degree of the sensitivity of the signal amplitude to lift-off/tilt variations grows as the notch size decreases. This can be mainly explained by the ratio of the notch depth to the standard penetration depth of eddy currents. The lower this ratio, the higher the sensitivity of the notch signal to the changes of eddy currents' density as well as lift-off/tilt variations.

Investigating the reliability of a selected NDE procedure is as critical as developing models for sizing in the framework of QNDE. Therefore, in chapter 4 of this dissertation, a series of manual and automated scans are performed on a number of flawed/unflawed martensitic

AISI 410 stainless steel samples. Based on a prior experience, a number of parameters are indicated as influential. Therefore, the variation of these parameters in a controlled manner and their attribution to signal response variations, in both manual and automated scans, are captured in a POD study. Furthermore, the recorded automated/manual noise is processed to conceive its dependency on the test frequency and the orientation of surface roughness. In addition, a model-based study is conducted to investigate the effect of defect orientation in these materials on the signal response of a split-D probe. Finally, the POD curves for the automated and manual scans are compared to get a better insight into the capability of each procedure. The following can be presented as the conclusions of the study:

- After investigating the level of noise related to each of the manual and automated scans, it is observed that regardless of chosen test frequency and orientation of surface roughness, the noise level in manual scan always exceeds the levels of the noise in automated counterpart. The difference is explainable by the higher calibration gain used in the manual scans to compensate the increased effect of lift-off relative to automated scans. There are also additional sources in manual scans, including the uneven hand pressure and non-parallelism between the scan plane and the sample's surface, contributing to the noise.
- Noise level in both scan techniques increases as either the surface roughness orientation or the test frequency is increased. The slope of these variations is steeper for manual scans. The trend of variations of the noise, as the orientation of surface roughness is changed from  $0^\circ$  to  $90^\circ$  angle, is identical to the trend observed for  $R_a$  *versus* orientation.
- In crack orientation study, it is found that the variations of the signal amplitude *versus* the crack length get as small as 5 % when a threshold L/D value is reached at each crack orientation. The L/D value is found to be 1, 1.38 and 1.66 for  $0^\circ$ ,  $45^\circ$ , and  $90^\circ$  crack orientations, respectively; by aid of experimental tests and numerical simulations. The investigations also show that the signal amplitude is independent of the crack length when L/D ratio is smaller than unity.
- The extracted PODs for automated scans supports the idea of using a scan index smaller than the diameter of the driver coil. It is observed that the  $a_{90/95}$  reduces as the

scan index is decreases from 2.5 mm to 0.5 mm. The study also suggests that a better POD can be achieved in automated scans at the lowest frequency of 500 kHz.

- In general, manual scans provide better POD results than automated scans. It is believed that the tendency of inspectors to maximize the signals from the detected flaws is the main reason behind this observation. The probe's trajectory in automated scans, even by selecting small indexes, does not always pass through the center of the crack, resulting in lower signal amplitude averages.

## RECOMMENDATIONS

Previous approaches, which provide a comprehensive strategy for modelling and model-based sizing of detected defects, are mainly presented based on volume integral method for ECT using split-D probes. However, owing to recent progresses in computing hardware and resources, FEM dominates the current ECT modelling efforts as a highly flexible modelling tool. Since the modelling tool is newly applied to ECT procedures, the modelling of more advanced ECT probes such as split-D probes used for different purposes should be further investigated for validation and calibration. Although the current study partly covers the use of such probes in a specific application to size surface defects in a certain material, some details regarding the defect model as well as the capacity of the inversion approach is still to be investigated. The following summarize some unexplored aspects of the present study, which seek the attention of future works:

- This work mainly concentrates on using EDM notches as representative of fatigue surface cracks. However, the comparison between the signals of these two is beyond the scope of the thesis. In order to make a transition in modelling of EDMs and inversion of their signals toward actual industrial inspection of fatigue cracks, one should conduct a study to optimize the parameters of the notch to best estimate the signal of cracks of the same size. In fact, this would serve as a calibration study taking into account the effect of notch parameters such as width, profile and the conductivity bridges between its walls in modelling to reproduce the signal of a fatigue crack of the same length and depth.
- We experienced some difficulty in characterizing the internal probe's constituents and their properties. As suggested by experience, it would be beneficial to design and build a costume ECT probe for the purpose of model validation since this promotes the accuracy of model inputs and thus, provides a more rigorous validation.
- The model presented here simulates the ECT signal of the split-D probe moving over the notch passing from its centerline. In other words, the probe inspects a single line centered to the notch length, which is not always the case in actual testing conditions. This simplifying assumption is made here since the concern of authors is mainly

focused on automated scans in which it is feasible to find the notch centerline for impedance recordings and accordingly, sizing. However, to build a more thorough and reliable sizing algorithm the impedance variations should be simulated across several scan lines of a certain index over the defect geometry. The additional impedance data, acquired from different positions of the probe relative to defect, compliment the training data sets and enhances the sizing accuracy.

- In order to add to the maturity of the inversion algorithm to derive additional defect parameters such as depth, defect's tilt angle and orientation, impedance values linked to a full scan over the notch should be obtained through modelling. This fact could result in lengthy simulation runs. As a remedy to such difficulty, a surrogate model interpolating the impedance data from limited scans of specific defect sizes, angles and orientations could be established to form a cost effective forward model. It should also be noted that by increasing the output parameters of the network, a Mamdani type fuzzy inference system should be used instead of the single output Sugeno system (Mamdani & Assilian, 1975). Once such an inversion algorithm is developed and trained, it can be integrated as a processing unit to the inspection system to provide the characteristics of detected flaws in real-time.
- From the category of common probe's positioning and misalignment errors, probe's tilt and lift-off are investigated here since these two are majorly responsible for degrading the ECT signal quality during automated scans. Beside these two, angular deviations of the direction of D-shaped coils from the intended scan direction could also weaken the ECT signal. It is desirable to investigate the effect of such deviations on the signal of ECT and count them in development of the forward model. Doing so allows one to determine the sizing uncertainties more realistically. Other factors originated from the faults in probe's fabrication may also exist. Ideally, the effect of such parameters should be characterized and included in model as well (R. D. Mooers & Aldrin, 2016b). However using custom probes diminishes such problems.
- Based on the experience achieved in the reliability study of ECT, it is highly recommended to use spring-loaded probes in automated ECT of ferromagnetic parts since this would reduce the lift-off noise in the signal and consequently, the noise can

be solely assigned to the surface roughness. Surface condition for the samples used in POD demonstration shall represent the condition of those in actual inspections since the impact of this factor in ECT of ferromagnetic materials is significant. Furthermore, other calibration procedures such as two-point calibration could reduce the variability of signal response caused by the inspector's calibration. In this case, the POD representation majorly includes the effect of test parameters rather than human factor.

The POD curves plotted for automated and manual scans here only served as a comparison measure between the two testing techniques. It is clear that including more flawed/unflawed samples and controlled parameters to such a study adds to its reliability albeit the costs increases. Whenever concerns related to the cost of the POD study arise, MAPODs are the most beneficial alternatives. Developing such studies requires models representing actual defects, material and probe properties, in order to simulate the signal of actual cracks as accurate as possible. Besides, carrying out ECT signal sensitivity studies based on these models helps to indicate the influential parameters required for the study. The volume of simulations in such studies could also be reduced by assuming that the signal response variability at each defect size is a linear function of influential parameters (Rosell, 2015).

## **Future work**

### **Eddy current testing for detecting hydrogen embrittlement**

It has been known for a long time in industries that the exposure of steels to hydrogen during processes such as heat treatment welding, electroplating, and acid pickling could cause HE. HE endangers the performance of the in-service components by causing unexpected failure. Even the small amounts of hydrogen adsorbed by material can reduce ductility of the host and in turn, the time to failure of components. Among materials, the susceptibility of high strength steels to HE is highest even at room temperatures. Due to this fact and the high sensitivity applications of such materials, industries have been looking for a NDE method to

detect hydrogen and quantify the amount of it in components to be able to take necessary actions regarding them. For the same purpose the DPHM-601 project is defined by CRIAQ in order to explore the capability of different NDE techniques fitting this application. ECT is also nominated by the project, as one of the NDE methods, for assessment of HE in SAE 4340 martensitic stainless steel components of aircraft landing gear. According to the plan of the project, some test coupons of SAE 4340 are prepared, each undergoing a different process to achieve various intensities of hydrogen content. The three principle processes used in preparation of samples are cadmium electroplating, baking and chemical etching. The philosophy of using cadmium electroplating is, mainly, to charge the samples indirectly with hydrogen. In addition, baking is believed to be the main mean of reducing the hydrogen content. Furthermore, the plated cadmium layer is removed (*i.e.* sample is stripped) from some samples using a chemical solution to investigate if this layer traps hydrogen. A primary bar stock of SAE 4340 having 3 inches of outer diameter is cut to length of  $0.25 \pm 0.015$  inches. The bar stock is prepared by air-melting per aerospace material specification (AMS) 6415 standard and quenched and tempered according to AMS 2759/2 to obtain ultimate tensile strength of 260-280 ksi. Table 6.1 provides a list of the samples and summarizes the procedures used for their preparation.

Table 6.1 procedures used in preparation of samples to study hydrogen embrittlement

<b>Sample ID</b>	<b>Processing</b>
A	Neither baked nor plated
B	Plated and baked immediately
C	Plated, and baked after 8 hours delay
D	Plated, and baked after 16 hours delay
E	Plated, stripped and baked immediately
F	Plated, stripped and baked after 8 hours delay
G	Plated, stripped and baked after 16 hours delay
H	Plated, neither stripped nor baked
I	Plated, stripped but it is not baked

As presented in Table 6.1, the processes for samples are planned in a manner to generate different hydrogen concentrations in samples. Although this is planned based on a literature review and experience-based knowledge of industrial partners, the result might not be as anticipated. To this end, other academics involved in the project are trying to measure the actual hydrogen concentration of each sample using nuclear resonance analysis and thermal desorption spectroscopy. Besides, some mechanical tests including the constant loading of standard samples, designed according to American society for testing and material (ASTM) F-519, are carried out to evaluate the HE of plated components (International, 2017). These tests are still incomplete, and only a fraction of the results is in hand. It is important to compare the ECT measurements to the result of those tests in order to gain a better understanding of the behaviour observed in ECT signal variations from one sample to another.

For the purpose of ECT inspections, a surface reflection absolute probe performing at frequency range of 20 kHz to 200 kHz is used. It is expected that hydrogen content affects conductivity or/and permeability of the ferromagnetic steel sample. Moreover, besides affecting the base metal properties, the hydrogen may also influence electrical conductivity of the cadmium layer for the samples plated with cadmium. The ECT probe used here is believed to be a good choice fitting the intended application since an absolute configuration is appropriate for monitoring the variations of this kind. The probe is connected to a Nortec 500S ECT unit and subsequently, different test frequencies, selected within the interval of the probe's performing frequency, are used in tests. The gains on Nortec device are set equally and the rotation angle is set to zero during the tests. A point is marked on the surface of each of A, E and I samples. The probe is nulled inside air and it is approached to samples A, E, and I to touch them perpendicularly at the marked point. The lift-off traces are captured consecutively for the frequency range of 20 kHz-200 kHz with increments of 20 kHz. Figure 6.1(a) demonstrates the impedance plane including the lift-off traces collected from the three samples at different frequencies. As suggested by the figure, discrimination between the traces of these three samples is easier at the highest frequency of 200 kHz. Accordingly, this frequency is used for the tests hereafter. The primary result from inspecting random locations

on the surface of samples A, E, and I is shown in Figure 6.2(b). To provide a better visual to compare these traces, the impedance plane is rotated so the trace of sample A becomes horizontal and also the probe is nulled while it is placed on the surface of this sample. In this manner, all the measurements are referenced to the probe's impedance when it is on sample A. According to observations, the lift-off traces obtained for different samples are distinguishable from each other. Moreover, the trace of sample E falls closer to the one from sample A since sample E is baked immediately after plating and sample A did not have any treatment. However, Figure 6.1(c) shows that by placing the probe randomly on the surface of one sample, as an instance sample E here, large signal variability is obtained. Thus, it is not possible to say that the trace of sample A always falls below the one from sample I, as it can be seen in Figure 6.1(c). These impedance variabilities for the samples with the stripped plating layer are related to non-uniformities in the removal of the plating layer. It is believed that the etching process does not completely remove the plating and the thickness of the remaining cadmium layer varies at different surface spots. In addition, for sample A, it is witnessed that the impedance value varies slightly as different surface spots are tested. These observations for sample A could be due to the inhomogeneities in conductivity and permeability of the base material. Figure 6.1(c) shows that the traces collected from sample A and I overlap. Noteworthy that among the non-plated samples, these two are supposed to have the largest signal discrepancy considering their treatment. In general, the probe's impedance averaged for several test locations on the surface of each of these three samples shows that the impedance value decreases from sample I to A.

The same testing procedure can be carried out for the plated samples. Extremely larger signal variability due to the change of test spot on the sample's surface is observed for the plated samples. However, averaging the impedance values, which are randomly collected from different spots of a sample's surface, helps to discriminate the signal of these samples.

The first task was to ensure that ECT can provide enough resolution to discriminate different samples from each other. Now, it is time to plan a methodology to inversely infer the hydrogen content from the averaged impedance value of each sample. For this purpose, the

impedance value should be related to material properties that are directly affected by hydrogen content.

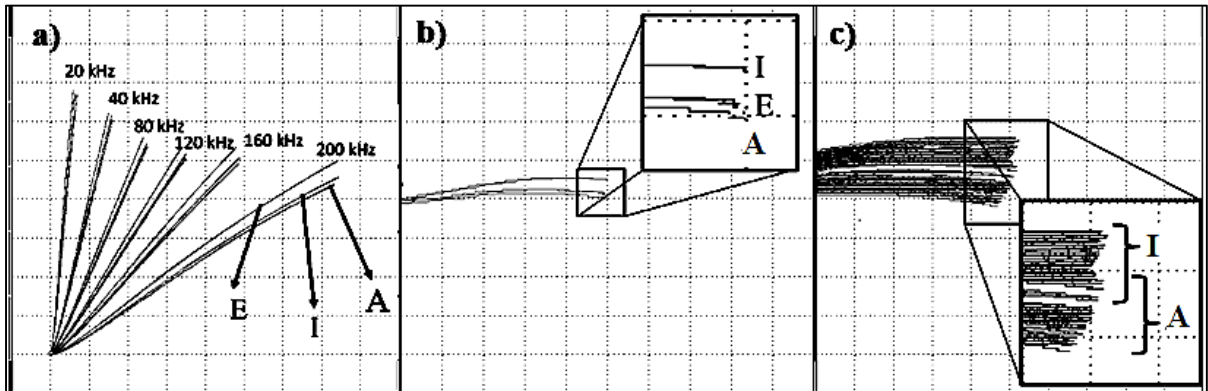


Figure 6.1 Screen of Nortec 500S showing (a) the effect of test frequency on lift-off traces for three samples of I, E and A, (b) rotated horizontally lift-off traces at 200 kHz for three samples I, E and A, (c) overlapping of the lift-off traces of samples I and A recorded collectively from different spots on their surface

As mentioned earlier hydrogen would most likely affect the conductivity and permeability of the substrate as well as the conductivity of the plating layer. Investigating the combined effect of material properties on the probe's impedance could be misleading since it is possible that the effect of two different properties be identical and as a result, it becomes difficult to find out the changes in the probe's impedance is attributed to which one. Therefore, the effect of each of these properties on the impedance should be studied individually by isolating one property and subsequently, relate it to the hydrogen content through experiments. As an example, saturating non-plated samples magnetically sets the relative permeability of the samples to one. In this manner, the effect of electromagnetic permeability is excluded and one would be able to relate the impedance changes to the variation of conductivity alone. The following is a proposed methodology providing the necessary steps to be able to present the recorded ECT impedance values as a function of hydrogen concentration.

1. Simplifying the problem: It is essential to reduce the number of material properties included in the primary study. As an example, the non-plated steel samples can be magnetically saturated by applying a sufficiently large electromagnetic field on the

samples during the test. Doing so makes it possible to monitor the variations of the probe's impedance, as we test different non-plated samples, as a function of the difference in their electrical conductivity.

2. Developing a model: The probe's impedance can be linked to the material's conductivity through developing a model which incorporates the interaction between the probe and the material. To this end, the probe and material should be well characterized so, the inputs of the model are as accurate as possible. Subsequently, the model's reliability should be verified. This can be done by comparing the model's impedance outputs, testing a standard sample with known properties, to the experimental measurements of the same sample.
3. Inferring the conductivity value from the measured impedance: Through this strategy, one could take the material's conductivity as an unknown variable in the model and perform a sweep on this parameter to match the output of the model to the measured impedance of different samples. Accordingly, the conductivity value for each sample can be deduced.
4. Conductivity versus hydrogen content: The same samples used in the study are also tested by other academic groups through destructive tests in order to determine their content of hydrogen. Therefore, it is possible to establish a relationship between the conductivity value and hydrogen content for each sample given these values.
5. Inferring the permeability value from the measured impedance: After determining the conductivity, the permeability can be evaluated through the model by removing the saturation field. The conductivity value can be kept constant, as determined in the previous steps, and the permeability value can be swept in the model to fit the model's output on the measured impedance value. Thus, the permeability can be also discovered and related to the hydrogen content.
6. Plated samples: The procedure to determine the conductivity of the plated layer follows the same fashion. Initially, the conductivity and permeability of the substrate shall be evaluated through the aforementioned steps. Afterwards, by keeping those as constant values in the model, the conductivity of the plated layer should be swept to find the agreement between the impedance readings and the model's output.

Currently, the project is still in its initial stages and the following describes the advancements that are made so far. The internal components of the probe used in these tests are characterized through 3-D model reconstruction of CT-scan images. Likewise, the number of turns and dimensions are extracted from these images as depicted in Figure 6.2. Moreover, the permeability of the cores are determined through model calibration.

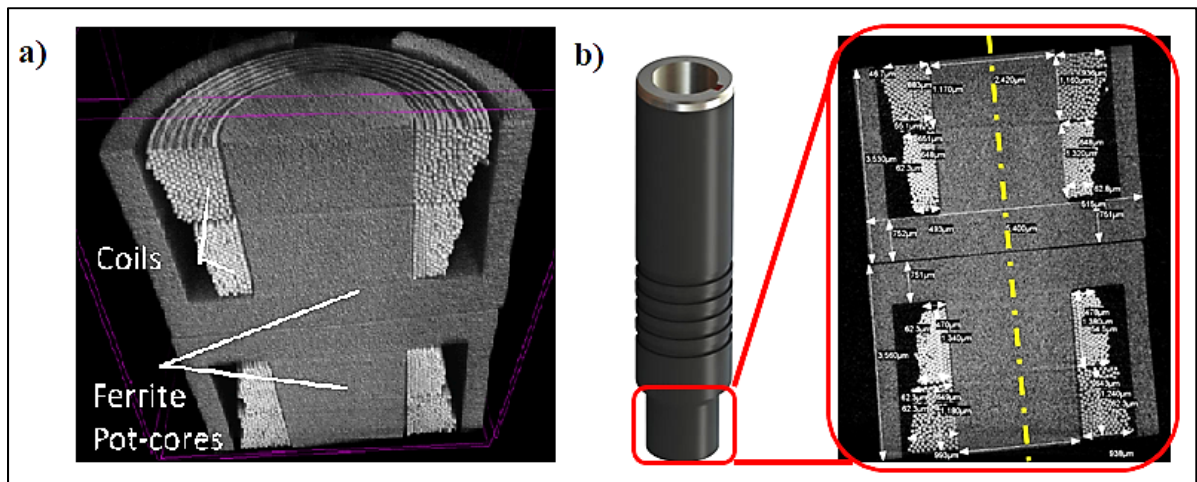


Figure 6.2 (a) 3-D model reconstructed from CT-scan image stack of the reflection absolute surface probe showing coils and cores, and (b) X-ray image of the probe along with its axis of symmetry

According to the geometry of the probe while testing an undefective sample, it is possible to prepare a 2-D axisymmetric CAD model for FEM analysis. The axis of symmetry is illustrated with a dashed line in Figure 6.2(b). 2-D model decreases the simulation time significantly and allows very rapid parametric sweep within the model. Noteworthy that, only the bottom core and coils are included in the model since the upper half of the probe is only meant to serve as a reference sensing the air. Accordingly, the model is prepared in Comsol, as shown in Figure 6.3(a) and the properties of the coils and the cores are assigned to the corresponding domains. The probe's model is subsequently calibrated by performing some tests on standard aluminum and copper samples with known conductivity values.

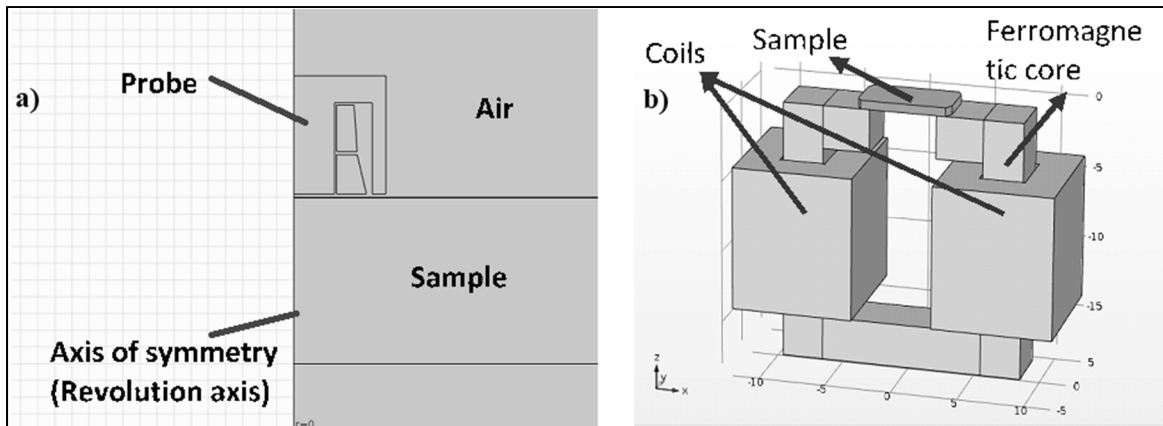


Figure 6.3 (a) Axisymmetric 2-D model for assembly of probe, sample and air domain prepared in Comsol and, (b) 3-D model of magnetizer's assembly and SAE 4340 sample

In order to saturate the samples magnetically, it is essential to have an electromagnetic yoke, which can apply high intensities of electromagnetic field to the sample. Toward that, a CAD model for an electromagnetic yoke comprised of two heavily wound coils and ferrite cores is designed based on the commercially available materials. The design is imported into Comsol for secondary analysis. The 3-D model assembly consists of the cores, coils and the steel sample A which is cut as a strip. The ferrite core material, called Kool  $M\mu 90$ , is selected from the data sheets available in market. In order to be able to take into account its nonlinear permeability in FEM simulations, its  $B-H$  curve is extracted and digitized. In the same fashion, the  $B-H$  curve of SAE 4340 steel, extracted from literature (Kwun & Burkhardt, 1987), is assigned to the steel sample. The coils' dimensions as well as their number of turns are varied in the model to achieve the saturation of the steel sample, which happens at approximately magnetic field density of 1.6 T within the sample. The coils are carrying a DC current of 20 A. Figure 6.4(a) shows the simulation results for the solution of  $B$  within the different components. From the figure, it is evident that the  $B$  field amplitude is larger than 1.6 T in the steel sample. In Figure 6.4(b), a high pass filter is applied for the field densities of higher than 1.6 T to provide a clearer image of the saturated region in the sample. It is discovered that having two coils, each with 200 turns of a round-sectioned magnet wire with American wire gauge (AWG) of 7 could result in saturation of the steel sample. Based on the

design, the coils are ordered to be wound and they were sent for subsequent assembly. A picture of the final assembly coils and cores is presented in Figure 6.4(c).

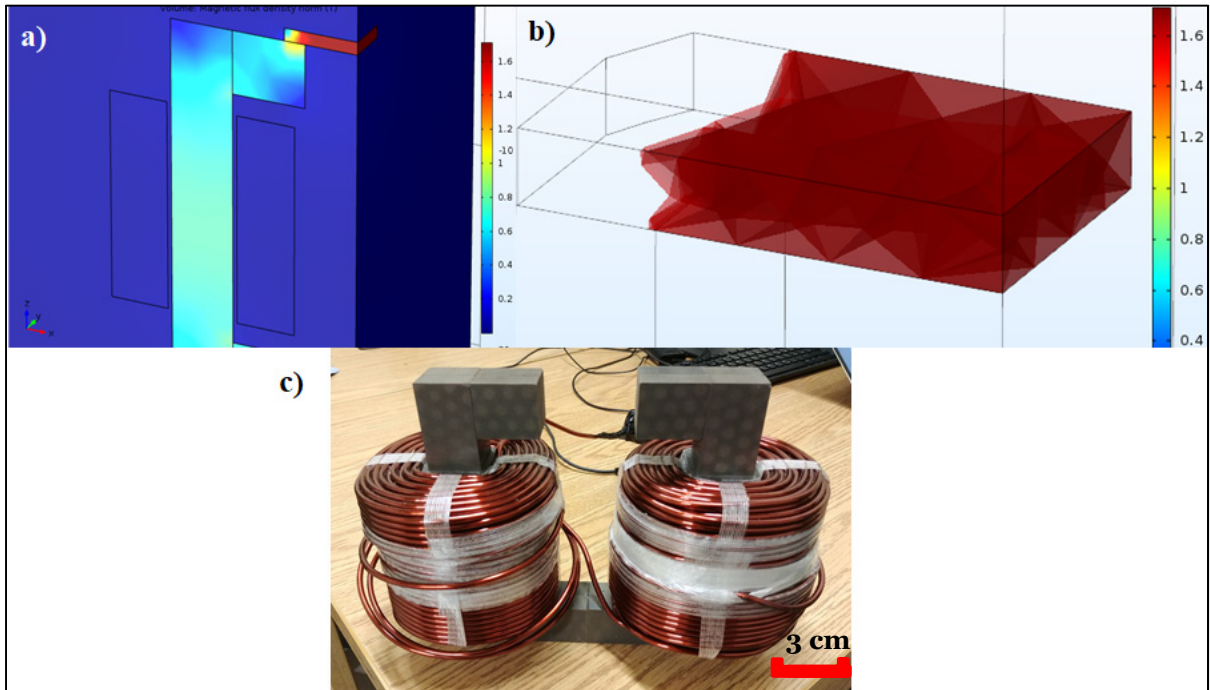


Figure 6.4 Magnetic field density (a) inside different domains of the assembly including the SAE 4340 sample, and (b) inside the SAE 4340 sample after applying 1.6 T high pass filter

This work is still incomplete and it will be continued by other students involved in the project DPHM-601. However, the following conclusions could be drawn from the early work that has been done so far:

- It is possible to discriminate the samples that are undergone different treatments, as presented in Table 6.1, using their ECT impedance values. In other words, ECT provides sufficient resolution for sorting these samples, each containing a different concentration of hydrogen.
- ECT reflection absolute surface probe are best suited for measuring the variations of material properties such as electrical conductivity and magnetic permeability. Since, it is expected that hydrogen content affect these two properties, these probe types are

the most appropriate choice for such applications providing the absolute impedance reading of the receiver coil.

- Using higher test frequencies seems to provide a better separation between the signals of different samples. The highest allowable frequency (*i.e.*, 200 kHz) of the probe is used in this study however; it might be possible to further improve the results by using a probe, which performs at higher frequencies.
- According to the design of magnetizer, two coils, each with 200 turns from a magnet wire of 7 AWG with round cross section should carry 20 A of DC current in order to saturate most parts of the SAE 4340 sample. The design parameters for the magnetizer are optimized to saturate a sample with size of 70 mm × 30 mm × 6 mm.
- A time domain heat transfer analysis of the coils shows that the temperature of the coils remains below 90° C after one hour of operation while a DC current of 20 A flows in the coils. Accordingly, the wire insulation, which is designed to work at maximum temperature of the 200° C, should stay intact for short testing durations.

## APPENDIX I

### **A MODEL-BASED STUDY OF THE EFFECT OF SEMI-ELLIPTICAL SURFACE NOTCH GEOMETRY ON THE SIGNAL OF A SPLIT-D EDDY CURRENT PROBE**

Ehsan Mohseni <sup>a</sup>, Martin Viens <sup>a</sup>, Demartonne Ramos França <sup>b</sup>

<sup>a</sup> École de technologie supérieure (ÉTS); Montréal, Québec, Canada

<sup>b</sup> John Abbott College; Sainte-Anne-de-Bellevue, Québec, Canada

NDT in Canada 2016 & 6th International CANDU In-Service Inspection Workshop  
November 15-17, 2016, Burlington, Ontario, Canada

#### **Abstract**

Eddy current testing (ECT) of tiny fatigue surface cracks are mostly carried out by means of differential probes. Among their various designs, Split-D reflection differential probes, named after their D-shaped internal cores and receiver coils, are particularly interesting because of their small footprint that makes them suitable for inspecting short surface cracks. In many of ECT theories and modelling trials that have been published on the interaction of fatigue cracks with the magnetic field of ECT probes, fatigue cracks are simplified and replaced by semi-elliptical notches. Therefore, in model-based ECT studies, electrical discharge machined (EDM) notches are frequently used since they are advantageous in terms of their low manufacturing cost as well as their usefulness in calibration and model verification procedures. Additionally, ECT signals obtained from EDM notches can roughly estimate those obtained from real fatigue cracks having the same size. Accordingly, in the present study a commercially available split-D surface probe is modeled based on its actual dimensions and material properties. The dimensions of the probe are extracted from a CT-scan reconstruction and inserted in the 3-D model. The probe scanning over 3 semi-elliptical notches having different sizes is simulated using the AC/DC module of COMSOL Multiphysics. A test frequency of 500 kHz is considered in the simulations, and the test block containing the notches is assigned with material properties of aluminum. The effect of simulation parameters, such as mesh size and distribution, is investigated, and hence the parameters are finely tuned to achieve consistent results. Afterwards, the reliability of the

simulation outputs is assessed by comparing them to impedance measurements of semi-elliptical surface notches in an aluminum block. This validation study shows acceptable matching of the probe's impedance obtained from both simulations and measurements. After validation of the model, the sensitivity of eddy current signals to variations of the notch geometry (e.g., notch opening, depth and length) is studied using the 3-D simulations. The importance of studying the notch opening originates from the fact that by decreasing this opening in the simulations, a better approximation of a fatigue crack shall be achieved. On the other hand, the ECT signals obtained from different notch lengths and depths establish a size dependent signal archive at the selected test frequency. This archive can be used as a basis for inversion purposes using artificial intelligence algorithms to be pursued in future studies.

## APPENDIX II

### **SENSITIVITY OF EDDY CURRENT SIGNALS TO PROBE'S TILT AND LIFT-OFF WHILE SCANNING SEMI-ELLIPTICAL SURFACE NOTCHES - A FINITE ELEMENT MODELING APPROACH**

Ehsan Mohseni <sup>a</sup>, Martin Viens <sup>a</sup>

<sup>a</sup> École de technologie supérieure (ÉTS), Montréal, Québec, Canada

NDT in Canada 2017  
June 6-8, Québec City, Québec, Canada

#### **Abstract**

In aircraft maintenance programs, Eddy current testing (ECT) has always been one of the most reliable methods of inspecting wheels, turbine blades, and rivet holes. Due to the loading conditions, fatigue induced crack is the most common flaw type in these components. Therefore, a high sensitivity ECT probe is required to reliably detect such shallow surface cracks. Split-D reflection differential probe with a very small footprint is proven to be the most efficacious tool for detecting very tight and tiny fatigue cracks. The advantages related to the differential configuration of D-shaped receiver coils are multifold. This configuration is less prone to the noise generated by lift-off variations; moreover, the effect of gradual variations of conductivity and permeability within the material is negligible on the probe's signal. Accordingly, the signal to noise ratio and the reliability of such a probe are significantly improved. Evaluation of large panels with curved complex surfaces as well as high inspection volumes of aging structures have increased the demands for automated robotized inspection systems. Even though robotic systems could conduct faster and more consistent ECT scans, they always suffer from errors in probe positioning. These errors commonly emerge as lift-off variations or deviation of the probe from perpendicularity (i.e. probe tilt angle). Origins of these misalignments can be mainly attributed to the friction forces between the probe and the part surface, deviations of the part geometry from the one used for generating the scan path, and initial calibration process of the coordinates corresponding to the tool and sample frames. In any case, the errors regarding the probe

positioning change the nature of recorded signals. Accordingly, it is necessary to investigate it further in order to know the extent of their influence on probe's impedance. Hence, this research studies the effect of small tilt angles and lift-off variations of a split-D reflection differential probe on the signals of three semi-elliptical surface notches each having different dimensions. For this end, numerical simulations are carried out using Comsol multiphysics while a validation study of this FEM approach is presented in an earlier publication. Five probe's tilt angles, up to a maximum of 5 degrees, are considered. Similarly, four probe's lift-offs, up to a maximum of 140  $\mu\text{m}$ , are simulated. In both cases, model's outcome (phase and amplitude of the notch signals) is validated through experimental measurements.

## BIBLIOGRAPHY

- Achenbach, J., & Thompson, D. (1991). Towards quantitative non-destructive evaluation of aging aircraft. *Structural Integrity of Aging Airplanes*, 1-13. doi: 10.1007/978-3-642-84364-8\_1
- Aldrin, J., Knopp, J., Lindgren, E., & Jata, K. (2009). Model-assisted probability of detection (MAPOD) evaluation for eddy current inspection of fastener sites. *Review of Progress In Quantitative Nondestructive Evaluation*, 28, 1784-1791. doi: 10.1063/1.3114175
- Aldrin, J. C., Sabbagh, H. A., Annis, C., Shell, E. B., Knopp, J., & Lindgren, E. A. (2015). Assessing inversion performance and uncertainty in eddy current crack characterization applications. In *41st Annual Review of Progress In Quantitative Nondestructive Evaluation: Volume 34* (Vol. 1650, pp. 1873-1883). AIP Publishing. doi: 10.1063/1.4914813
- Aldrin, J. C., Sabbagh, H. A., Murphy, R. K., Sabbagh, E. H., Knopp, J. S., Lindgren, E. A., & Cherry, M. R. (2012). Demonstration of model-assisted probability of detection evaluation methodology for eddy current nondestructive evaluation. In *Review of Progress in Quantitative Nondestructive Evaluation, Volume 31* (Vol. 31, pp. 1733-1740). AIP Publishing. doi: 10.1063/1.4716421
- Aldrin, J. C., Sabbagh, H. A., Sabbagh, E., Murphy, R. K., Keiser, M., Forsyth, D. S., & Lindgren, E. A. (2014). Model-based inverse methods for bolt-holt eddy current (BHEC) inspections. In *Review of Progress In Quantitative Nondestructive Evaluation* (Vol. 1581, pp. 1433-1440). AIP Publishing. doi: 10.1063/1.4864990
- Annis, C. (2009). *MIL-HDBK-1823A, Nondestructive Evaluation System Reliability Assessment*. Philadelphia, PA, USA.
- Annis, C. (2018). Statistical Best-Practices for Building Probability of Detection (POD) models, R package mh1823, version 5.4.4. Accessed on 1 March at <http://www.statisticalengineering.com/mh1823/>
- Auld, B., & Moulder, J. (1999). Review of advances in quantitative eddy current nondestructive evaluation. *Journal of Nondestructive Evaluation*, 18(1), 3-36. doi: 10.1023/A:1021898520626
- Auld, B., Muennemann, F., & Winslow, D. (1981). Eddy current probe response to open and closed surface flaws. *Journal of Nondestructive Evaluation*, 2(1), 1-21. doi: 10.1007/BF00614993

- Bagaviev, A., & Ulbrich, A. (2004). Life assessment of turbine components based on deterministic and probabilistic procedures. *International Journal of Pressure Vessels and Piping*, 81(10), 855-859. doi: 10.1016/j.ijpvp.2004.07.003
- Beissner, R. (1988). Approximate model of eddy-current probe impedance for surface-breaking flaws. *Journal of Nondestructive Evaluation*, 7(1), 25-34. doi: 10.1007/BF00565774
- Berens, A. P. (2000). *Probability of Detection (POD) Analysis for the Advanced Retirement for Cause (RFC)/Engine Structural Integrity Program (ENSIP) Nondestructive Evaluation (NDE) System-Volume 1: Pod Analysis*. U.S. Defense Technical Information Center.
- Bhaumik, S., Sujata, M., & Venkataswamy, M. (2008). Fatigue failure of aircraft components. *Engineering Failure Analysis*, 15(6), 675-694. doi: 10.1016/j.engfailanal.2007.10.001
- Blitz, J. (2012). *Electrical and Magnetic Methods of Non-destructive Testing* (Vol. 3). Netherlands: Springer. doi: 10.1007/978-94-011-5818-3
- Boller, C. (2001). Ways and options for aircraft structural health management. *Smart Materials and Structures*, 10(3), 432.
- Boukani, H. H., Viens, M., Tahan, S., & Gagnon, M. (2014). On the performance of nondestructive testing methods in the hydroelectric turbine industry. In *27th IAHR Symposium on Hydraulic Machinery and Systems* (Vol. 22, pp. 012018). IOP Publishing. doi: 10.1088/1755-1315/22/1/012018
- Bowler, J. R. (2000). Inversion of open cracks using eddy-current probe impedance measurements. In *Review of Progress in Quantitative Nondestructive Evaluation* (Vol. 509, pp. 529-534). AIP. doi: 10.1063/1.1306094
- Bowler, J. R., & Harfield, N. (1998). Evaluation of probe impedance due to thin-skin eddy-current interaction with surface cracks. *Magnetics, IEEE Transactions on*, 34(2), 515-523. doi: 10.1109/20.661483
- Bowler, J. R., Jenkins, S., Sabbagh, L., & Sabbagh, H. (1991). Eddy-current probe impedance due to a volumetric flaw. *Journal of Applied Physics*, 70(3), 1107-1114. doi: 10.1063/1.349615
- Bowler, J. R., Sabbagh, L., & Sabbagh, H. (1990). Eddy-current probe impedance due to a surface slot in a conductor. *IEEE Transactions on Magnetics*, 26(2), 889-892. doi: 10.1109/20.106460

- Bowler, J. R., Yoshida, Y., & Harfield, N. (1997). Vector-potential boundary-integral evaluation of eddy-current interaction with a crack. *IEEE Transactions on Magnetics*, 33(5), 4287-4294. doi: 10.1109/20.620437
- Bowler, J. R. (1994). Eddy-current interaction with an ideal crack. I. The forward problem. *Journal of Applied Physics*, 75(12), 8128-8137. doi: 10.1063/1.356511
- Bowler, J. R., & Norton, S. J. (1992). Eddy current inversion for layered conductors. *Journal of Research in Nondestructive Evaluation*, 4(4), 205-219. doi: 10.1007/BF01616488
- Bowler, J. R., Sabbagh, L. D., & Sabbagh, H. A. (1989). A theoretical and computational model of eddy-current probes incorporating volume integral and conjugate gradient methods. *IEEE Transactions on Magnetics*, 25(3), 2650-2664. doi: 10.1109/20.24505
- Bowler, J. R., Theodoulidis, T. P., Xie, H., & Ji, Y. (2012). Evaluation of eddy-current probe signals due to cracks in fastener holes. *IEEE Transactions on Magnetics*, 48(3), 1159-1170. doi: 10.1109/TMAG.2011.2170084
- Brown, A., & Eviston, C. (2017). Model development and validation of geometrically complex eddy current coils using finite element methods. In *Review of Progress in Quantitative Nondestructive Evaluation* (Vol. 1806, pp. 110015). AIP Publishing. doi: 10.1063/1.4974693
- Burke, S. (1985). A perturbation method for calculating coil impedance in eddy-current testing. *Journal of Physics D: Applied Physics*, 18(9), 1745.
- Burke, S. (1988). A benchmark problem for computation of  $\Delta Z$  in eddy-current nondestructive evaluation (NDE). *Journal of Nondestructive Evaluation*, 7(1), 35-41. doi: 10.1007/BF00565775
- Burke, S. (1994). Eddy-current inversion in the thin-skin limit: Determination of depth and opening for a long crack. *Journal of applied physics*, 76(5), 3072-3080. doi: 10.1063/1.358454
- Burke, S., & Ibrahim, M. (2004). Mutual impedance of air-cored coils above a conducting plate. *Journal of Physics D: Applied Physics*, 37(13), 1857. doi: 10.1088/0022-3727/37/13/021
- Burrows, M. L. (1964). *A theory of eddy-current flow detection* (Dissertation, University of Michigan, University of Michigan).
- Buvat, F., Pichenot, G., Prémel, D., Lesselier, D., Lambert, M., Voillaume, H., & Choffy, J. P. (2004). Eddy-current modeling of ferrite-cored probes. In *Review of Progress in Quantitative Nondestructive Evaluation, Volume 23* (Vol. 760, pp. 463-470). AIP Publishing. doi: 10.1063/1.1916712

- Carboni, M., & Cantini, S. (2015). Advanced ultrasonic “Probability of Detection” curves for designing in-service inspection intervals. *International Journal of Fatigue*, 86, 77-87. doi: 10.1016/j.ijfatigue.2015.07.018
- Cecco, V. S., Van Drunen, G., & Sharp, F. L. (1983). *Eddy current testing, volume 1*. Chalk River, ON, Canada: Atomic Energy of Canada Ltd., Chalk River, Ontario. Chalk River Nuclear Labs.
- Chari, M. (1974). Finite-element solution of the eddy-current problem in magnetic structures. *IEEE Transactions on Power Apparatus and Systems*, (1), 62-72. doi: 10.1109/TPAS.1974.293916
- COMSOL, I. (2007). AC/DC Module User’s Guide: COMSOL AB.
- COMSOL, I. (2012). Single-turn and Multi-turn Coil Domains in 3D.
- COMSOL, I. (2018). COMSOL Multiphysics Reference Manual, version 5.3. Accessed at [www.comsol.com](http://www.comsol.com)
- Davis, J. R. (1989). *ASM Handbook: Nondestructive evaluation and quality control* (Vol. 17). ASM International.
- Dillström, P., & Nilsson, F. L. (2007). 7.11-Probabilistic Fracture Mechanics. In *Comprehensive Structural Integrity* (Vol. 7, pp. 465-489). Elsevier. doi: 10.1016/B0-08-043749-4/07097-X
- Dodd, C., & Deeds, W. (1968). Analytical Solutions to Eddy-Current Probe-Coil Problems. *Journal of Applied Physics*, 39(6), 2829-2838. doi: 10.1063/1.1656680
- Dodd, C. V., Luquire, J., Deeds, W., & Spoeri, W. (1969). *Some eddy-current problems and their integral solutions*. Oak Ridge National Lab, Tennessee.
- Findlay, S., & Harrison, N. (2002). Why aircraft fail. *Material Today*, 5(11), 18-25. doi: 10.1016/S1369-7021(02)01138-0
- García-Martín, J., Gómez-Gil, J., & Vázquez-Sánchez, E. (2011). Non-destructive techniques based on eddy current testing. *Sensors*, 11(3), 2525-2565. doi: 10.3390/s110302525
- Georgiou, G. A. (2007). PoD curves, their derivation, applications and limitations. *Insight - Non-Destructive Testing and Condition Monitoring*, 49(7), 409-414. doi: 10.1784/insi.2007.49.7.409

- Ghiocel, D. M., & Wang, L. (2004, 26-28 July). *Risk-Based Condition Assessment and Maintenance Engineering for Aging Aircraft Structure Components* presented at 9th ASCE Specialty Conference on Probabilistic Mechanics and Structural Reliability, Albuquerque, NM, USA.
- Grimberg, R., Savin, A., Iancu, L., & Chifan, S. (2000). Fuzzy inference system used for a quantitative evaluation of the material discontinuities detected by eddy current sensors. *Sensors and Actuators A: Physical*, 81(1), 248-250. doi: 10.1016/S0924-4247(99)00134-X
- Grover, H. J. (1966). *Fatigue of aircraft structures*. Columbus, OH, USA: Battelle Memorial Institute.
- Hagemaiyer, D., & Kark, G. (1997). Eddy current detection of short cracks under installed fasteners. *Materials Evaluation*, 55(1), 25-30.
- Hellier, C. (2013). *Handbook of Nondestructive Evaluation, Second Edition*. New York, NY, USA: McGraw-Hill Education.
- Hochschild, R. (1959). Electromagnetic methods of testing metals. *Progress in Non Destructive Testing*, 1, 57-109.
- Ida, N., Betzold, K., & Lord, W. (1982). Finite element modeling of absolute eddy current probe signals. *Journal of Nondestructive Evaluation*, 3(3), 147-154. doi: 10.1007/BF00566556
- Ida, N., Palanisamy, R., & Lord, W. (1983). Eddy current probe design using finite element analysis. *Materials Evaluation*, 41(12), 1389-1394.
- International, A. (2017). ASTM F519-17a Standard Test Method for Mechanical Hydrogen Embrittlement Evaluation of Plating/Coating Processes and Service Environments. West Conshohocken, PA, USA: ASTM International.
- Iyyer, N., Sarkar, S., Merrill, R., & Phan, N. (2007). Aircraft life management using crack initiation and crack growth models—P-3C Aircraft experience. *International Journal of Fatigue*, 29(9), 1584-1607. doi: 10.1016/j.ijfatigue.2007.03.017
- Jang, J. S. R., Sun, C. T., & Mizutani, E. (1997). *Neuro-fuzzy and Soft Computing: A Computational Approach to Learning and Machine Intelligence*. Prentice Hall.
- Jones, R., Molent, L., & Pitt, S. (1999). Study of multi-site damage of fuselage lap joints. *Theoretical and Applied Fracture Mechanics*, 32(2), 81-100. doi: 10.1016/S0167-8442(99)00029-4

- Khan, T., & Nakagawa, N. (1999). Quantitative impedance measurements for eddy current model validation. In *Review of Progress in Quantitative Nondestructive Evaluation, Volume 19* (Vol. 509, pp. 441-448). AIP Publishing. doi: 10.1063/1.1306082
- Knopp, J. S., Aldrin, J., Lindgren, E., & Annis, C. (2006). Investigation of a Model-Assisted Approach to Probability of Detection Evaluation. In *33rd Annual Review of Progress in Quantitative Nondestructive* (Vol. 894, pp. 1775-1782). AIP Publishing. doi: 10.1063/1.2718178
- Knopp, J. S., Aldrin, J. C., & Misra, P. (2006). Considerations in the validation and application of models for eddy current inspection of cracks around fastener holes. *Journal of Nondestructive Evaluation*, 25(3), 123-137. doi: 10.1007/s10921-006-0008-3
- Kojima, F., Kubota, N., & Hashimoto, S. (2001). Identification of crack profiles using genetic programming and fuzzy inference. *Journal of Materials Processing Technology*, 108(2), 263-267. doi: 10.1016/S0924-0136(00)00767-6
- Krause, H., Hohmann, R., Gruneklee, M., & Maus, M. (2000). Aircraft wheel and fuselage testing with eddy current and SQUID. *7th European Conference on Non-destructive Testing*, 42(3), 148-151.
- Kwun, H., & Burkhardt, G. L. (1987). Effects of grain size, hardness, and stress on the magnetic hysteresis loops of ferromagnetic steels. *Journal of Applied Physics*, 61(4), 1576-1579. doi: 10.1063/1.338093
- Lemire, H., Underhill, P., & Krause, T. (2009, June). *Applying POD to improve bolt hole eddy current inspection* présentée à 4th European-American Workshop on Reliability of NDE, Berlin, Germany.
- Lemire, H., Underhill, P., Krause, T., Bunn, M., & Butcher, D. (2010). Improving probability of detection of bolt hole eddy current inspection. *Research in Nondestructive Evaluation*, 21(3), 141-156. doi: 10.1080/09349841003728951
- Libby, H. L. (1971). *Introduction to Electromagnetic Nondestructive Test Methods* John Wiley & Sons.
- Lu, Y., Bowler, J. R., & Theodoulidis, T. P. (2012). An analytical model of a ferrite-cored inductor used as an eddy current probe. *Journal of Applied Physics*, 111(10), 103907. doi: 10.1063/1.4716189
- Mackerle, J. (1999). Finite-element modelling of non-destructive material evaluation: a bibliography (1976-1997). *Modelling and Simulation in Materials Science and Engineering*, 7(1), 107.

- Mackerle, J. (2004). Finite-element modelling of non-destructive material evaluation, an addendum: a bibliography (1997–2003). *Modelling and Simulation in Materials Science and Engineering*, 12(5), 799. doi: 10.1088/0965-0393/12/5/004
- Mamdani, E. H., & Assilian, S. (1975). An experiment in linguistic synthesis with a fuzzy logic controller. *International Journal of Man-Machine Studies*, 7(1), 1-13. doi: 10.1016/S0020-7373(75)80002-2
- May, P., Zhou, E., & Morton, D. (2007). Numerical modelling and implementation of ferrite cored eddy current probes. *NDT & E International*, 40(8), 566-576. doi: 10.1016/j.ndteint.2007.06.003
- Mix, P. E. (2005). *Introduction to Nondestructive Testing: A Training Guide*. Wiley-Interscience. doi: 10.1002/0471719145
- Mohseni, E., Viens, M., & Franca, D. R. (2016). A model-based study of the effect of semi-elliptical surface notch geometry on the signal of a Split-D eddy current probe. In *NDT in Canada 2016 & 6th International CANDU In-Service Inspection Workshop*. Canadian Institute for Non-Destructive Evaluation.
- Mooers, R. D., Knopp, J. S., & Blodgett, M. (2012). Model based studies of the split D differential eddy current probe. In *Review of Progress in Quantitative Nondestructive Evaluation* (Vol. 1430, pp. 373-380). AIP Publishing. doi: 10.1063/1.4716252
- Mooers, R. D., & Aldrin, J. C. (2016a). Continued developments in the modeling of complex dimensions and orientation variation in split D differential eddy current probes. In *43rd Annual Review of Progress in Quantitative Nondestructive Evaluation, Volume 36* (Vol. 1806, pp. 110012). AIP Publishing. doi: 10.1063/1.4974690
- Mooers, R. D., & Aldrin, J. C. (2016b). Effects of angular variation on split D differential eddy current probe response. In *42nd Annual Review of Progress in Quantitative Nondestructive Evaluation* (Vol. 1706, pp. 090022). AIP Publishing. doi: 10.1063/1.4940559
- Mooers, R. D., Aldrin, J. C., & Knopp, J. S. (2015a). Model the effects of core/coil size and defect length on eddy current response. In *41st Annual Review of Progress In Quantitative Nondestructive Evaluation: Volume 34* (Vol. 1650, pp. 395-404). AIP Publishing. doi: 10.1063/1.4914635
- Mooers, R. D., Aldrin, J. C., & Knopp, J. S. (2015b). Realistic split D differential probe model validation. In *Review of Progress in Quantitative Nondestructive Evaluation* (Vol. 1650, pp. 385-394). AIP Publishing. doi: 10.1063/1.4914634

- Mooers, R. D., Knopp, J. S., Aldrin, J. C., & Sathish, S. (2013). Simulated parametric study based on a representative split D differential eddy current probe. In *40th Annual Review of Progress in Quantitative Nondestructive Evaluation: Incorporating the 10th International Conference on Barkhausen Noise and Micromagnetic Testing* (Vol. 1581, pp. 1344-1351). AIP Publishing. doi: 10.1063/1.4864977
- Mooers, R. D., Knopp, J. S., Aldrin, J. C., & Sathish, S. (2014). Split D differential probe model validation using an impedance analyzer. In *Review of Progress in Quantitative Nondestructive Evaluation* (Vol. 1581, pp. 1511-1518). AIP Publishing. doi: 10.1063/1.4865002
- Morabito, F. C. (1998). An intelligent network for defect profile reconstruction in eddy current applications. *Studies in Applied Electromagnetics and Mechanics*, 13, 434-437.
- Moulder, J. C., Uzal, E., & Rose, J. H. (1992). Thickness and conductivity of metallic layers from eddy current measurements. *Review of Scientific Instruments*, 63(6), 3455-3465. doi: 10.1063/1.1143749
- Nakagawa, N., Khan, T., & Gray, J. (2000). Eddy current probe characterization for model input and validation. In D. O. Thompson & D. E. Chimenti (Éds.), *Review of Progress in Quantitative Nondestructive Evaluation, Volume 21A* (Vol. 509, pp. 473-480). AIP Publishing. doi: 10.1063/1.1306086
- Nakagawa, N., Yang, M., Larson, B. F., Madison, E., & Raulerson, D. (2009). Study of the effects of EDM notch width on eddy current signal response. In *Review of Progress in Quantitative Nondestructive Evaluation* (Vol. 1096, pp. 287-294). AIP Publishing. doi: 10.1063/1.3114217
- Nath, S., Balasubramaniam, K., Krishnamurthy, C., & Narayana, B. (2010). Reliability assessment of manual ultrasonic time of flight diffraction (TOFD) inspection for complex geometry components. *NDT & E International*, 43(2), 152-162. doi: 10.1016/j.ndteint.2009.10.007
- Neuschaefer, R. W., & Beal, J. B. (1972). *Assessment of and standardization for quantitative nondestructive test* (n° 19730005756). USA: NASA.
- Norton, S. J., Kahn, A. H., & Mester, M. L. (1989). Reconstructing electrical conductivity profiles from variable-frequency eddy current measurements. *Journal of Research in Nondestructive Evaluation*, 1(3), 167-179.
- Olin, B. D., & Meeker, W. Q. (1996). Applications of statistical methods to nondestructive evaluation. *Technometrics*, 38(2), 95-112.

- Palanisamy, R., & Lord, W. (1979). Finite element modeling of electromagnetic NDT phenomena. *IEEE Transactions on Magnetics*, 15(6), 1479-1481. doi: 10.1109/TMAG.1979.1060412
- Peiró, J., & Sherwin, S. (2005). Finite difference, finite element and finite volume methods for partial differential equations. In *Handbook of Materials Modeling* (pp. 2415-2446). Springer. doi: 10.1007/978-1-4020-3286-8\_127
- Pitt, S., & Jones, R. (1997). Multiple-site and widespread fatigue damage in aging aircraft. *Engineering Failure Analysis*, 4(4), 237-257. doi: 10.1016/S1350-6307(97)00020-4
- Rajesh, S. (1997). Probability of detection models for eddy current NDE methods. *NDT & E International*, 3(30), 174.
- Rao, B., Raj, B., Jayakumar, T., & Kalyanasundaram, P. (2002). An artificial neural network for eddy current testing of austenitic stainless steel welds. *NDT & E International*, 35(6), 393-398. doi: 10.1016/S0963-8695(02)00007-5
- Rosado, L. S., Janeiro, F. M., Ramos, P. M., & Piedade, M. (2013). Defect characterization with eddy current testing using nonlinear-regression feature extraction and artificial neural networks. *IEEE Transactions on Instrumentation and Measurement*, 62(5), 1207-1214. doi: 10.1109/TIM.2012.2236729
- Rosell, A. (2015). Efficient finite element modelling of eddy current probability of detection with transmitter-receiver sensors. *NDT & E International*, 75, 48-56. doi: 10.1016/j.ndteint.2015.07.001
- Rosell, A., & Persson, G. (2011). Modelling of a differential sensor in eddy current non-destructive evaluation. In *COMSOL Users Conference*.
- Rosell, A., & Persson, G. (2012a). Comparison of experimental and model based pod in a simplified eddy current procedure. In *18th World Conference on Nondestructive Testing*. South African Institute for Non-Destructive Testing (SAINT).
- Rosell, A., & Persson, G. (2012b). Eddy current signal Response predictions for use in model assisted POD estimations based on different flaw characteristics. In *4th International Symposium on NDT in Aerospace*.
- Rosell, A., & Persson, G. (2012c). Finite element modelling of closed cracks in eddy current testing. *International Journal of fatigue*, 41, 30-38. doi: 10.1016/j.ijfatigue.2011.12.003
- Rosell, A., & Persson, G. (2013). Model based capability assessment of an automated eddy current inspection procedure on flat surfaces. *Research in Nondestructive Evaluation*, 24(3), 154-176. doi: 10.1080/09349847.2013.779401

- Rummel, W. D., & Matzkanin, G. A. (1997). *Nondestructive evaluation (NDE) capabilities data book*. Austin, TX, USA: Nondestructive Testing Information Analysis Center.
- Sabbagh, H. (1987). A model of eddy-current probes with ferrite cores. *IEEE Transactions on Magnetics*, 23(3), 1888-1904. doi: 10.1109/TMAG.1987.1065171
- Sabbagh, H. A., Murphy, R. K., Sabbagh, E. H., Aldrin, J. C., & Knopp, J. S. (2013). *Computational Electromagnetics and Model-Based Inversion*. New York, NY, USA: Springer-Verlag doi: 10.1007/978-1-4419-8429-6
- Sabbagh, H. A., Sabbagh, E. H., & Murphy, R. K. (2002). Recent advances in modeling eddy-current probes. In *Review of Progress in Quantitative Nondestructive Evaluation* (Vol. 615, pp. 423-429). AIP Publishing. doi: 10.1063/1.1472829
- Santandréa, L., & Le Bihan, Y. (2010). Using COMSOL-Multiphysics in an eddy current non-destructive testing context. In *COMSOL European Conference*.
- Schijve, J. (1994). Fatigue of aircraft materials and structures. *International Journal of Fatigue*, 16(1), 21-32. doi: 10.1016/0142-1123(94)90442-1
- Shell, E. B., Aldrin, J. C., Sabbagh, H. A., Sabbagh, E., Murphy, R. K., Mazdiyasn, S., & Lindgren, E. A. (2014). Demonstration of model-based inversion of electromagnetic signals for crack characterization. In *Review of Progress in Quantitative Nondestructive Evaluation, Volume 34* (Vol. 1650, pp. 484-493). AIP Publishing. doi: 10.1063/1.4914645
- Shull, P. J. (2016). *Nondestructive evaluation: theory, techniques, and applications*. CRC press.
- Sikora, R., & Baniukiewicz, P. (2005). Reconstruction of cracks from eddy current signals using genetic algorithm and fuzzy logic. In *Review of Progress in Quantitative Nondestructive Evaluation* (Vol. 820, pp. 775-782). AIP Publishing. doi: 10.1063/1.2184605
- Smid, R., Docekal, A., & Kreidl, M. (2005). Automated classification of eddy current signatures during manual inspection. *NDT & E International*, 38(6), 462-470. doi: 10.1016/j.ndteint.2004.12.004
- Society, I. C. (2018). Testing Electromagnetic Analysis Methods. International Compumag Society. Accessed at [www.compumag.org/jsite/team.html](http://www.compumag.org/jsite/team.html)
- Song, S. J., & Shin, Y. K. (2000). Eddy current flaw characterization in tubes by neural networks and finite element modeling. *NDT & E International*, 33(4), 233-243. doi: 10.1016/S0963-8695(99)00046-8

- Stratton, J. A. (2007). *Electromagnetic theory*. Wiley-IEEE Press.
- Sugeno, M. (1985a). *Industrial applications of fuzzy control*. New York, NY, USA: Elsevier Science Inc.
- Sugeno, M. (1985b). An introductory survey of fuzzy control. *Information Sciences*, 36(1-2), 59-83. doi: 10.1016/0020-0255(85)90026-X
- Takagi, T., & Sugeno, M. (1985). Fuzzy identification of systems and its applications to modeling and control. *IEEE Transactions on Systems, Man, and Cybernetics*, (1), 116-132. doi: 10.1016/B978-1-4832-1450-4.50045-6
- Takagi, T., Uesaka, M., & Miya, K. (1997). Electromagnetic NDE research activities in JSAEM. *Electromagnetic Nondestructive Evaluation*, 12, 9-16.
- Tarantola, A. (2005). *Inverse Problem Theory and Methods for Model Parameter Estimation*. Philadelphia, PA, USA: Society for Industrial and Applied Mathematics (SIAM).
- Theodoulidis, T. (2010). Developments in efficiently modelling eddy current testing of narrow cracks. *NDT & E International*, 43(7), 591-598. doi: 10.1016/j.ndteint.2010.06.003
- Tsoukalas, L. H., & Uhrig, R. E. (1996). *Fuzzy and neural approaches in engineering*. New York, NY, USA: John Wiley & Sons.
- Udpa, L., & Udpa, S. (1991). Neural networks for the classification of nondestructive evaluation signals. In (Vol. 138, pp. 41-45). IET. doi: 10.1049/ip-f-2.1991.0007
- Underhill, P., & Krause, T. W. (2011a). Eddy current analysis of mid-bore and corner cracks in bolt holes. *NDT & E International*, 44(6), 513-518. doi: 10.1016/j.ndteint.2011.05.007
- Underhill, P., & Krause, T. W. (2011b). Quantitative fractography for improved probability of detection (POD) analysis of bolt hole eddy current. *Research in Nondestructive Evaluation*, 22(2), 92-104. doi: 10.1080/09349847.2011.553349
- Underhill, P., & Krause, T. W. (2017). Finite element model study of the effect of corner rounding on detectability of corner cracks using bolt hole eddy current. In *AIP Conference Proceedings* (Vol. 1806, pp. 110006). AIP Publishing.
- Underhill, P. R., & Krause, T. W. (2011). Enhancing probability of detection and analysis of bolt hole eddy current. *Journal of Nondestructive Evaluation*, 30(4), 237-245. doi: 10.1007/s10921-011-0112-x

- Underhill, P. R., & Krause, T. W. (2016). Eddy current probability of detection for mid-bore and corner cracks in bolt holes of service material. *Research in Nondestructive Evaluation*, 27(1), 34-47. doi: 10.1080/09349847.2015.1045642
- Upadhyaya, B., Yan, W., Behraves, M., & Henry, G. (1999). Development of a diagnostic expert system for eddy current data analysis using applied artificial intelligence methods. *Nuclear Engineering and Design*, 193(1), 1-11. doi: 10.1016/S0029-5493(99)00162-4
- Verite, J. (1990). A coil over a crack. (results for benchmark problem 8 of team workshop). *COMPEL-The International Journal for Computation and Mathematics in Electrical and Electronic Engineering*, 9(3), 155-167. doi: 10.1108/eb010072
- Volker, A., Dijkstra, F., Terpstra, S., Heerings, H., & Lont, M. (2004). Modeling of NDE reliability: Development of a POD generator. In *16th World Conference on Nondestructive Testing*. Canadian Institute for Non-Destructive Evaluation.
- Wincheski, B., & Namkung, M. (1998). Detection of sublayer fatigue cracks under airframe rivets. In D. O. Thompson & D. E. Chimenti (Eds.), *Review of Progress in Quantitative Nondestructive Evaluation, Volume 17* (pp. 331-338). New York, NY, USA: Springer. doi: 10.1007/978-1-4615-5339-7\_42
- Xu, B. (2014). *Intelligent Eddy Current Crack Detection System Design Based on Neuro-Fuzzy Logic* (Concordia University, Montreal, QC, Canada). (978748).
- Xu, B., Xie, W., Viens, M., Mohseni, E., Birglen, L., & Mantegh, I. (2013). Intelligent eddy current crack detection system design based on neuro-fuzzy logic. In *The NDT in Canada 2013 Conference in conjunction with the International Workshop on Smart Materials & Structures, SHM and NDT for the Energy Industry* (pp. 7-10).
- Yusa, N., Perrin, S., Mizuno, K., & Miya, K. (2007). Numerical modeling of general cracks from the viewpoint of eddy current simulations. *NDT & E International*, 40(8), 577-583. doi: 10.1016/j.ndteint.2007.04.002
- Zeng, Z., Udpa, L., & Udpa, S. S. (2010). Finite-element model for simulation of ferrite-core eddy-current probe. *IEEE Transactions on Magnetics*, 46(3), 905-909. doi: 10.1109/TMAG.2009.2034651